UNIVERSITY OF CALIFORNIA
Los Angeles

Warped Time Stretch: Photonic Hardware Accelerators for Imaging and Sensing

A dissertation submitted in partial satisfaction
of the requirements for the degree
Doctor of Philosophy in Electrical Engineering

by

Jacky Chak-kee Chan

2018

ABSTRACT OF THE DISSERTATION

Warped Time Stretch: Photonic Hardware Accelerators for Imaging and Sensing

by

Jacky Chak-kee Chan
Doctor of Philosophy in Electrical Engineering
University of California, Los Angeles, 2018
Professor Bahram Jalali, Chair

Photonic time stretch is a well-established real-time optical technology. Using dispersion, the spectral modulation of a broadband optical pulse is stretched to alleviate the bandwidth bottleneck present in the subsequent analog-to-digital conversion and digital processing. The recent warped time stretch generalizes this concept with tailored non-uniform dispersion profiles, reshaping the wideband optical information arbitrarily and in real-time. Warped stretch can be considered a particular implementation of photonic hardware acceleration, a new category of data processing engines in which analog optical pre-processing is performed preceding optical-to-electrical conversion. Given a-priori knowledge of the non-uniform entropy statistics of the optical input spectrum, the dispersion profile can be engineered to provide the optimal warp for optical signal pre-processing, while maintaining the advantages of traditional time-stretch in terms of ultrafast, real-time data acquisition of wideband optical data. By optically reshaping the optical signal prior to uniform sampling, his introduces the effective capability of adaptive sampling rates to single-shot, ultrafast optical measurements and instrumentation, Such a capability has wide-ranging applicability, including optical pulse reshaping, feature extraction, network coding, data compression and optical phase retrieval.

To validate the generalization of time stretch to arbitrary warped mappings of the optical spectrum into the time domain, the theory of time stretching is re-explored, and additional physical constraints for the group delay profile and optical signal are identified. We also establish a mathematical equivalence of the temporal chirp of any large dispersion with the group delay, enabling the design of time-domain signals with passive dispersive elements that are described in the spectral domain.

Grounded by theoretical validation, we develop multiple applications to warped time stretch. We demonstrate that proper design of warped stretch transformation leads to time-bandwidth product engineering. We develop mathematical expressions for a dispersion-influenced time bandiwdth product and simulate the effect of warped dispersion on the time-bandwidth product for broadband optical signals. Using time-frequency analysis, we analyze the effect of imperfect dispersion profiles on the performance of such systems, and extend that analysis to dispersive phase recovery systems in the presence of system noise.

Similar to time-bandwidth engineering, we also show that the signal-to-noise ratio of the optical signal can be engineered if given a-priori knowledge of the spectrotemporal statistics of the signal. Via analysis and simulation of the signal-to-noise ratio under the influence of dispersion, we provide a design pathway for translating this a-priori knowledge into context-optimized data acquisition and processing. We also leverage these bandwidth engineering concepts in the digital domain, and develop an smart sampling approach for image compression.

In order to introduce warped dispersion in which the profile can be modified in real-time, we demonstrate a physical implementation of reconfigurable dispersion. In a generalization of chromo-modal dispersion, we use acousto-optics to provide a reconfigurable mapping of the spectrum to time. This is achieved by exploiting the angle-dependent excitation of multimode waveguides. Such a source for dispersion would be of interest for any time-stretch detection system where feedback is required for the dispersion profile.

The dissertation of Jacky Chak-kee Chan is approved.

David Saltzberg

Jia-Ming Liu

Tatsuo Itoh

Bahram Jalali, Committee Chair

University of California, Los Angeles
2018

To Jesus, my Lord and Saviour

and

To my parents,

Chun-Man and Dana

Table of Contents

List of Figures

ACKNOWLEDGMENTS

First and foremost, I would like to give my wholehearted thanks to my advisor, Prof. Bahram Jalali, for his guidance, vision, discussions and support. It has been a privilege to work under him, and I am grateful to be given the opportunity to be brought up to speed as I transitioned from a material science focus to electrical engineering at UCLA. In addition to the challenging work environment he has firmly established in the laboratory, I am indebted to him not only in learning the technical rigour in both theory and experiment, but also to clear presentational ideas and the importance of always considering the bigger picture, being mindful of direction and taking actionable steps towards what often appears to be unattainable goals.

I would like to thank all my journal and conference co-authors, for their input which directly shaped almost all the chapters in this dissertation. Chapter 3 is a version of an ArXiv preprint arXiv:1612.04562, 2016. Chapter 4 is a version of Applied Physics Letters Vol. 105, No. 22, p. 221105, 2014. Chapter 5 is a version of Optica Vol. 1, No.1, pp. 23-31, 2014. Chapter 6 is a version of the post-deadline paper at the Conference on Lasers and Electro-Optics (CLEO) Pacific Rim, PDP.4, Hong Kong, China, 2018. Chapter 7 is a version of Proceedings of SPIE, Photonics West: Real-time Measurements, Rogue Phenomena, and Single-Shot Applications III (Conf. 10517), San Francisco, CA, 2018. Finally, Chapter 8 is a version of PLoS ONE, Vol. 11, No. 7, 2016. I am particularly thankful for Prof. Mohammad Hossein Asghari for his mentorship and discussions, without which many of the results of these papers could not have been possible. I would also like to thank my other PhD committee members, Prof. Tatsuo Itoh, Prof. Jia-Ming Liu, and Prof. David Saltzberg, for their invaluable time, as well as the insightful exchanges during both my PhD prospectus and thesis defense regarding these results.

Apart from the mentorship of Prof. Asghari, I am thankful for Eric Diebold and Brandon Buckley for their mentorship when I first joined the laboratory, training me in my first optical experiments and their help with my first academic paper, and for Sebastian “Nino” Karpf, who was instrumental in helping me develop a better experimental common sense and for his valuable input and guidance for my projects during his time at the Jalali lab. I would also like to thank Yunshan Cathy Jiang and Cejo Konuparamban Lonappan for the fruitful discussions we had in the laboratory, technical or otherwise. Finally, Peter DeVore and Ata Mahjoubfar were instrumental in introducing me to the field of optics and photonics at that fateful OSA / SPIE Student Chapter meeting. In particular, I would like to highlight my gratitude to Ata; I am thankful for his friendship and his essential role in shaping my academic and professional thinking. Without his influence, the technical content of my papers would not be of as high a calibre.

In term of spiritual support, I am indebted to my church, the Chinese Baptist Church of West Los Angeles, as well as the GSM and ICF Christian fellowships. for their advice, love and support as fellow Christians. I also thank Gregory Lui and Michael Tu for their support and Christian perspectives on academia. Last but certainly not least, I thank Crystina Zhang immensely for being there for me as my time as a graduate student came to a close, for her love, encouragement, support and resourcefulness, always pushing me to succeed and pointing me towards what is most important. Thank you, Crystina! You are a constant reminder of God’s love to me.

I am thankful for the love and support of my family. My father, an academic himself, has always been a source of encouragement and wisdom since I started college. He has always been someone I look up to in terms of work ethic, leadership and reliability, a role model and mentor to which I am grateful. I thank my mother who is always extends a gentle listening ear and for her gentle and timely advice. I also thank my sister Jenny, for her care and support in the midst of her busyness, as she finishes a degree of her own. I am indebted to their support and sacrifice for the achievement of my PhD degree.

Finally, I thank God for all that I have, for leading me every step of the way of PhD career and beyond. My encounter with Peter and Ata was a prayer answered and I know He will continue to direct my path in the future. Thank You for Your unconditional and sacrificial love. I am eternally grateful for Your presence and provision throughout my life.

Vita

2009	Junior Research Assistant, Aaron Ho group, Chinese University of Hong Kong, Hong Kong
2010	Biosensor Researcher, Patricia Nieva group (SIMSLab), University of Waterloo, Canada
2011	Research Assistant, Hong Ma group (Multi-scale Design Laboratory), University of British Columbia, Canada
2012	B.Sc., Nanotechnology Engineering, University of Waterloo, Canada
2015	M.Sc., Electrical Engineering, University of California, Los Angeles, USA
2016	Teaching Assistant (Circuits Laboratory I), University of California, Los Angeles, USA
2017	Teaching Assistant (Physics for Electrical Engineers, Honors), University of California, Los Angeles, USA
2016–present	Graduate Student Researcher, Bahram Jalali group (Photonics Lab), Electrical Engineering Department, UCLA

Publications and Presentations

J. C.K. Chan, E. D. Diebold, B. W. Buckley, S. Mao, N. Akbari, B. Jalali, *"Digitally synthesized beat frequency-multiplexed fluorescence lifetime spectroscopy"*, Biomedical Optics Express, Vol. 5, No. 12, pp. 4428-4436, 2014.

B. Jalali, **J. C.K. Chan**, M. H. Asghari, *"Time–bandwidth engineering"*, Optica, Vol1, No. 1, pp. 23-31, 2014.

J. C.K. Chan, A. Mahjoubfar, M. H. Asghari, B. Jalali, *"Reconstruction in Time-Bandwidth Compression Systems"*, Applied Physics Letters, Vol. 105, No. 22, p. 221105, 2014.

J. C.K. Chan, M. H. Asghari, B. Jalali, *"Performance of time-bandwidth engineering systems"*, IEEE Photonics Conference, San Diego, CA, pp. 134-135, 2014.

J. C.K. Chan, A. Mahjoubfar, C. L. Chen, B. Jalali, *"Context-aware image compression"*, PLoS ONE, Vol. 11, No. 7, 2016.

B. Jalali, **J. C.K. Chan**, A. Mahjoubfar, D. R. Solli, M. Asghari, *"The Temporal Gearbox"*, arXiv preprint, arXiv:1612.04562v2, 2016.

J. C.K. Chan, S. Karpf, B. Jalali, *"Dynamic chromo-angular-modal excitation of multimode waveguides via acousto-optic deflection"*, SPIE Photonics West, Real-time Measurements, Rogue Phenomena, and Single-Shot Applications III (Conf. 10517), San Francisco, CA, 2018.

J. C.K. Chan, B. Jalali, *"Optical SNR Engineering with Warped Stretch"*, Conference on Lasers and Electro-Optics (CLEO) Pacific Rim, Post-deadline paper, PDP.4, Hong Kong, China, 2018.

J. C.K. Chan, B. Jalali, *"Unified Theory of Time Stretch Systems"*, In preparation. 2018.

CHAPTER 1

Introduction

The detection of optical ultrafast signals is a ubquitious problem across many disciplines, such as astronomy, biology, medical, military and industrial. In many such scenarios, the speed of such optical data is much higher than the acquisition electronics. Moreover, even if the speed limitations could be relaxed, the continuous and high-speed data acquisition would quickly accumulatie and lead to difficulties in data storage. Photonic time-stretch is a mature optical technique which was introduced in the 1990s to address the problem of speed, bridging the bandwidth gap between optics and electronics by slowing down the optical signal in real-time.

In this dissertation, we introduce warped time stretch, also known as foveated time stretch, to address the storage volume in a general manner via “foveated sampling”. The term “foveated sampling” comes from the “fovea centralis”, a small area near the centre of the retina, corresponding to cells that capture light for the central field of vision, in which nearly 50% of densely packed cone photoreceptor cells are located. The eye achieves image acquisition with non-uniform resolution in the visual field by spatially varying the cone cell density. Additionally, the spatially-varying photoreceptor cell density enables enhanced image resolution in central vision with lower resolution in the peripheral vision where high resolution is not necessary.

Our goal is to implement the same function for sampling of the spectrum of ultrafast waveforms, and to do so in real-time. Normally this would require a sampler with a sample rate that adapts to the instantaneous behaviour of the input signal in real-time. However, this is not possible because the time scales of optical signals are in the picosecond range or less, which is much shorter than the response time found in electronic circuits. In addition, the sampling rate would have to be synchronized with the variations in input signal.

A better approach that avoids the speed and synchronization issues is to perform warped time-stretching followed by uniform sampling. The first step is a spectrotemporal operation in which the spectrum of the broadband optical signal is non-uniformly mapped to a time scale that is slow enough to digitized. This is followed by uniform sampling in time domain performed by an analog-to-digital converter. When combined, this effectively achieves foveated spectral sampling at ultra-high speeds and in real-time. As we demonstrate below, this technique leads to efficient allocation of samples based on the information density of the spectrum.

Similar to linear time stretch, foveated stretch is realized using dispersive elements, but here the dispersion is tailored to map the spectrum into time in a signal-dependent manner [1, 2]. This represents a new type of sparse sampling that operates in real-time (in contrast to conventional sparse sampling that requires multiple measurements followed by iterative algorithms for signal reconstruction). The design of the dispersion profile is tailored to the time-averaged spectral statistics. It is open loop and does not require instantaneous adaptivity. Real-time optical data compression has been demonstrated with this technique to solve the big data predicament caused by the high throughput of time stretch instruments [3]. This has motivated similar follow-on works by a growing number of researchers [4–8].

In Chapter 2, we first develop a unified framework for the analysis of any optical system which utilizes time stretch. The theoretical study in this study identifies the major components of a warped time-stretch system and the general conditions necessary for a successful mapping of the optical spectrum into time with an frequency-dependent dispersion profile. This allows us to unify and standardize all disparate time-stretch related systems into the same framework for system analysis.

More generally, warped time stretch can be considered as a specific class of photonic hardware accelerators. Photonic hardware accelerators (PHAs) comprise a new category of data processing engines, in which analog optical pre-processing is performed preceding optical-to-electrical conversion and digital processing to alleviate the burden on the electronics. This vision enables the acquisition and digital processing of waveforms that are much faster than what is possible with conventional electronics. Chapter 3 shows that the application of large dispersion allows for as equivalence in describing dispersive effects in both time and frequency domains. We liken this particular application of spectral basis decomposition of the group delay to the operation of a mechanical gearbox, in which different gears can be selected to match the torque needed for a given velocity profile of a vehicle.

In many cases, the spectral profile is sufficient for the characterization of the input optical pulse, particularly in applications in which a “blank” optical pulse functions as the carrier or medium, such that the desired ultrafast signal imprinted onto the spectral intensity for real-time slow down using time stretch. In situations in which the original temporal profile of optical signal is of interest, the recovery of the time-domain waveform from the measured envelope spectrum of a time-stretched optical pulse requires phase recovery. Chapter 4 discusses the signal reconstruction process involving complex field recovery and back-propagation in the presence of noise. We show that the presecnce of noise and distortion to the acquired signal intensities significantly affects the convergence of the phase retrieval system, up to a noise cut-off threshold.

In Chapter 5 we explore the effect of introducing a warped dispersion on the time-bandwidth product of a broadband optical signal. We demonstrate that unlike conventional photonic time stretching, the time-bandwidth product can either be minimized or expanded, when the group delay profile is designed specifically to the local density of spectral features. Using time-frequency analysis, we also develop a mathematical expression for the product, and analyze its change under different dispersion profiles via simulations. We also analyze the impact that imperfections of the dispersion profiles have on the performance of such systems.

Given control on the power spreading and bandwidth reduction along the time-stretched waveform via dispersion, it is natural to also consider using tailored stretching to manipulate the signal-to-noise ratio (SNR) of an optical signal. Chapter 6 shows, by both theory on the instantaneous power and by simulations, that the SNR can be engineered as long as the information density of the spectrum is known on average, such that the dispersion profile can be appropriately designed. This opens up a new pathway to analog optical computing.

In order to design warped dispersion in real-time for time-stretch systems where feedback is required, a physical implementation of reconfigurable dispersion is often desirable. Chapter 7 provides one such implementation. It is a generalization of chromo-modal dispersion, which uses acousto-optics to provide a reconfigurable mapping of the spectrum to time. This is achieved by exploiting the angle-dependent excitation of multimode waveguides.

Finally, in Chapter 8, we taking the inspiration of the "foveated" methods we developed for non-uniform frequency-to-time mappings in optical signals for optical data compression, we demonstrate the application of warped stretch to digital image compression. We achieve image compression via smart downsampling by pre-warping an image prior to uniform downsampling and demonstrate the compression technique on both black-and-white as well as colour images.

CHAPTER 2

Mathematical foundations of warped time stretch

2.1 Introduction

Data acquisition devices are in the core of all communication, sensing and imaging systems. Otherwise known as analogy-to-digital converters (DAC) or "digitizers" they are often limit how fast and how accurately data can be captured in a system. While the performance of data converters may be limited by one or a combination of different mechanisms, the accuracy decreases with speed for all data converters. Put differently, the effective number of bits reduces at high input signal bandwidths and high sampling rates [9]. To alleviate this problem, photonic time-stretch was introduced in the 1990s as a key-enabling technology for single-shot, real-time detection of ultrafast optical signals [10,11]. Over the years, many variants of time-stretch systems have been developed and implemented under various modalities, including real-time oscilloscopes such as TiSER [12, 13], optical coherence tomography (OCT) [14,15], line-scan imaging [16–18], and more recently, to photon Doppler velocimetry (PDV) [19–22] and broadband laser ranging (BLR) [21–24].

By enabling single-shot measurements and non-stop capture of billions of frames, time-stretch has led to several scientific breakthroughs, ranging from the first observation of the laser mode-locking dynamics [25] and soliton explosions in fibers [26], to relativistic electron bunching in synchrotrons [27], and to single-shot

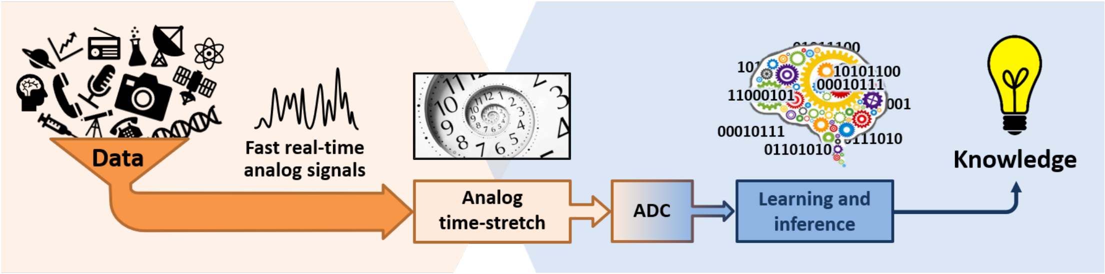

Figure 2.1: Overview of the role of time-stretch in data acquisition and processing systems. Time-stretching acts as the bridge between real-world analog data and knowledge derived from digital processing, learning and inference algorithms, by slowing down the acquisition speed of the incoming data to match that of the processing electronics.

stimulated Raman spectroscopy (SRS) [28, 29], and label-free detection of cancer cells in blood with record accuracy, a feat achieved by combining time stretch with deep learning networks [17, 30].

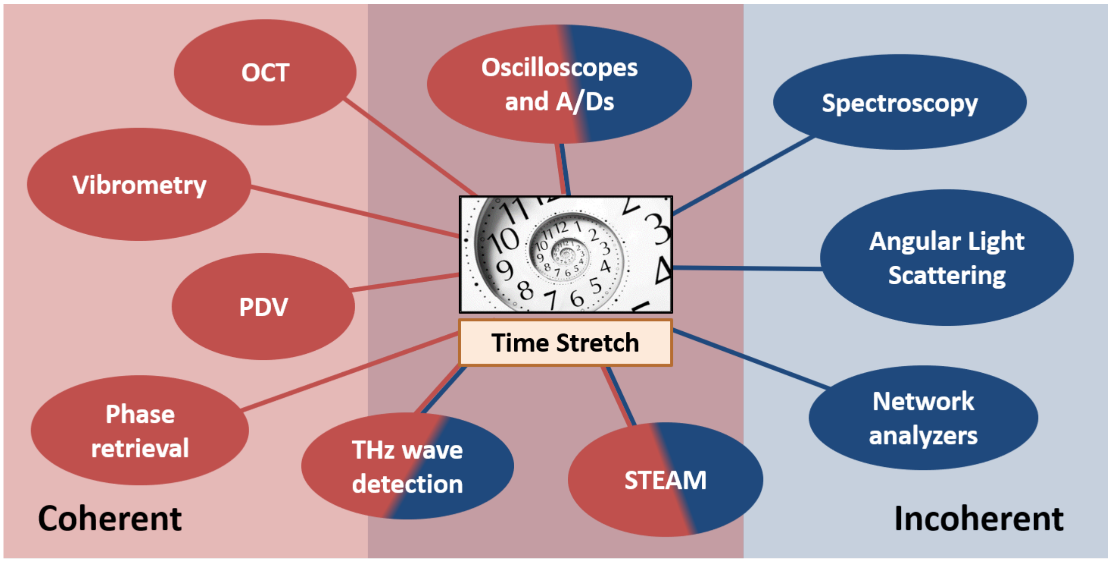

Figure 2.2: Applications and detection modalities of photonic time-stretch, including both coherent (e.g. optical coherence tomography (OCT), phase retrieval etc.) and incoherent methods (time-stretch spectroscopy, angular light scattering etc.); some techniques admit both incoherent and coherent detection modalities.

With the rapidly proliferating creation and deployment of time stretch systems in various applications, having a unified framework for understanding, design and analysis of time stretch systems is paramount. In this context, various time stretch systems ranging from oscilloscopes to microscopes are described in a single theoretical framework following and single canonical equation. This unified framework also leads to a modular design of time stretch systems using a limited set of fundamental building blocks.

Figures 2.2 and 2.3 illustrate the key steps common amongst all time-stretch systems. We start with Figure 2.2 which illustrates four key steps common amongst all time-stretch systems. The first step is modulation of the fast sig-

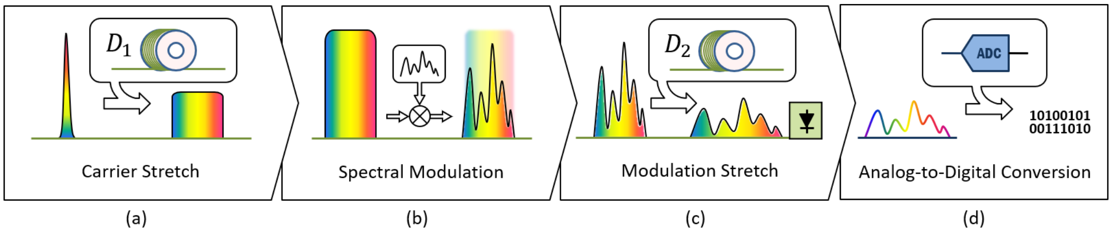

Figure 2.3: Overview of the time-stretch process. (a) The wideband optical carrier is chromatically dispersed via time-stretch dispersive Fourier transform (TS-DFT). (b) Information is encoded onto the optical spectrum amplitude. Since the carrier is previously dispersed, the temporal amplitude modulation now has a one-to-one correspondence to the carrier wavelengths. (c) With frequency-to-time mapping of the information in place, further chromatic dispersion with TS-DFT now slows down the modulated signal in real time. (d) This real-time information can now be analyzed in the digital domain. By tuning the ratio of group velocity dispersion between the two dispersive elements D_1 and D_2, the speed of the input signal can now match that of the analog-to-digital converter (ADC) or digitizer. In general, the time-stretch technique can be seen as a Fourier-domain ADC, which digitizes the modulated optical spectrum (as opposed to the time-domain optical input).

nal onto the spectrum of a broadband optical pulse. Various ways to do this for temporal, spatial and angular signals under test are described later. The second step is to stretch the signal modulation on a wideband optical carrier by way of chromatic dispersion, in a process that is now known as the time-stretch dispersive Fourier transform (TS-DFT). A key component of any photonic time-stretch system is the dispersive element, which disperses the wideband optical spectrum in time. With sufficiently large chirp, the dispersion profile completely specifies the location of each wavelength in the carrier spectrum, which results in a one-to-one correspondence between the carrier intensity in time and each wavelength component. Therefore, if information is now encoded onto the optical spectrum via amplitude modulation, any further chromatic dispersion of the carrier can stretch the encoded signal in time. Furthermore, by tuning the stretch factor, which is the ratio of group velocity dispersion between the first and second dispersive elements D_1 and D_2, the speed of the input signal can now match that of the analog-to-digital converter (ADC), thus opening up the bottleneck of optical data acquisition and sensing. Moreover, distributed Raman amplification can be integrated into the second dispersive element to maintain high SNR. In general, the time-stretch technique can be seen as a Fourier-domain ADC, which digitizes the modulated optical spectrum (as opposed to the time-domain optical input).

The spectral modulation process can be direct in time or in the Fourier domain. To imprint the target information onto the optical carrier, the carrier must be first be stretched in the domain which the information is located. This can be achieved both incoherently and coherently. In the incoherent case, we identified three main mappings: time-to-time, time-to-space, and time-to-angle; these correspond to Time-Stretch Enhanced Recorder (TiSER) [12], time-stretch imaging systems such as the Serially Time Encoded Amplified Microscopy (STEAM) [16], and angular encoded time-stretch systems such as the Spectrally Encoded Angular Light Scattering (SEALS) [31]. To access information encoded in the spectral

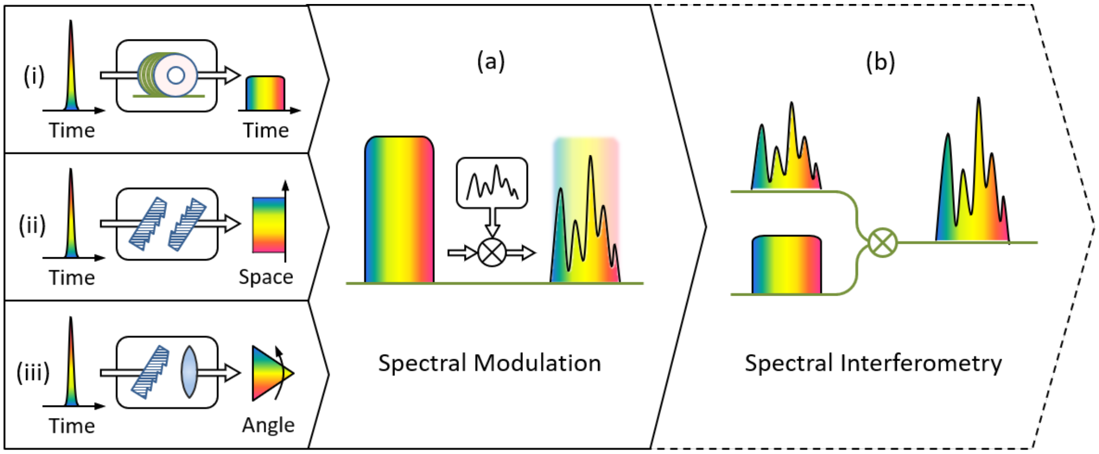

Figure 2.4: Two ways to modulate the information onto the optical spectrum. (a) Incoherent (direct) modulation and (b) coherent (indirect/Fourier domain) modulation. (a) The wideband optical carrier is chromatically dispersed via time-stretch dispersive Fourier transform (TS-DFT), or spatially dispersed with a grating pair, or provide angular encoding by including a lens after the grating pair. (b) To access information encoded in the spectral phase of the input optical signal (or, similar to the incoherent case, in the spatial variations of the optical path length), the Fourier domain optical intensity is indirectly modulated with axial (refractive index) modulation. In the incoherent case, we identified three main mappings: (i) time-to-time, (ii) time-to-space, and (iii) time-to-angle; these correspond to Time-Stretch Enhanced Recorder (TiSER), time-stretch imaging systems such as the Serially Time Encoded Amplified Microscopy (STEAM), and angular encoded time-stretch systems such as the Spectrally Encoded Angular Light Scattering (SEALS).

phase of the input optical signal (or, similar to the incoherent case, in the spatial variations of the optical path length), the Fourier domain optical intensity is indirectly modulated with axial (refractive index) modulation.

The outline of the paper is as follows: Section 2.2 will be the mathematical framework of the time-stretch technique. Section 2.3 will be an extended and unified discussion of time-stretch systems by application, in terms of incoherent and coherent output data, respectively. For the incoherent case, this includes time-stretch spectroscopes, oscilloscope / digitizers (with TiSER), network analyzers, hardware processing acceleration, imaging (with STEAM) and angular light scattering (with SEALS); for the coherent case, this includes optical coherence tomography (OCT), vibrometry, photon Dopple velocimetry (PDV), interferometry, and phase retrieval. We aim to demonstrate that all time-stretch systems share the same time-and signal-dependent stretch factor M, where:

$$M[t(\lambda)] = 1 + \frac{D_2(\lambda)}{D_1(\lambda)} \tag{2.1}$$

2.2 Mathematical derivations for warped time stretch

We introduce a mathematical framework for describing the coherent evolution of the signal envelope of an optical pulse, following the terminology and framework outlined in [32], but expanding upon it in terms of introducing a general group delay dispersion profile; this is known as warped stretch (also known as foveated stretch or anamorphic stretch). The general procedure involves the input optical signal being stretched by an initial dispersive element D_1, followed by a modulation of the information onto the envelope of the broadband optical carrier. This signal envelope is then stretched in time by a second dispersive element D_2.

2.2.1 Carrier stretching

The complex envelope spectrum of a broadband input pulse $E_i(t) = |E_i(t)|e^{j\omega_c t}$ can be described in the phasor notation as:

$$\tilde{E}_i(\omega - \omega_c) = \mathcal{F}_t\{E_i(t)\} = |\tilde{E}_i(\omega - \omega_c)|e^{j\theta(\omega-\omega_c)} \tag{2.2}$$

where ω_c is the carrier frequency. Dispersive elements are typically phase-only operations with their transfer function in the form $H(\omega) = e^{j\phi(\omega-\omega_c)}$, where $\phi(\omega)$ is the phase induced by dispersion. In terms of the propagation constant $\beta(\omega)$, $\phi(\omega)$ can be written as:

$$\phi(\omega) = \beta(\omega) \cdot z = \sum_{m=1}^{\infty} \frac{\beta_m z}{m!}(\omega - \omega_c)^m \tag{2.3}$$

where β_m is the m-th order propagation constant coefficient in the z-direction.

The group delay $\tau = d\phi/d\omega$ can similarly be Taylor-expanded into its dispersive modes. Without loss of generality, we will also shift our frame of reference to that of the delayed optical pulse. That is, for a propagation length of $z = L$ within the dispersive element, $t - \beta_1 L \to t$ is the dispersion-retarded temporal frame of reference, and:

$$\tau(\omega) - \beta_1 L \to \tau(\omega) = \sum_{m=2}^{\infty} \frac{\beta_m z}{(m-1)!}(\omega - \omega_c)^m \tag{2.4}$$

is the $\beta_1 L$-retarded group delay. We will hereon use the alternative formulation of expressing dispersive elements in terms of the more tangible physical quantity of group delay $\tau(\omega)$, instead of in terms of the spectral phase $\phi(\omega)$. After passing through the first dispersive element D_1, the time-domain output electric field envelope $E_{D1}(t)$ can then be written in the most general form as:

$$E_{D1}(t) = \mathcal{F}_\omega^{-1}\{\tilde{E}_{D1}(\omega - \omega_c)\} = \int_{-\infty}^{\infty} |\tilde{E}_i(\omega - \omega_c)|e^{j\theta(\omega-\omega_c)+j\int \tau_{D1} d\omega - j\omega t} \frac{d\omega}{2\pi} \tag{2.5}$$

Note that in most cases, the input pulse is near transform-limited or has limited chirp prior to stretching, and thus $\theta' \ll \tau_{D1}$ and we can ignore the input chirp

$\theta'(\omega)$. This justifies the formulation of frequency-to-time mapping purely in terms of the group delay profile $\tau(\omega)$.

2.2.2 Signal modulation

At this point, the optical carrier is modulated with the desired information $s(t)$, which has a complex spectrum $\tilde{s}(\Omega)$. We can represent the modulation in the spectral domain as a convolution:

$$\tilde{E}_I(\Omega_I) = \mathcal{F}_t\left\{E_{D1}(t) \cdot s(t)\right\} = \int_{-\infty}^{\infty} \tilde{E}_{D1}(\Omega_I - \Omega)\tilde{s}(\Omega)\frac{d\Omega}{2\pi} \tag{2.6}$$

where $\Omega = \omega - \omega_c$ is the (angular) modulation frequency relative to the carrier frequency ω_c.

The simple expression that models the modulation event demonstrates the power of time stretch systems to be applicable to a vast range of information modalities. This includes analog signals, such as RF microwave signals, Raman signatures, as well as digital signals; moreover, both amplitude and phase information can also be accommodated.

2.2.3 Modulation stretching

The modulated carrier is now passed through another dispersive element D_2 with a corresponding $\beta_1 L_{D2}$-retarded group delay $\tau_{D2}(\omega)$. Mathematically, this is represented as:

$$\begin{aligned}\tilde{E}_{D2}(\omega_I) &= \tilde{E}_I(\omega_I)e^{j\int \tau_{D2}d\omega} \\ &= \int_{-\infty}^{\infty} \tilde{E}_i(\Omega_I - \Omega)e^{j\left[\int \tau_{D1}(\omega_I-\Omega)d(\omega_I-\Omega)+\int \tau_{D2}(\omega_I)d\omega_I\right]}\tilde{s}(\Omega)\frac{d\Omega}{2\pi}\end{aligned} \tag{2.7}$$

The two group delay integrals can be combined to become:

$$\begin{aligned}&\int \tau_{D1}(\omega_I - \Omega)d(\omega_I - \Omega) + \int \tau_{D2}(\omega_I)d\omega_I \\ &\qquad = \hat{\tau}'_{tot}(\omega_I;\Omega)\left(\omega_I - \frac{\Omega}{M(\omega_I;\Omega)}\right)^2 + \frac{\hat{\tau}'_{D2}(\omega_I)}{M(\omega_I;\Omega)}\Omega^2\end{aligned} \tag{2.8}$$

where $\hat{\tau}(\omega) = \sum_{m=2}^{\infty} \frac{\beta_m L}{m!}(\omega - \omega_c)^{m-2}$ is a weighted Taylor expansion of the group delay dispersion $\hat{\tau}^{'}(\omega) = \sum_{m=2}^{\infty} \frac{\beta_m L}{(m-2)!}(\omega - \omega_c)^{m-2}$, and $\hat{\tau}^{'}_{tot}(\omega_I; \Omega) = \hat{\tau}^{'}_{D1}(\omega_I - \Omega) + \hat{\tau}^{'}_{D2}(\omega_I)$ is the total weighted group delay dispersion, and $M(\omega_I; \Omega) = 1 + \frac{\hat{\tau}^{'}_{D2}(\omega_I)}{\hat{\tau}^{'}_{D1}(\omega_I - \Omega)}$ is the generalized stretch factor. For time-stretch dispersive Fourier transformation to occur, the group delay dispersion $D_\lambda(\omega) = \frac{2\pi c}{\lambda_0^2}\frac{\partial \tau(\omega - \omega_c)}{\partial \omega}$ must be sufficiently large over the optical bandwidth to spread the spectral components of the optical pulse apart and achieve information stretch via wavelength-to-time mapping. Mathematically speaking, this corresponds to a sufficiently large group delay dispersion which satisfies the asymptotic requirements of the stationary phase approximation.

If we assume slow-varying group delay dispersion profiles $\tau^{'}_{D1}(\omega)$ and $\tau^{'}_{D2}(\omega)$, we can invoke the stationary phase approximation [28, 33, 34] to give us the following new stationary envelope frequency $\omega_s = \hat{\tau}^{-1}_{tot}(t)$ by:

$$\frac{d}{d\omega_I}\left[\int \hat{\tau}_{tot}(\omega_I; \Omega) d\omega_I - \omega_I t\right]_{\omega_I = \omega_s} = 0 \tag{2.9}$$

From the aforementioned assumptions made for the stationary phase approximation to be valid, we are justified to also assume $\tilde{s}(\Omega)$ has compact support over $\left[-\frac{\Delta\Omega}{2}, \frac{\Delta\Omega}{2}\right]$, where the modulation bandwidth $\Delta\Omega$ is much smaller than that of the optical bandwidth $\Delta\omega$. This allows us to remove the convolutional dependence on certain slow-varying terms. When assuming that $\tilde{s}(\omega)$ has compact support over $\left[-\frac{\Delta\Omega_I}{2}, \frac{\Delta\Omega_I}{2}\right]$ we can make the following slow-varying envelope approximations:

$$\begin{aligned}
M(\omega_I; \Omega) &\approx M(\omega_s) = 1 + \frac{\hat{\tau}^{'}_{D2}(\omega_s)}{\hat{\tau}^{'}_{D1}(\omega_s)} \approx 1 + \frac{D_2(\lambda)}{D_1(\lambda)} \\
\hat{\tau}^{'}_{D1}(\omega_s - \Omega) &\approx \hat{\tau}^{'}_{D1}\left(\omega_s - \frac{\Omega}{M}\right) \\
\hat{\tau}^{'}_{D2}(\omega_s) &\approx \hat{\tau}^{'}_{D2}\left(\omega_s - \frac{\Omega}{M}\right) \\
\tilde{E}_i(\Omega_s - \Omega) &\approx \tilde{E}_i\left(\Omega_s - \frac{\Omega}{M}\right)
\end{aligned}$$

It should be noted that the temporal resolution of the envelope is limited by the oscillation period of the optical carrier, but which can be tuned by adjusting the magnitude of the dispersion prior to the spectral modulation [35]. After the approximations are made, the output electric field $E_{D2}(t)$ can therefore be shown to be:

$$E_{D2}(t) \approx \mathcal{E}_{D2}(t) \cdot s_{TS}\left(\frac{t}{M(\omega_s)}\right) \tag{2.10}$$

where:

$$\mathcal{E}_{D2}(t) \equiv \frac{\tilde{E}_i(\omega_s - \omega_c)}{\sqrt{2\pi|\tau'_{tot}(\omega_s)|}} \exp\left[j\int \tau(\omega_s)d\omega_s - j\omega_s t - j\frac{\pi}{4}\right] \tag{2.11}$$

is the stretched envelope of the unmodulated transformed-limited pulse $E_i(t)$, and

$$\begin{aligned} s_{TS}\left(\frac{t}{M(\omega_s)}\right) &\equiv \int_{-\infty}^{\infty} \tilde{s}(\Omega) \exp\left(j\frac{\hat{\tau}_{D2}(\omega_s)}{M(\omega_s)}\Omega^2 - j\frac{\Omega}{M(\omega_s)}t\right)\frac{d\Omega}{2\pi} \\ &= \mathcal{F}_{\Omega}^{-1}\left\{\tilde{s}(\Omega)\exp j\phi_{DIP}(\Omega)\right\} \end{aligned}$$

is the time-stretched modulation, with $\phi_{DIP}(\Omega) = \frac{\hat{\tau}(\omega_s)}{M(\omega_s)}\Omega^2$ as the spectral dispersion-induced phase. As expected, each frequency $\omega_s = \hat{\tau}'_{tot}(t)$ of the optical spectrum amplitude is now mapped to a distinct point in time t. From this mapping, we can see that the total duration of the optical carrier envelope has been stretched by a factor of $\langle M(\omega)\rangle_\omega$ since modulation. This is the time-stretch dispersive Fourier transformation of the optical carrier [36, 37]. Simultaneously, note how in equation (2.10) each time point of the chirped modulation signal $s_{TS}(t)$ is now mapped to a stretched time $M(\omega_s)t$ of the carrier envelope; this is the generalized photonic time stretch process with arbitrary dispersion, which we call "warped time stretch", or "warped stretch".

It should be noted that, while SPA is necessary for the mathematical framework, in general, it need not be satisfied by the optical element that provides the temporal dispersion itself. For example, we will later demonstrate this for the case of time-stretch imaging, where the residual carrier dispersion D_1 can be very small and does not satisfy the SPA alone. However, modulation stretching still occurs due to the SPA being satisfied by the spatial dispersion induced by the grating pair. This spatial dispersion occurs in a different domain than the final information stretch, so while it satisfies the SPA condition for the time-stretch system, it is not included in the stretch factor. While SPA is necessary for the mathematical framework, in general, it need not be satisfied by the optical element that provides the temporal dispersion itself.

While we have derived the above expression using the stationary phase approximation in the so-called far-field regime, it can be considered a special case of the generalized dispersion Fourier transformation, in which this approximation need not hold true. In near-field conditions, there is no longer a one-to-one mapping between the optical spectrum and the recorded time-domain signal; thus, not only is the optical intensity required, but the envelope phase is also needed for the full reconstruction of the input signal. The extra requirement for near-field time stretch systems of capturing the envelope phase can be realized with coherent detection [38], with phase retrieval techniques from intensity measurements [13, 39–48]. While the stretch factor achieved under the near field regime is by definition smaller than that in the far-field, it is often sufficient in many applications for overcoming the bandwidth limitations of photodetection and signal digitization. Therefore, from a pragmatic standpoint, it is not strictly necessary to use large dispersion for overcoming speed bottlenecks with time stretch, despite the advantage of far-field regime in simplifying the signal detection and interpretation. Moreover, it is important to note that even though achieving a dispersive Fourier transform (i.e. frequency-to-time mapping) simplifies signal reconstruction and interpretation, it does not enable fast real-time measurements. Rather, the ability to slow down the waveform's timescale with dispersion is what overcomes the critical ADC speed bottleneck.

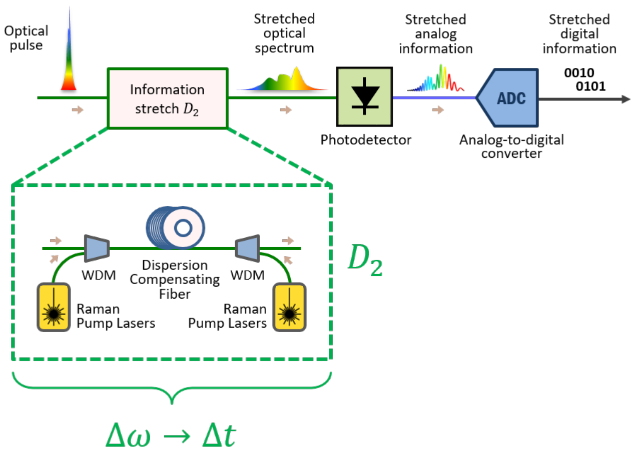

Figure 2.5: Schematic for time-stretch spectroscopy systems. An optical pulse is chromatically dispersed by a highly dispersive element (such as a dispersion compensating fiber, which can also allow for Raman amplification in tandem) with dispersion D_2. With sufficient dispersion, each individual optical wavelength is delayed to a different time. This enables the optical spectrum of ultrafast pulses to be recorded and digitized in real-time.

2.3 Analysis of incoherent time-stretch systems

2.3.1 Time stretch spectroscopy

Time stretch spectroscopy is at the heart and foundation of the photonic time-stretch technique. By passing the optical signal through a highly dispersive element, such as a dispersion compensating fiber, with dispersion D_2. With sufficient dispersion, each individual optical wavelength is delayed to a different time, effectively mapping the spectral information into time. To compensate for the spreading in power from large amounts of dispersion, distributed Raman amplification can also be introduced. In most cases, the original optical pulse has negligible dispersion compared to the introduced dispersion; therefore, the post-stretch information bandwidth is solely determined by the amount of applied dispersion D_2. We can then perform photodetection and A-to-D conversion using acquisition speeds matched to the post-dispersion bandwidth of the input pulse.

Since only a single dispersive element is introduced, there is technically no stretch factor applicable to this system. It can considered as a time-stretch system with a modulation function $s(t)$ of unity.

2.3.2 Time Stretch Enhanced Recorder (TiSER)

The Time-stretch Enhanced Recorder (TiSER) is the first example of a time-stretch system, applied to solve the speed limitations of electronic digitization. In TiSER-like systems, the source is stretched by a dispersion-compensated fiber (DCF) with group delay dispersion D_1, then modulated with an RF signal. The modulated optical signal is then stretched again with group delay dispersion D_2. The stretch factor [33], which in general we define as the ratio of the time-stretched output modulation relative to the unstretched input modulation, is:

$$M = \frac{D_1 + D_2}{D_1} = 1 + \frac{D_2}{D_1} \tag{2.12}$$

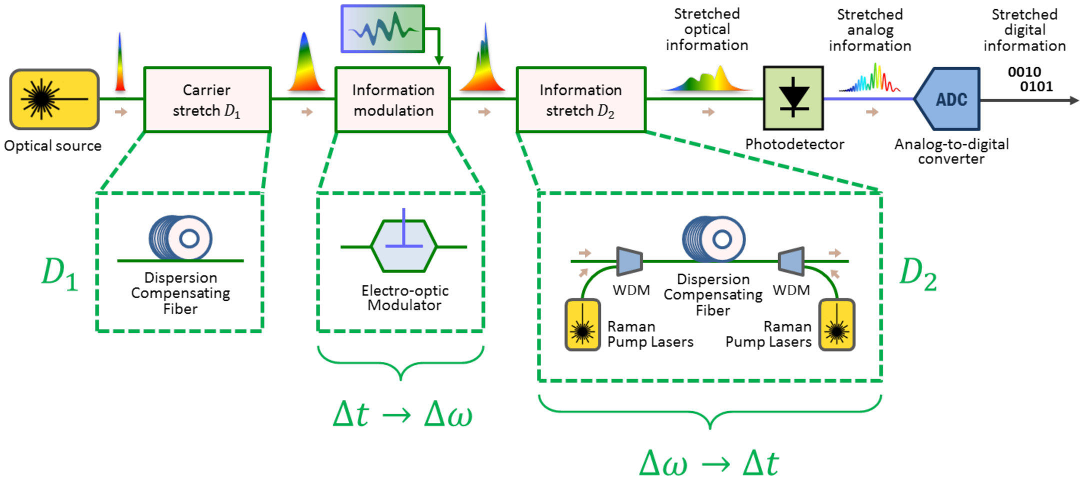

Figure 2.6: Schematic for TiSER-based systems. The broadband optical pulse is first dispersed with group delay dispersion D_1, then amplitude modulated by the input signal. This effectively maps the temporal RF input onto the optical spectrum, which can then be stretched via the second group delay dispersion D_2 to bridge the speed mismatch between the RF input and the digitizer. With distributed Raman amplification integrated into the second dispersive element, the SNR can also be maintained and not to be limited by the ADC bit depth post-stretch.

Even in its purest form, TiSER-like systems have been very successfully deployed in optical characterization and sensing applications. For example, the time-stretch accelerated processor (TiSAP) has been instrumental in [49], where eye diagrams and BER estimation was performed in real-time at 10 Gb/s on video-streaming UDP packets. In TiSAP and other applications using TiSER, the instrument operates in "burst mode", meaning that the high sampling rate provided by optically stretching an electrical signal is limited in duration by the repetition rate of the laser source.

While TiSER systems routinely use Mach-Zehnder modulators (MZMs) to map the electrical signal onto the optical carrier, the photonic time-stretch process is agnostic to the particular modulation technology. For example, electroabsorptive modulators or scattering events (such as in the case of time-stretch OCT or PDV) are possible signal modulation methods. Another possibility is with free-space nonlinear optical interactions, as is shown in [50], where, as an example, the Pockels effect was used to perform electro-optical sampling. In this way, terahertz radiation can be detected in real-time, which can be used for diagnostic applications in particle physics, such as those characterizing the micro-bunching effects of electron beams in cyclotrons [27].

The case of using four wave-mixing to achieve TiSER operation [51] as it requires modification to the stretch factor. The primary modification in the all-optical TiSER is the use of the nonlinear optical process of four wave mixing to replace the electro-optic modulator for imprinting the information onto the optical carrier. This allows the input signal to be optical instead of electrical.

Assuming negligible self-phase modulation and cross-phase modulation effects, the degenerate four-wave mixing process can be described by a set of three coupled first-order differential equations [52] as:

$$\begin{cases} \dfrac{\mathrm{d}E_p(z)}{dz} = \dfrac{3j\omega_p^2}{c^2 k_p^{(z)}}\chi_{\text{eff}} E_p^*(z) E_s(z) E_I(z) e^{-j\Delta kz} \\ \dfrac{\mathrm{d}E_s(z)}{dz} = \dfrac{3j\omega_s^2}{c^2 k_s^{(z)}}\chi_{\text{eff}} E_p^2(z) E_I^*(z) e^{-j\Delta kz} \\ \dfrac{\mathrm{d}E_I(z)}{dz} = \dfrac{3j\omega_I^2}{c^2 k_I^{(z)}}\chi_{\text{eff}} E_p^2(z) E_s^*(z) e^{j\Delta kz} \end{cases} \tag{2.13}$$

where $E_p(z)$, $E_s(z)$ and $E_I(z)$ are the pump, probe and idler electric fields, respectively. In this case, the probe electric field $E_s(z)$ is the input optical signal, and the idler wave $E_I(z)$ is the amplified and wavelength-shifted output field. Note that for simplicity, we have assumed negligible attenuation, self-phase modulation and cross-phase modulation effects. Since the pump field is broadband but the signal field is narrowband, the degenerate four-wave mixing process imprints the narrowband temporal input signal onto the stretched broadband carrier, where it can be further stretched with a second dispersive element.

If we further assume an undepleted carrier pulse over the entire length of propagation within the four-wave mixing modulator, we are reduced to only considering the interactions between the two latter coupled equations. In this case, the coupled equations can be solved analytically. After simplifying with the condition of perfect phase matching at $\omega_I = 2\omega_p - \omega_s$, we have:

$$\begin{cases} E_s(t;z) = E_s(t;0)\cos\kappa z \\ E_I(t;z) = \dfrac{3j\omega_I^2}{c^2 k_I^{(z)}} \dfrac{\chi_{\text{eff}}}{\kappa} E_p^2(z) E_s^*(t;0)\sin\kappa z \end{cases} \tag{2.14}$$

where $\kappa = 3\sqrt{\frac{\omega_s\omega_I}{c^2\epsilon_0 n_s n_I}}\chi_{\text{eff}} E_p^2$ is the coupling constant. After a distance equal to the coupling length $z = \ell_c \triangleq \frac{\pi}{2\kappa}$, we have $E_s(z = \ell_c) = 0$, and a complete energy transfer from input E_s to the output E_I occurs. This is the four-wave mixing based all-optical information modulation process.

The correct determination of the stretch factor is subtle, since the modulated chirped pulse is located in a range of optical wavelengths which is different and mutually exclusive from the initial stretched pulse. This manifests mathematically as a different frequency-to-time mapping for $E_I(t; z = \ell_c)$ and $E_p(t; z = \ell_c)$, respectively. The two quantities are related by:

$$E_I\left(\tau_{D1}\left(\frac{\omega_I+\omega_s}{2}\right); \ell_c\right) = \frac{3j\omega_I^2}{c^2 k_I^{(z)}}\frac{\chi_{\text{eff}}}{\kappa}E_p^2\left(\tau_{D1}(\omega_p-\omega_c); \ell_c\right)E_s^*(t; 0) \tag{2.15}$$

This can be rewritten more simply in the frequency domain as:

$$\begin{aligned}\tilde{E}_I\left(\Omega_I\right) &= \mathcal{F}_{\omega_I}\left\{\frac{3j\omega_I^2}{c^2 k_I^{(z)}}\frac{\chi_{\text{eff}}}{\kappa}E_p^2(t)E_s^*(t)\right\} \\ &= \frac{3j\omega_I^2}{c^2 k_I^{(z)}}\frac{\chi_{\text{eff}}}{\kappa}\int_{-\infty}^{+\infty}\tilde{E}_s^*(\Omega)\widetilde{E_p^2}(\Omega_I-\Omega)\frac{\mathrm{d}\Omega}{2\pi}\end{aligned} \tag{2.16}$$

Note how the definition of the Fourier transform operator for $\tilde{E}_I\left(\Omega_I\right)$ on the left hand side influences $\tilde{E}_s^*(\Omega)$ and $\widetilde{E_p^2}(\Omega_I-\Omega)$ on the right hand side to be expressed in terms of Ω_I instead of Ω_p.

Using the approximation $\widetilde{E_p^2} \approx \tilde{E}_i^2\left(\frac{\Omega}{2}\right)\exp 2j\phi\left(\frac{\Omega}{2}\right)$, the stretch factor M can now be shown to be:

$$\begin{aligned}M\left(\lambda_p\right) &= 1 + \frac{D_2(\Omega_I)}{\frac{1}{2}D_1\left(\frac{\Omega_I-\Omega}{2}\right)} \\ &\approx 1 + \frac{D_2\left(\lambda_I = \frac{\lambda_p\lambda_s}{2\lambda_s-\lambda_p}\right)\cdot\Delta\lambda_I}{D_1(\lambda_p)\cdot\Delta\lambda_p}\end{aligned} \tag{2.17}$$

where we have expressed D_1 in terms of λ_p and D_2 in terms of λ_I to reflect the extra time-stretching induced by the change in bandwidth in the degenerate four-wave mixing process, due to energy conservation. In most cases, since the optical bandwidth between the input and output remains unchanged, the $\Delta\lambda$ dependence can be cancelled to recover the usual stretch factor expression as before.

2.3.3 Single Shot Network Analyzer (SiNA)

Instead of considering photonic time-stretch as an optical bypass which enhance the bandwidth of electrical communications systems, one can also focus on its

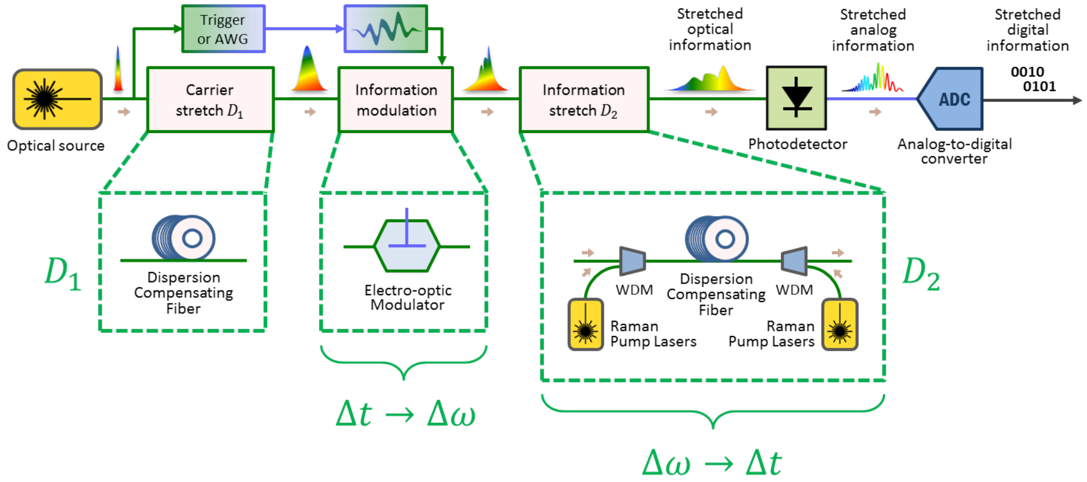

Figure 2.7: Schematic for the Single-shot Network Analyzer (SiNA) time-stretch system. An optical trigger is sent to a waveform generator to initiate an impulse response measurement of the device-under-test (DUT). The output response is modulated onto the D1 pre-stretched optical carrier by the TiSER-based time-stretch system, which slows down the electrical response of the signal via the dispersive element D_2. The electrical single-shot output of SiNA is the slowed temporal response of the DUT, which can then be measured and analysed in real-time.

single-shot nature, and the additional information this provides. The Single-shot Network Analyzer (SiNA) is a practical application which demonstrates the value in this change in perspective. Traditionally, network analyzers are limited by the digitization bandwidth, thus necessitating either a parallel array of ADCs (such as in LSNAs), each of which monitor a or require temporal multiplexing of the input test signal to the device under test (such as in vector network analyzers). Both of these traditional options are by definition not single-shot compatible, and are costly to scale.

In SiNA, the temporal response of the DUT is modulated onto the optical carrier and slowed down by the time-stretch system in real-time. This effectively removes removing increases the maximum measurable bandwidth of the DUT response, and allows for the recovery of the S-parameters in real-time.

Since the optical portion of the integrated system is functionally identical to that for the TiSER system, we have the same stretch factor M of:

$$M = 1 + \frac{D_2}{D_1}$$

where D_1 and D_2 are the first and second dispersive elements, respectively.

2.3.4 Time Stretch Accelerated Processor (TiSAP)

The Time-Stretch Accelerated Processor (TiSAP) is a generalization of the real-time system response characterization technique introduced by SiNA. Similar to SiNA, the focus in TiSAP is on the real-time processing of wideband signals, one application is real-time optical performance monitoring (OPM) of ultrafast data transmissions by means of relieving the digitization bandwidth bottleneck. When generalized to pseudo-random electrical inputs, such an integral optoelectronic system can be considered as an applied to optical performance monitoring (OPM).

In TiSAP, the optically-triggered digital pseudo-random bit sequence (PRBS) is time-stretched by a TiSER-based optical system. The slowed-down PRBS is

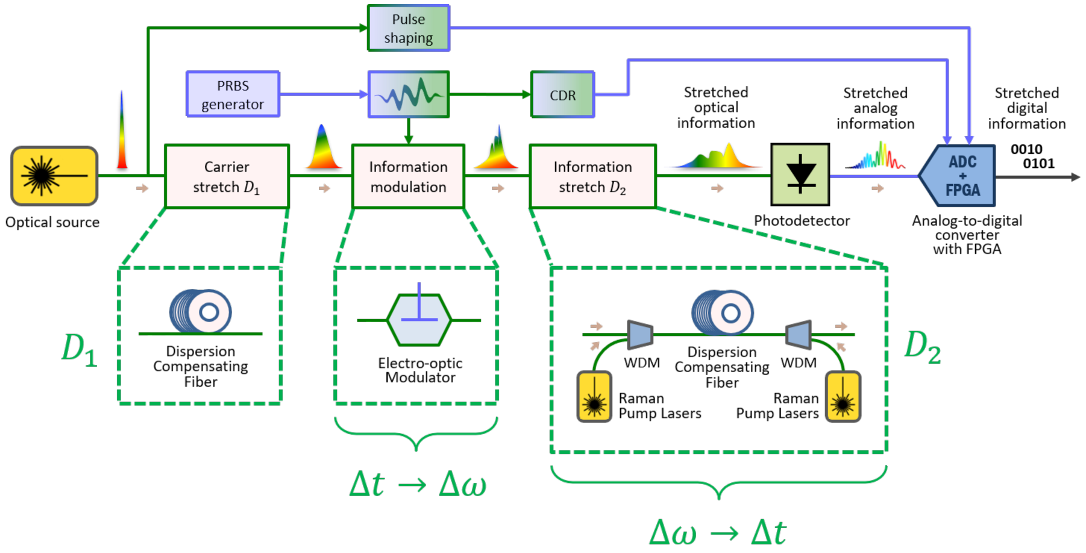

Figure 2.8: Schematic for the time-stretch accelerated processor (TiSAP) for optical performance monitoring. For proof-of-concept, a pseudo-random bit sequence (PRBS) representing a real-world digital input is generated and modulated onto an optical carrier which is pre-chirped with the dispersive element D_1. The optical chirped pulse is then stretched by a second dispersive element D_2, stretching the signal before being captured by the photodetector. An FPGA provides pulse shaping and clock data recovery to the stretched PRBS input under feedback, then finally digitized with an ADC at a lower, time-stretched bandwidth.

then used at the ADC along with a synchronized pulse-shaping and clock data recovery (CDR) process which is implemented directly in the ADC via an FPGA. The monitoring can thus be provided that is synchronized, real-time and also in-service, while eliminating read-write transfer bottlenecks of digital monitoring systems, and processing latencies from software-based alternatives.

Since the optical portion of the integrated system is functionally identical to that for the TiSER system, we have the same stretch factor of:

$$M = 1 + \frac{D_2}{D_1}$$

2.3.5 Time Stretch Imaging

In time-stretch imaging, also known as Serial Time-Encoded Amplified Microscopy (STEAM), the source spectrum first undergoes (optional) chromatic dispersion D_1, then mapped into space a diffraction grating pair with line spacing d. The optical carrier is then imprinted with the spatial information of the sample via scattering. After target modulation, the optical signal is stretched again with group delay dispersion D_2.

From an information perspective, we are shifting the domain in which the information resides, and each time this is done, we obtain a degree of freedom in scaling the conversion factor with the device parameters. In TiSER, both the input (analog RF signal) and the output (optical pulse) reside in the temporal domain, which is mediated by a frequency-to-time mapping achieved by direct RF modulation on the pre-chirped optical spectrum. In general, however, other implementations may have differing initial and final information domains (e.g. in STEAM-based line-scan imaging systems), or the information modulation may not be performed directly on the optical spectrum (e.g. in coherent TiSER and PDV). We will later show in our discussion of coherent time-stretch systems that it is also instructive to define a generalized group delay dispersion parameter which

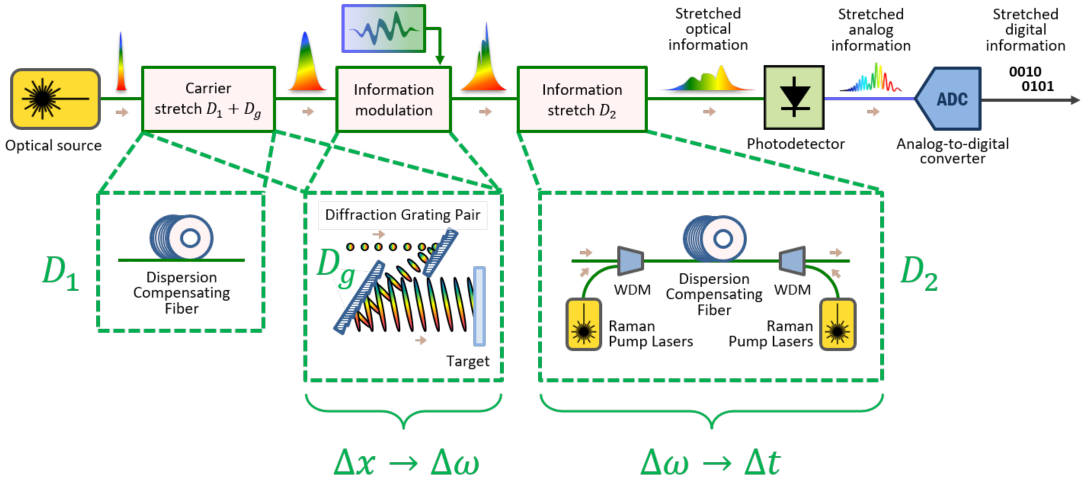

Figure 2.9: Schematic for STEAM-based line-scan imaging systems. After passing through an optional dispersive element D_1, the broadband optical pulse is spatially dispersed with a diffraction grating pair to obtain a line-scan image of the target. The wavelength-dependent path difference creates a group delay dispersion D_g, which is doubled in the return path. The spatial information is now mapped onto the optical spectrum, which is then stretched via the second group delay dispersion D_2 (with integrated distributed Raman amplification), further mapping the spatial information into time, enabling ultrafast, single-shot serial readout of the spatial line-scan image.

encompasses alternative time-stretch modalities.

For spatial diffraction, we consider a pair of parallel gratings with groove period d and inter-grating distance L, with the incident optical pulse at an angle θ_i relative to the grating normal. Each grating obeys the grating equation for the diffraction angle θ_m of order m; that is:

$$\sin\theta_m + \sin\theta_i = m\lambda \tag{2.18}$$

The diffraction grating provides two sources of chromatic spread. The first is a temporal delay τ_G (relative to the wavelength $\lambda_0 \triangleq \frac{d}{m}\sin\theta_i$) corresponding to the front pulse tilt of the grating:

$$\Delta\tau_G(\lambda) = \frac{nL}{c}\left[(\sec\theta_m - 1) + \sin\theta_m \sin\theta_i\right] \tag{2.19}$$

The second is the spatial diffraction D_x, parallel to the surface of the target. Following the process in Section 2.2, we model this as a wavelength-dependent spatial shift $X_G(\lambda)$ (again, relative to the wavelength λ_0), where:

$$X_G(\lambda) = L\cos\theta_i \frac{m(\lambda - \lambda_0)}{d} \tag{2.20}$$

Under the linear optics assumption, the spatial and temporal domains do not interact (i.e. $\tilde{E}_i(x,t) = |E_i(x - x_i)|\, e^{jk_x(x-x_i)} \cdot |E_i(t)|\, e^{j\omega_c t}$). Assume WLOG that we do not include any additional temporal pre-modulation dispersion D_1. Then, after the diffraction grating, we have:

$$\tilde{\tilde{E}}_{D1}(k_x, \omega - \omega_c) = \left|\tilde{\tilde{E}}_i(k_x, \Omega)\right| e^{j\int X_G(k_X)dk_x} e^{j\int \tau_G(\Omega)d\Omega} \tag{2.21}$$

where $\tilde{\tilde{E}}_{D1}(k_x, \omega - \omega_c)$ is the electrical field spectrum in both k- and ω-space (with units of $\left[\frac{\mathrm{V}}{\mathrm{m\cdot Hz\cdot nm^{-1}}}\right]$). Using the stationary phase approximations $x = X_G(k_s)$ and $t = \tau_G(\omega_s)$, we can write the output electric field as:

$$\begin{aligned} E_G(x[t(\lambda)]) = &\left[\frac{\left|\tilde{\tilde{E}}_i(k_s, \omega - \omega_c)\right|}{\sqrt{2\pi|X'_G(k_s)|}} \exp\left(j\int X_G(k_s)dk_s - jk_s x - j\frac{\pi}{4}\right)\right] \\ &\cdot \left[\frac{1}{\sqrt{2\pi|\tau'_G(\omega_s)|}} \exp\left(j\int \tau_G(\omega_s)d\omega_s - j\omega_s t - j\frac{\pi}{4}\right)\right] \end{aligned} \tag{2.22}$$

Note that the time and space mappings have a one-to-one correspondence with one another via the dispersion relation $\omega_s = c\,k_s$; that is:

$$x = X_G\left(\frac{\tau_G^{-1}(t)}{c}\right) \tag{2.23}$$

Also note how the dimensional inter-dependence is reflected in the nested coordinate $x[t(\lambda)]$; this multi-dimensional mapping will be further discussed in the Chapter 3, where we liken this operation to a mechanical gearbox for transmission. The signal $s(x)$ is now imprinted onto the spatial beam, and we have $E_M((x[t(\lambda)]) = E_G((x[t(\lambda)]) \cdot s(x[t(\lambda)])$. After the inverse grating diffraction, the spatial diffraction is undone, removing the time dependence on the spatial coordinate, and the modulation $s(t)$ is now only dependent on time. We hence only need to consider the temporal dispersion for the stretch factor. Following (2.6) the temporally stretched electric field signal can be written as:

$$\tilde{E}_M(x,\omega) = E_i(x-x_i)\cdot\int_{-\infty}^{+\infty}\tilde{E}_i(\Omega_I-\Omega)e^{j\int 2\tau_{D1}(\Omega_I-\Omega)\,\mathrm{d}(\Omega_I-\Omega)}\cdot\tilde{s}\left(\Omega(\mu)\right)\frac{\mathrm{d}\Omega}{2\pi} \tag{2.24}$$

Note the lack of spatial diffraction and that the temporal dispersion has been doubled. The signal is now mapped onto the spectrum, and further derivations follow as before. The stretch factor is therefore:

$$M = \frac{2(D_1 + D_g) + D_2}{D_1 + D_g} = 1 + \frac{D_2'}{D_1'} \tag{2.25}$$

where $D_1' = D_1 + D_g$ is the total pre-modulation dispersion, and $D_2' = D_1 + D_g + D_2$ is the total post-modulation dispersion.

2.3.6 Stretch-encoded angular light scattering

In time-stretch angular light scattering systems, the input broadband pulse is first spatially dispersed by a diffraction grating, then focused by an objective lens onto the scattering sample. Assuming the wavelength dependence of the angular scattering is negligible over the optical bandwidth, the measured spectrum at a

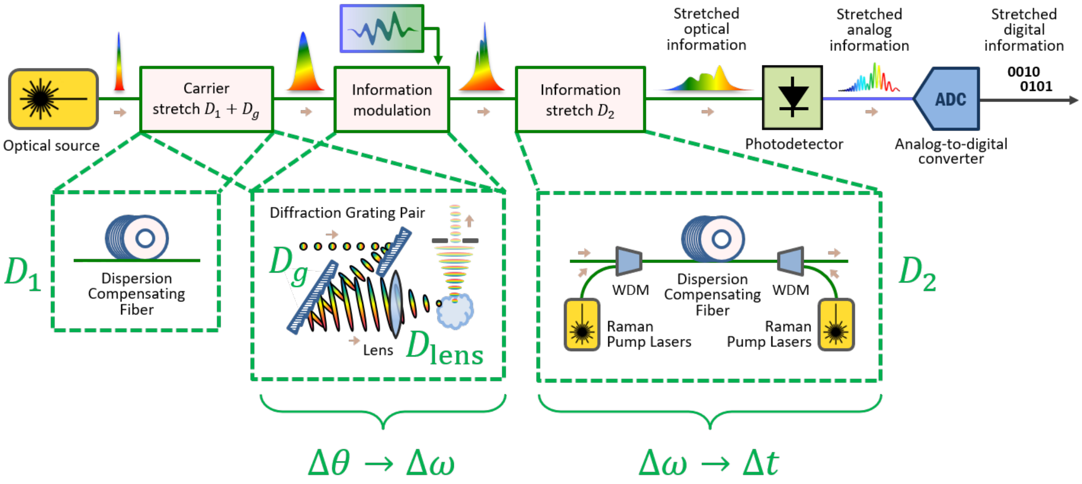

Figure 2.10: Schematic for stretch-encoded angular light scattering systems. After passing through an optional dispersive element D_1, the broadband optical pulse is spatially dispersed by a diffraction grating pair, where the wavelength-dependent path difference adds an additional group delay dispersion D_g. The spatial rainbow is then focused onto the target and the side-scattering is recorded. Since rainbow is narrowband, the wavelength dependence on the scattering intensity is negligible; therefore, the angular information is now mapped onto the optical spectrum. By further stretching via the second group delay dispersion D_2 (with integrated distributed Raman amplification), further mapping the spatial information into time, enabling ultrafast, single-shot serial readout of the spatial line-scan image.

fixed angle from the sample represents the angular spectral response of the sample, which is mapped onto the optical spectrum. Therefore, after coupling back into a fiber, the optical spectrum can then be stretched, and enable the single shot capture of the angular scattering response from a point source (which can then be scanned over the object of interest). However, unlike the case of time stretch imaging with STEAM, here we need to include the phase response of the lens and model the angular scattering of the sample at a given measurement angle θ.

After the application of the first dispersive element D_1 and diffraction grating, we recover Equation (2.21). The broadband pulse then enters into a (thin) convex cylindrical lens, modelled by the Fresnel diffraction integral as a complex transmittance a_{lens}:

$$a_{lens}(x,\omega) = \exp\left(-j\frac{\omega x^2}{2cf}\right)\exp\left(j\frac{2\pi n\Delta_0}{\lambda}\right) \tag{2.26}$$

where $\frac{1}{f} = (n-1)\left(\frac{1}{R_1} - \frac{1}{R_2}\right)$ is the inverse of the focal length, R_1 and R_2 are the focal radii of curvatures of the front and back lens surfaces respectively, and $\Delta_0 = \Delta_1 + \Delta_2$ is the lens thickness (assuming overlapping principal planes of thicknesses Δ_1 and Δ_2). WLOG, we will omit the constant phase term $\exp\left(j\frac{2\pi n\Delta_0}{\lambda}\right)$ hereon.

After transmission through the thin lens, the free-space propagation to the focal plane $z_I = f$ adds a angle- and wavelength-dependent phase shift $\Delta\phi$, where:

$$\begin{aligned} e^{j\Delta\phi(x,\omega)} &= \exp\left[j\frac{2\pi}{\lambda}\sqrt{x^2 + \left(f - \Delta_2 + \frac{x^2}{2R_1}\right)^2}\right] \\ &\approx \exp\left[j\frac{\omega}{c}\left(f + \frac{x^2}{2f}\right)\right] \end{aligned} \tag{2.27}$$

We can see that the cylindrical lens cancels out the spatial diffraction created by the grating (and ignore the constant contribution from the free space propgation inthe z-direction). Each spatially separated wavelength is now mapped to a unique angle θ, where $\theta = \tan^{-1}\left(\frac{X_G(\lambda)}{f}\right)$ is the incidence angle (relative to the optical axis) to the sample in focus, and X_G is defined in the previous section in

Equation (2.20). The optical pulse can now be written as:

$$\tilde{E}_{D1}(\theta(\omega)) = \left|\tilde{E}_i(\theta, \Omega)\right| e^{j\int(\tau_G(\Omega)+\tau_{D1}(\Omega))d\Omega} \tag{2.28}$$

After interaction with the sample, for a given fixed output measurement angle θ_o, the sample imparts a complex and angular response $\tilde{s}(\theta_o + \theta(\omega))$ to the wavelength corresponding to the incidence angle θ; we thus have:

$$\tilde{E}_I\left[\theta_0(\omega)\right] = \int_{\Delta\theta} s(\theta_o + \theta)\tilde{E}_{D1}(\theta(\omega))d\theta(\omega) \tag{2.29}$$

This recovers the modulation step in Equation (2.6), but with the convolution in the angular domain. Since the signal is now mapped onto the spectrum, the derivations again follow from the post-dispersion derivations for TiSER. The stretch factor is therefore:

$$M = \frac{D_1 + D_g + D_2}{D_1 + D_g} = 1 + \frac{D_2}{D_1'} \tag{2.30}$$

where $D_1' = D_1 + D_g$ is the total pre-modulation dispersion.

2.3.7 Coherent systems

Thus far, we have described time-stretch systems in which the information is directly encoded onto the spectral envelope. In fact, the envelope phase can also be time-stretched, provided that there is a method to convert the phase information into amplitude information. By far the most common way to do so is via interferometry, or more precisely, spectral interferometry, since the encoded pulses are chromatically dispersed.

Figure 2.11 shows an overview of the coherent time-stretch process. The process is the same, except that the information modulation step in Figure 2.3 has been replaced by spectral interferometry. There is no requirement on the specific interferometric setup, as long as this mapping can be achieved.

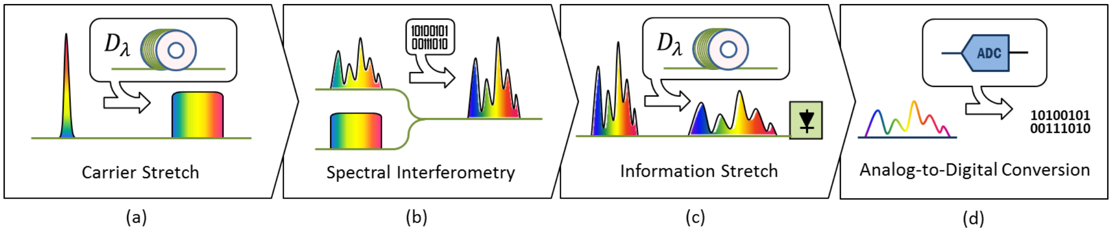

Figure 2.11: Overview of the coherent time-stretch process. (a) The wideband optical carrier is chromatically dispersed by a dispersive element. (b) Information is encoded onto the optical spectrum amplitude via spectral shearing. Since the carrier is previously dispersed, the temporal amplitude modulation now has a one-to-one correspondence to the carrier wavelengths. (c) With frequency-to-time mapping of the information in place, further chromatic dispersion now slows down the modulated signal in real time. (d) By tuning the ratio of group velocity dispersion between the two dispersive elements, the speed of the input signal can now match that of the analog-to-digital converter (ADC).

There are two main ways in which spectral interferometry may be introduced to coherent photonic time-stretch. One is by introducing signal-dependent phase delays in the signal arm of the interferometer via interaction with the sample, which beats in the intensity after recombining with the reference arm at the frequency $\Omega_B = \frac{t_2-\beta_1 L}{\beta_2 L} - \frac{t_1-\beta_1 L}{\beta_2 L} = \frac{2\pi c}{n\lambda_0^2}\frac{\Delta\tau}{D}$, where D is the group delay dispsersion. In this case, the beat frequency, which encodes the delay information, is slowed by a factor of D. This is the strategy employed by time-stretch optical coherence tomography (OCT), as well as the coherent version of TiSER. In this case, is appropriate to define a "beat frequency group delay dispersion" $D_B = \frac{\mathrm{d}\tau}{\mathrm{d}\Lambda_B}$ to reflect the domain in which the information is encoded (Λ_B is the beat period, where $\Lambda_B = \frac{2\pi}{\Omega_B}$).

The second method is to induce wavelength changes in the optical spectrum via interaction with the sample. This is the strategy employed by time-stretch photon Doppler velocimetry (PDV). Since there is an ambiguity in the frequency-to-time mapping, we can always define an effective time delay, such that $\frac{\Delta\tau_{\text{eff}}}{D} = \Delta\omega_D$, where $\Delta\omega_D$ is the Doppler shift.

2.4 Analysis of coherent time-stretch systems

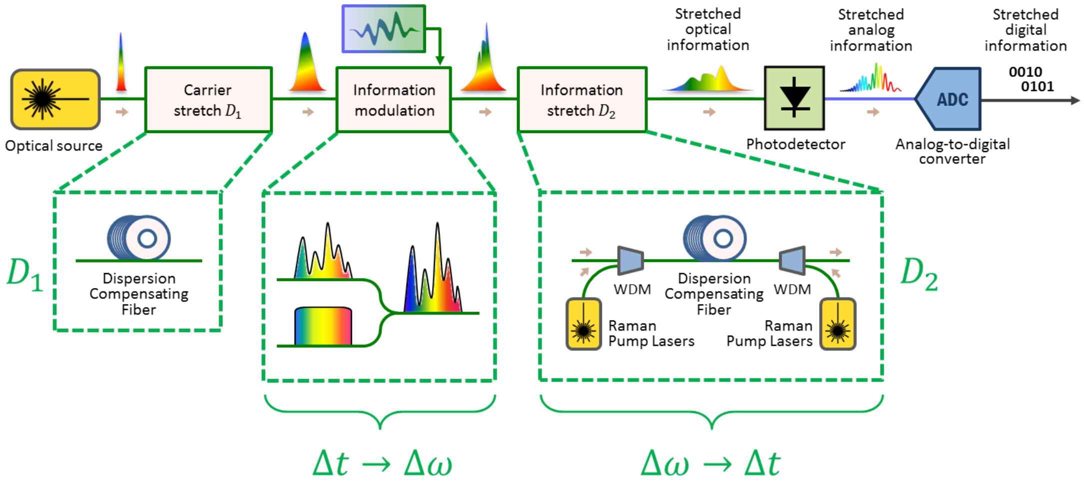

Figure 2.12: Schematic for coherent TiSER systems. A supercontinuum pulse is first dispersed with a dispersive element. The pulse then enters into an interferometric setup, and the sample arm is imprinted with coherent target information, while the other arm is unmodulated, but delayed by $\Delta\tau_{IF}$ to tune the heterodyne baseband frequency. When recombined with the reference arm, the interference causes the delay information to be mapped to the interference pattern in the optical intensity. The pulse intensity is then separated into its complementary (90°-shifted) counterpart for digital lock-in phase reconstruction.

In the coherent version of TiSER [13], a transform-limited broadband source $\left|\tilde{E}_i(\omega)\right|$ is dispersed by a highly dispersive element. Similar to time-stretch OCT, the precise location of the dispersion does not matter, but typically a small group delay dispersion D_1 to lower the peak power is preferred before the sample so as to compromise in terms of the integration time; the rest of the desired dispersion can be placed post-signal as D_2 after the interferometric setup (optionally with integrated distributed Raman amplification), which stretches the intensity modulation. Alternatively, as is the case in time-stretch OCT, we can instead consider installing matched dispersion fibres on each of the reference and signal arms. This configuration is useful for performing signal-only Raman amplification, which necessitates the addition of a pumped fibre in the signal arm anyway.

After entering into the interferometric setup, the pulse in the sample arm is encoded with coherent modulation (both in amplitude and phase). For example, in the case of an absorption event near $\lambda = \lambda_a$, the amplitude approaches zero, while a strong shift is induced in the phase.

After exiting the Mach-Zehnder interferometer, the beat intensity $I_{beat}(t)$ can be shown to be:

$$\begin{aligned} I_{beat}(t) &\propto \left|E_{D2}(t+\Delta\tau_{IF}) + E_{D2}(t)\right|^2 = \left|\mathcal{E}_{D2}(t+\Delta\tau_{IF})\right|^2 \left(1 + |s_M(t)|^2\right) \\ &+2\left|\mathcal{E}_{D2}(t+\Delta\tau_{IF})\right|^2 |s_M(t)| \cos\left[\frac{\pi}{4} + \measuredangle\tilde{s}\left(\frac{t}{M\beta_2 L_2}\right) - \frac{t^2}{2M\beta_2 L_2} + \frac{2\Delta\tau_{IF}t + \Delta\tau_{IF}{}^2}{2\beta_2 L_{tot}}\right] \end{aligned} \tag{2.31}$$

From the last expression in Equation 2.31, we can see that the stretch factor is the same for both the amplitude and phase modulation. Namely, it is:

$$M = 1 + \frac{D_2}{D_1}$$

2.4.1 Time-stretch optical coherence tomography (OCT)

In time-stretch OCT, a supercontinuum source is reflected by the sample at different depth layers, mapping the depth information $z(\Delta\tau)$ into time delays $\Delta\tau = \frac{2n\Delta z}{c}$ (relative to the reference beam). We first consider the case where dispersion D_2 is installed entirely before or after the interferometric setup [15], as shown in Figure 2.13. To maximize the “shutter speed” (i.e. minimize dwell time), it is preferable to allocate the dispersion entirely to after the signal modulation process. However, a small amount of dispersion D_1 should still be allocated pre-

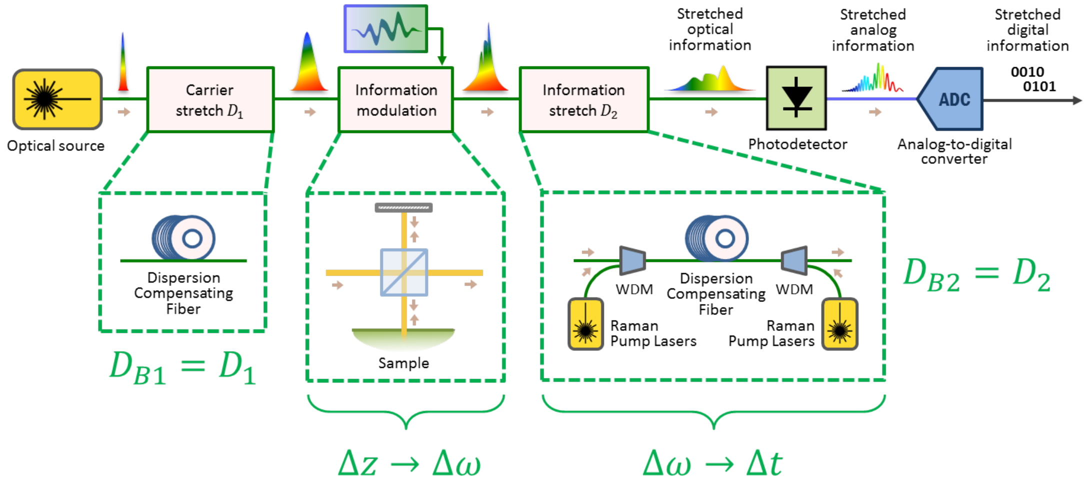

Figure 2.13: Schematic for time-stretch OCT systems. A supercontinuum pulse is first dispersed with a dispersive element with small group delay dispersion D_1 to lower the peak power without excessive compromise in the integration time. The pulse then enters into the interferometric setup. In the sample arm, the different depth layers of the sample reflect pulses at increasing time delays. When recombined with the reference arm, the interference causes the delay information to be mapped to beat frequencies in the optical intensity. By treating the interference as amplitude modulation, the pulse is then stretched via the second group delay dispersion D_2 (with integrated distributed Raman amplification), further mapping the depth information into time and enabling ultrafast, single-shot serial readout of the sample depth scan. Akin to swept-source OCT, the digital readout is then numerically Fourier-transformed to obtain the direct depth reflectivity profile.

signal to adjust the peak power to that below the damage threshold of the sample. When the supercontinuum rainbow is stretched by the introduction of group delay dispersion D_1, the the time delays $\Delta\tau$ are then mapped to beat wavelengths $\Lambda_B = \frac{2\pi}{\Omega_B}$ as:

$$\Delta\tau = \frac{n\lambda_0^2 D_1}{c\Lambda_B} \tag{2.32}$$

i.e. the reference and signal beams will beat with one another at the beat frequency $\Omega_B = \frac{t_2-\beta_1 L}{\beta_2 L} - \frac{t_1-\beta_1 L}{\beta_2 L} = \frac{2\pi c}{n\lambda_0^2}\frac{\Delta\tau}{D_1}$, which is slowed by a factor of D_1. (Note that apart from the signal-to-reference beating, we also have signal-signal self-beating "noise", but as the reflected power is much lower than the reference beam power, this can be neglected.) Since the depth information is fundamentally encoded in the time delays of the signal beam, it is appropriate to define a "beat frequency group delay dispersion" $D_B = \frac{\mathrm{d}\tau}{\mathrm{d}\Lambda_B}$ to reflect the domain in which the information is encoded. Fortunately, as shown in the equation above, the beat frequency GDD simply equals that of the total dispersion up to that point.

Also noted is that the information encoding process is time-invariant to changes by chromatic dispersion, so in principle the placement of the dispersion in the beam path does not matter, so long as the reference and signal beams receive the same amount of dispersion. The axial range Δz and resolution δz are therefore:

$$\Delta z = \frac{c\Delta\tau_{\max}}{2n} = \frac{c}{2n}(D_1 + D_2)\Delta\lambda \tag{2.33}$$

$$\delta z \geq 8\ln 2\sigma_z^2 = \frac{8\ln 2\, c\, D_1}{(D_1 + D_2)\sigma_\omega^2} = \frac{2\ln 2 D_1}{\pi(D_1 + D_2)}\frac{\lambda_0^2}{\Delta\lambda} \tag{2.34}$$

where σ_z and σ_ω is the half-linewidth (standard deviation) of the broadband optical signal in the spatial and spectral domains, respectively, where we have assumed a Gaussian temporal profile.

From Equation (2.34), we can see that the stretch factor is equal to that of TiSER:

$$M = \frac{D_{B2}}{D_{B1}} = 1 + \frac{D_2}{D_1} \tag{2.35}$$

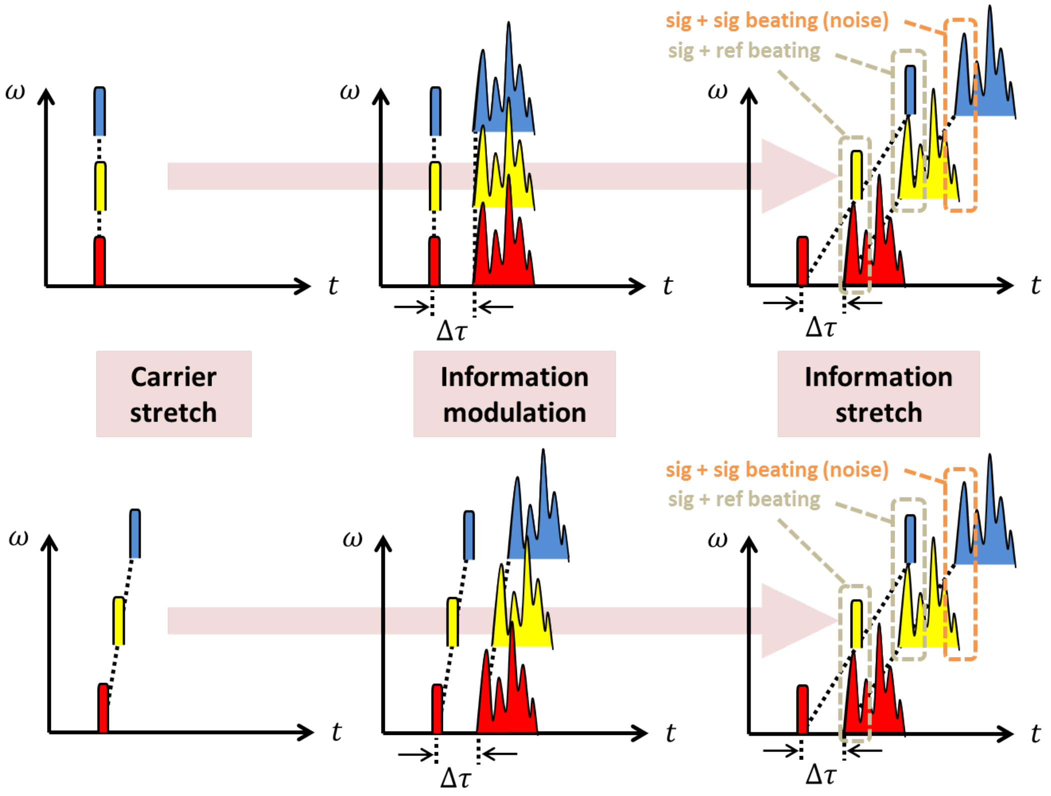

Figure 2.14: Illustration for the mechanism of post-signal dispersion in providing the information stretch. Since the signal is encoded in terms of delays of the signal arm relative to the reference arm, the precise position of the group delay dispersion (whether pre- or post-signal) does not matter to the amount of stretch generated, as long as both the signal and reference arms are affected equally.

Alternatively, we can consider the case of [14], where matched dispersion fibres are located on each of the reference and signal arms in a Michelson interferometer configuration. This configuration is useful if we want to perform signal-only Raman amplification, which necessitates the addition of a pumped fibre in the signal arm anyway. Since the self-beating signals are also amplified, optical filtering is required, typically after the reference arm is time-shifted by an amount larger than that corresponding to the total axial distance probed (at the cost of increasing the maximum beat frequency).

Since the Michelson configuration is used for the interferometer, the stretch factor (if pre- or post-signal dispersion is not considered) reduces to $M = \frac{D_1+D_1}{D_1} = 2$.

2.4.2 Time-stretch vibrometry and broadband laser ranging (BLR)

Similar to time-stretch OCT, time-stretch vibrometry relies on time delays between the signal and reference arm in the interferometer. Like OCT, the target is located at a fixed distance from the measurement location, but unlike OCT, the target surface has much greater reflectivity and the varying time delays from the sample arm are caused by standing-wave vibrations on a reflective surface. Alternatively, in broadband laser ranging (BLR), time delays can be introduced by the movement of the target in the direction of measurement, which are too slow to affect a significant Doppler effect.

While here we focus our attention in describing the case of vibrometry, in both cases the resultant beat frequency at the output of the interferometer can be described as follows:

$$\Omega_B = \frac{2\pi}{\Lambda_B} = \frac{4\pi^2 c}{n\lambda_0^2 D_1}\Delta\tau \tag{2.36}$$

As was the case for time-stretch OCT, the reference and signal beams will beat at the frequency $\Omega_B = \frac{2\pi c}{n\lambda_0^2}\frac{\Delta\tau}{D_1}$, which is slowed by diserpsion by a factor of

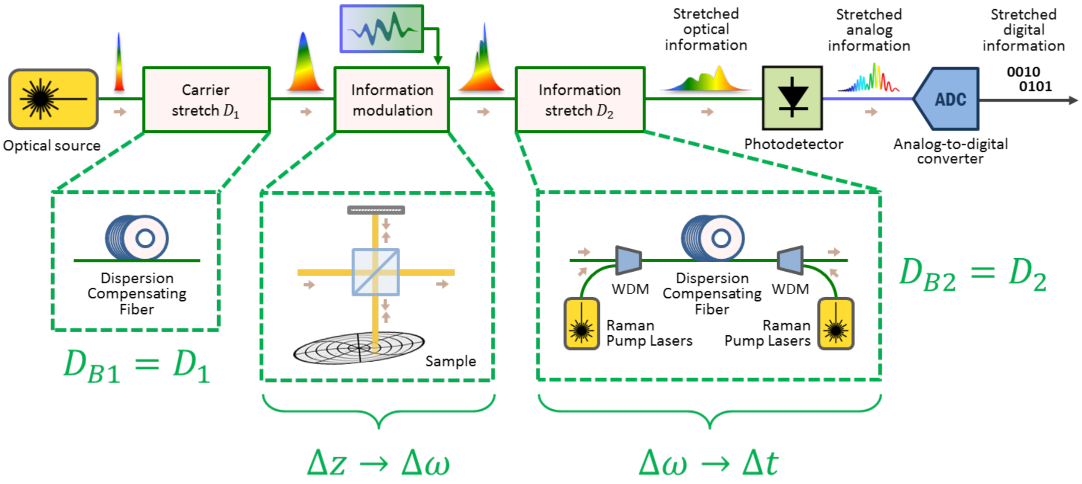

Figure 2.15: Schematic for time-stretch vibrometry systems. A supercontinuum pulse is first dispersed with a dispersive element with small group delay dispersion D_1 to lower the peak power without excessive compromise in the integration time. The pulse then enters into an interferometric setup. In the sample arm, the movement of the target reflects incoming pulses at fluctuating time delays. When recombined with the reference arm, the interference causes the delay information to be mapped to beat frequencies in the optical intensity. By treating the interference as amplitude modulation, the pulse is then stretched via the second group delay dispersion D_2 (with integrated distributed Raman amplification), further mapping the depth information into time and enabling ultrafast, single-shot serial readout of the sample depth scan. Akin to swept-source OCT, the digital readout is then numerically Fourier-transformed to obtain the direct depth reflectivity profile.

D_1, and so we can define a "beat frequency group delay dispersion" $D_B = \frac{\mathrm{d}\tau}{\mathrm{d}\Lambda_B}$ to reflect the interferometric domain in which the information is encoded, as was done for time-stretch OCT. For the case of vibrometry, the beat frequency GDD simply equals that of the total dispersion up to that point, which includes both the single-pass temporal dispersion D_g from the diffraction grating (as shown in Subsection 2.3.5) and the dispersion D_1 from the pre-signal DCF.

Following the same analysis as in time-stretch OCT, this gives us the stretch factor of:

$$M = 1 + \frac{D_{B2,\mathrm{tot}}}{D_{B1,\mathrm{tot}}} = 1 + \frac{D_g + D_2}{D_g + D_1} \approx 1 + \frac{D_2}{D_1} \tag{2.37}$$

2.4.3 Time-stretch Photonic Doppler velocimetry (PDV)

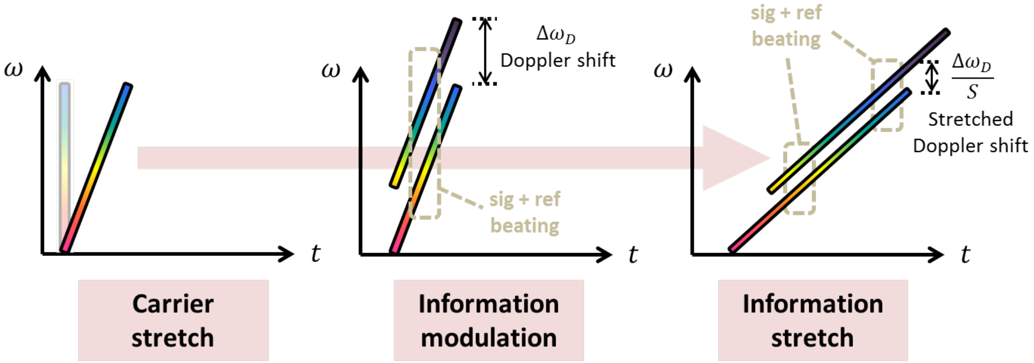

Figure 2.16: Mechanism of time-stretch photon Doppler velocimetry. The broadband optical carrier pulse is first stretched by a dispersive element D_1, and then enters into a interferometric setup. One of the arms impinges on a moving target, which imparts a Doppler shift $\Delta\omega_D$ on the pulse and shifts the spectrum in accordance with the velocity in the direction of measurement. After recombining with the reference pulse, the velocity information is encoded onto the optical intensity via beating between the signal and reference beams. The beating frequency can then be stretched via a second dispersive element D_2.

Time-stretch photon Doppler velocimetry (PDV) is the photonic time-stretch setup which measures the velocity profile of a moving object (along the direction of measurement) based on the Doppler shift of the optical beam that reflects from the target. The setup used is the same as that in Figure 2.16, except that target is replaced with a moving target.

In time-stretch PDV, the broadband optical carrier pulse is first stretched by a dispersive element D_1, and then enters into an interferometric setup. One of the interferometric arms impinges on a moving target, which imparts a Doppler shift $\Delta\omega_D$ on the pulse and shifts the spectrum in accordance with the velocity in the direction of measurement, given by:

$$\Delta\omega_D = \frac{4\pi v_D}{\lambda_0} \tag{2.38}$$

where v_D is the velocity of the target along the direction of measurement. At this point, each optical frequency in the Doppler-shifted arm is delayed by $\Delta\tau$ relative to the same frequency in the reference arm of the interferometer, which is determined by the first dispersive element, as in time-stretch OCT:

$$\Delta\tau = D_1\lambda_D = \frac{n\lambda_0^2 D_1}{2\pi c}\Delta\Omega_D = \frac{2n\lambda_0 D_1}{c}v_D \tag{2.39}$$

After recombining with the reference pulse, the velocity information is encoded onto the optical intensity via beating between the signal and reference beams. Since the same optical frequency gets delayed by the same amount regardless of where it is in time, the relative delay between the two pulses will be kept constant as they pass through the second dispersive element D_2. The beating frequency can therefore be stretched by the second dispersive element , giving us:

$$\Delta\omega_(D, S) = \frac{2\pi c}{n\lambda_0^2}\frac{\Delta\tau}{D_1 + D_2} = \frac{D_1}{D_1 + D_2}\frac{4\pi v_D}{\lambda_0} \tag{2.40}$$

From Equation (2.40), we see that the pulse is now slowed down by the stretch factor M, where:

$$M = 1 + \frac{D_2}{D_1}$$

2.5 Conclusion

We thus achieve a unified theory of warped time stretch in describing the output temporal signal after time-stretch operations, in terms of an arbitrary dispersion $\beta(\omega)$ (corresponding to the group delay $\tau(\omega)$). We also provided an overview for various optical systems for telecommunications, imaging, sensing which utilize photonic-time stretch as a critical component of their setup. From there, a unified framework for time-stretch systems was demonstrated, including incoherent systems such as TiSER and STEAM, as well as coherent systems, such as time-stretch OCT, coherent TiSER and time-stretch PDV. The abstracted mathematical description also identifies the smoothness assumptions which must to be satisfied in order to generalize from photonic time stretch to warped dispersive profile, and the resultant mathematical frramework is blose flexible and general. In particular, it was shown that the key parameter to photonic time-stretch is a proper definition of the stretch factor; in fact, all time-stretch systems can have their stretch factors described in the following form: $M\left[t(\lambda)\right] = 1 + \frac{D_2(\lambda)}{D_1(\lambda)}$.

CHAPTER 3

Gearbox analogy for engineering temporal pulse shapes with dispersion

3.1 Introduction

In the physical world, processes often occur at time scales that are too fast to be captured and processed by electronic circuitry. This is certainly the case in optics where the duration of laser pulses that are used for spectroscopy and sensing are several orders of magnitude faster than the fastest electronic digitizers and processors.

All measurement systems employ an analog to digital converter (ADC) for digitization and subsequent storage and processing of information. While there are several factors that can limit the performance of a measurement instrument, at high speed it the speed and the accuracy of the ADC that is the bottleneck. Specifically, there exists a sampling mismatch between the speeds of signal and that of the ADC. To alleviate this problem, Photonic Time Stretch, an analog slow motion technique, was introduced in the 1990s [10, 11]. In photonic time stretch, an optical fiber with large chromatic dispersion is used to slow down wideband optical signals that are encoded on the optical spectrum. The immediate yet powerful consequence of the temporal gearbox in bridging the speed mismatch between fast optical signals and slow ADCs is the ability to perform ultrafast optical measurements in a single-shot fashion.

For extended measurements of ultrafast optical signals, there is a need to tailor

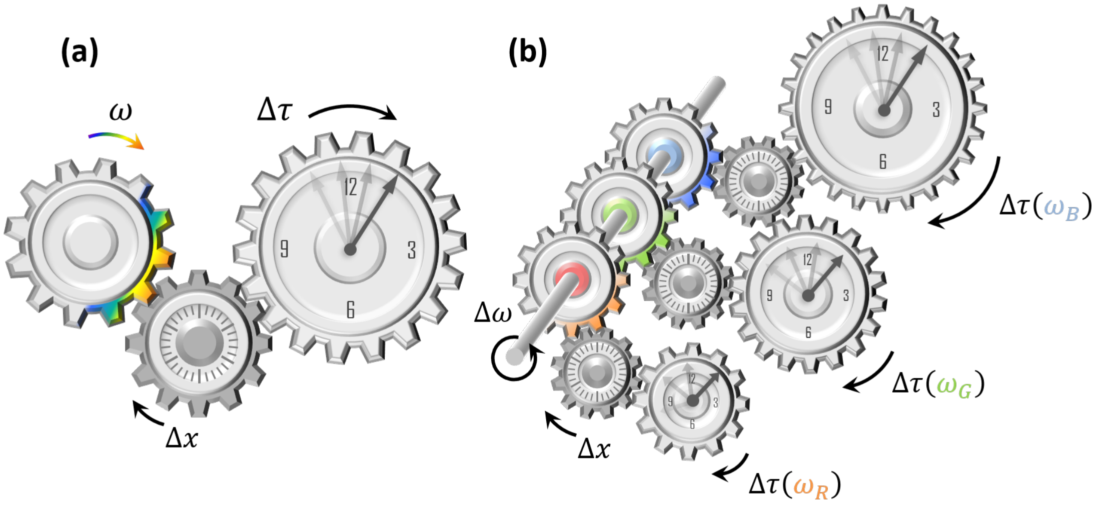

Figure 3.1: Illustration of the "temporal gearbox" concept. Photonic time stretch is a real-time optical transformation in which the spectrum of an optical signal is mapped into time. The broadband optical pulse can first transform into alternate domains (e.g. spatial domain) before being mapped into time in the final stage. Transforming first into other domains is useful for imprinting information which exists in domains other than time (e.g. spatial or angular data). (a) With conventional time stretch, the spectrum is mapped into time at a fixed rate, using a fixed dispersive element. This can be likened to using fixed gear to represent the mapping between domains. (b) In warped time stretch, the rate at which spectral information is mapped into time can be adjusted by modifying the dispersion profile. This can be likened to "shifting gears" in a mechanical gearbox to match the acceleration profile of a vehicle.

the group velocity dispersion of the dispersive fiber in a context-aware manner, such that the total time-bandwidth product of the system can be minimized [53]; recently, it has been shown that one can engineer the time-bandwidth product of data residing on an optical carrier, effectively achieving "photonic hardware acceleration" [32, 53]: it is not only possible to slow down the data but also to compress data all-optically [1, 32, 53, 54]. This is achieved using warped time stretch implemented with nonlinear group delay dispersion. The device performs variable-rate Fourier domain sampling where the sampling rate self-adapts to the local information content of the signal [1, 32].

The warped time-stretch functions as an information gearbox that dynamically matches the rate of incoming information to the rate of the data acquisition and processing backend. The operation can be likened to mechanical gearboxes or the"transmission in vehicles. The sampling rate of the acquisition system can be thought of being the equivalent of the number of teeth per second delivering torque at a certain point on a particular gear, which in turn is related to the rotation speed and the size of the gear used. The warped sampling is achieved by non-uniform mapping of the spectrum into time, such that information rich portions of the spectrum (high local entropy) are stretched more and receive larger number of samples by the ADC than do the sparse regions (low local entropy) [32]. This is done while minimizing the total temporal length (total number of samples), hence compressing the amount of digital data produced. The selection of gear ratio to match the acceleration profile of the vehicle is equivalent to the selection of dispersion profiles based on local sparsity of the optical spectrum. While the spectrotemporal reshaping performed by the warped dispersion is, in principle, lossless, signal reconstruction is lossy as it is subject to the finite signal to noise ratio of the system [54].

3.2 Equivalence to time-domain chirp

In Chapter 2, we derived an analytical expression for time-stretching using dispersive elements with arbitrary frequency dependence. In practice, the dispersive elements are often designed in terms of its Taylor expansion, where the series coefficients of the group delay correspond to higher order dispersion. That is, for a given group delay $\tau(\omega)$, we have:

$$\tau(\omega) = \sum_{m=1}^{\infty} \tau_m(\omega) = \sum_{m=1}^{\infty} \frac{\tau^{(m)}}{(m-1)!}(\omega - \omega_c)^{m-1} \tag{3.1}$$

where τ_m is the m-th group delay mode, and $\tau^{(m)} = \left.\frac{d^{m-1}\tau(\omega)}{d\omega^{m-1}}\right|_{\omega=\omega_c}$ is the m-th order derivative of the group delay evaluated at the centre frequency ω_c, and has units of $\left[\frac{\text{ps}}{\text{Hz}^{m-1}}\right]$. Each component of the group delay inputs a different spectrotemporal characteristic to the optical signal intensity. For example, in a fiber of length L with constant group delay dispersion, $\tau^{(1)} = \beta_1 L$ is the pulse temporal delay, and the constant $\tau^{(2)} = \left.\frac{d\tau(\omega)}{d\omega}\right|_{\omega=\omega_c}$ is the traditional definition of the group delay dispersion $\beta_2 L$. The dispersive element thus functions as a temporal gearbox, matching the time-bandwidth product of the input signal to that of the digitizer and subsequent electronics. With highly dispersive elements, the optical spectrum is mapped the into the temporal domain in a process known as time-stretch dispersive Fourier transformation, which mathematically is described by the stationary phase approximation [28, 33, 34].

To complete the analogy with mechanical gearboxes, we now introduce a method to describe the same frequency-to-time mapping from the perspective of time-domain filtering, by developing a mathematical description of such a temporal chirp $\Omega(t)$ in terms of the Taylor dispersive element (with group delay $\tau(\omega)$ in the spectral domain. This allows us to adapt the sampling rate to match the local bandwidth of the input optical waveform directly in the time-domain. Under the aforementioned stationary phase approximation at $\omega = \omega_s$, each time point t

has a one-to-one correspondence to an optical frequency ω_s in the optical spectral envelope:

$$\tau^{-1}(t) = \omega_s - \omega_c = \sum_{m=1}^{\infty} \frac{\Omega^{(m)}}{(m-1)!} \left(t - \tau^{(1)}\right)^{m-1} \tag{3.2}$$

where $\tau^{-1}(t) = \Omega(t)$ is the inverse function of the group delay and $\left\{\Omega^{(m)}\right\}$ are the series expansion coefficients of the chirp.

Assume that the input signal has a spectrum $\tilde{E}_{in}(\omega)$ has a spectral phase $\theta(\omega - \omega_c)$; then after time-stretch dispersive Fourier transformation, in which each time point is now one-to-one mapped to a stationary frequency $t = \tau(\omega_s)$, the output signal $E_{out}(t) = |E_{out}(t)| \exp j\Phi(t)$ has a chirp $\Phi(t)$:

$$\Phi(t) = \theta(\omega_s - \omega_c) + \sum_{m=1}^{\infty} \frac{(m-1)\Omega^{(m)}}{m!} \left(t - \tau^{(1)}\right)^{m} \tag{3.3}$$

where the first term of the right hand side is the frequency-to-time mapped input phase, and the second term corresponds to the added dispersion, which we will use as our "temporal gearbox".

Using series reversion [55], the chirp coefficients $\left\{\Omega^{(m)}\right\}$ [11] can be described in terms of group delay coefficients $\left\{\tau^{(m)}\right\}$ as:

$$\begin{cases} \Omega^{(1)} \equiv \omega_c = \dfrac{1}{\tau^{(2)}} \\ \Omega^{(2)} = -\dfrac{\tau^{(3)}}{(\tau^{(2)})^3} \\ \Omega^{(3)} = \dfrac{3(\tau^{(3)})^2 - \tau^{(2)}\tau^{(4)}}{6(\tau^{(2)})^5} \\ \quad \dots \end{cases} \tag{3.4}$$

The output optical intensity of the signal after passing through a single dispersive element can then be rewritten in terms of the temporal chirp as:

$$|E_{D1}(t)|^2 \approx \frac{\left|\tilde{E}_i\left(\tau^{-1}(t)\right)\right|^2}{2\pi} \frac{d\tau^{-1}(t)}{dt} \tag{3.5}$$

With a finite set of group delay modes, we are thus able to design and generate any tailored gear ratios to adjust the incoming local (instantaneous) information rate. Since the acquisition system “shifts gear” (redistributes the local entropy) automatically, the temporal gearbox is the optical equivalent of a mechanical gearbox in an automatic transmission.

3.3 Conclusion

The temporal gearbox is a powerful methodology providing a solution to real-time analog-to-digital conversion of fast optical waveforms while minimizing the amount of data produced by these high throughput systems. outlines a pathway to real-time, single-shot optical computing and signal processing. Moreover, due to the symmetry between Equations (3.1) and (3.5), dispersion profiles that have a slow rate of convergence in one domain can be thus efficiently represented in its dual domain. The established equivalence in time and frequency domain descriptions of the frequency-to-time mapping has applications for the design and modelling of dispersive elements with discrete basis elements, such as the higher-order dispersion in the frequency domain, or the grating period of a chirped fiber Bragg grating in the time domain. Much like transmission system in vehicles, we envision the use of dispersive primitives to construct the desired group delay profile by its modal components to play an essential role in spectrotemporal reshaping and encoding of pulse trains in fiber-optic telecommunication systems.

CHAPTER 4

Reconstruction performance of time-bandwidth engineered systems

4.1 Introduction

In time-stretch systems, it is often useful to recover the time-domain signal from the acquired spectral intensity. This is achieved via backpropagation of the broadband signal envelope, and this requires the knowledge of the spectral chirp. The methods from which the spectral chirp is recovered are often collectively called phase retrieval, since photodetection is a square-law detector and only acquires the signal intensity. Since square-law detection is a nonlinear process, all methods require the acquisition of two or more intensity measurements to recover the signal phase (or equivalently, the spectral chirp).

In this chapter, we discuss the signal reconstruction process involving complex field recovery and back-propagation in the presence of noise. Given a method for phase retrieval, it is useful to evaluate the overall effect on signal fidelity of adding a time-stretch component to a coherent detection system. We show that the presence of noise and distortion to the acquired signal intensities significantly affects the convergence of the phase retrieval system. While the particular amount of noise tolerance depends on the retrieval method and sometimes the signal statistics itself, each method can be assigned an output signal to noise and distortion ratio (SNDR), or equivalently, an output effective number of bits (ENOB) as a threshold, under which the method breaks down and no longer functions properly.

This helps provide justifiication in assuming a perfect photodetection system in the Chapter 5; as long as one can limit the noise and distortion introduced into the system to that below the threshold, the signal can be reconstructed.

4.2 Methods

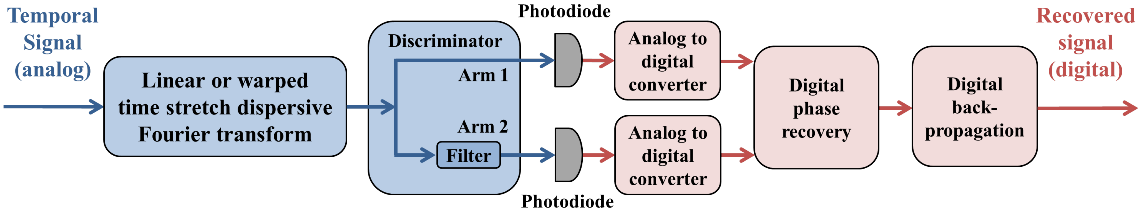

Figure 4.1: Block diagram of time stretch system with phase retrieval. The analog waveform is first reshaped by the linear or warped transform. An analog discrimination filtered response as well as the original frequency-to-time mapped signal intensities are then recorded for digital phase recovery. After photodetection and analog to digital conversion, the complex electric field is obtained using a digital phase recovery algorithm and the input waveform is reconstructed using digital back-propagation.

Figure 4.1 shows the block diagram of the system investigated here. The encoding uses a warped time-stretch dispersive Fourier transform with an engineered group delay, followed by intensity detection in the photodiode. The aim is to compress the intensity time bandwidth product to make digitization and storage of wideband optical waveforms possible in real-time and at high throughput. In the far field, the transform causes warped (nonlinear) frequency-to-time mapping. The decoding reconstructs the original waveform in the digital domain using complex field recovery followed by digital back-propagation through the warped group delay transform.

There are numerous techniques for recovering the complex amplitude from intensity-only measurements [39–47,56] and a review of the field is not the purpose of this paper. Here we use the STARS algorithm [40] without having performed a comprehensive comparison with alternative techniques. While this technique may not be the optimum, the conclusions reached here are independent of the specific phase recovery techniques and apply, qualitatively, to other methods. The STARS technique obtains the complex-field using two intensity measurements [40]. In particular, the signal is measured at the input and output of a linear optical discrimination filter, as shown in Figure 4.1.

4.3 SNR dependence of reconstruction

Reconstructing the temporal profile of the input waveform requires the full field of the dispersed signal and necessitates optical phase recovery. The ability to recover the optical phase from intensity measurements is influenced by the SNR of the measurement. Achieving phase recovery with large dynamic ranges is hindered by sources of the noise in the measurement, such as shot-noise and thermal noise of photo-detection, as well as quantization noise given the bit depth of the digitizer. This issue is not unique to the present system and is true for all phase recovery techniques. The main sources of noise in high-speed measurements are thermal noise, shot noise, relative intensity noise, and the quantization noise of the digitizer [57]. The ADC plays a central role in the system and its resolution and sampling rate (lower-bounded by the Nyquist rate) both affect the fidelity of the phase recovery and hence the reconstruction. The trade-off between ADC sampling rate and resolution places additional emphasis on the ADC.

To focus the discussion and give a specific example, we consider a test waveform shown in Figure 4.2(a). The signal under test is chosen such that (i) it is physically realizable, (ii) it has a reasonable order of complexity to demonstrate

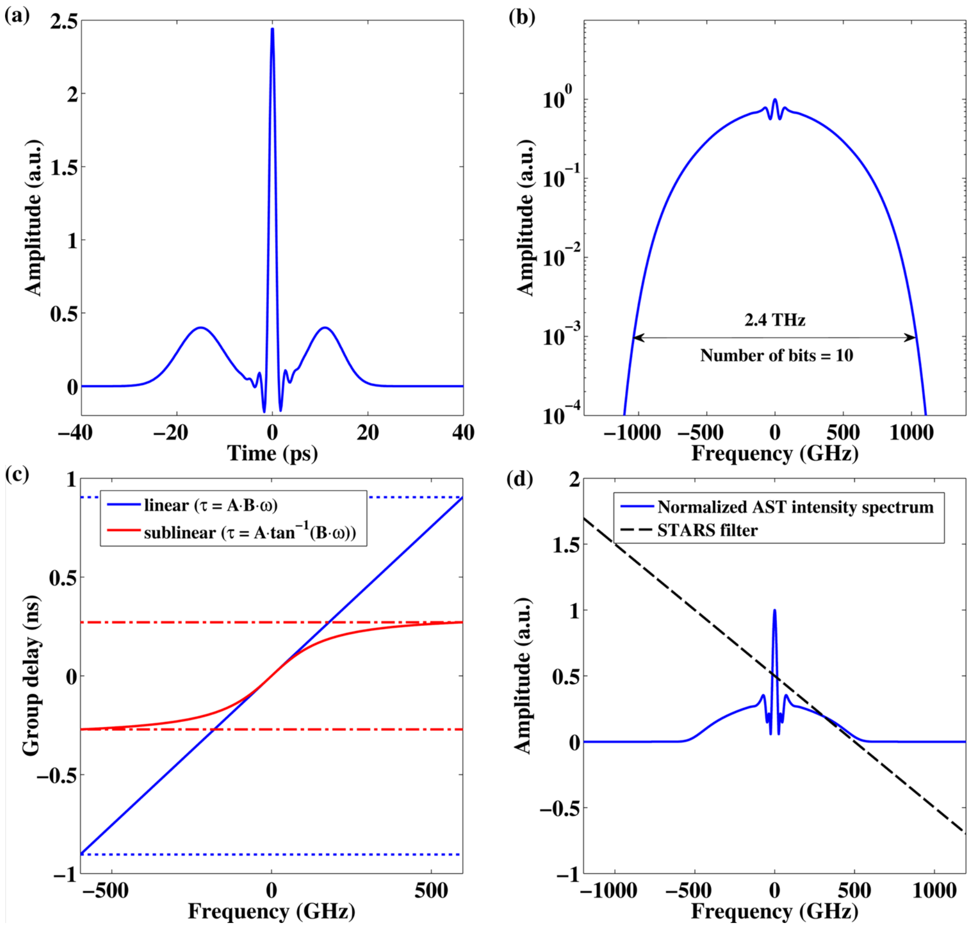

Figure 4.2: (a) Signal under test. (b) Intensity spectrum with 2.4 THz double sideband bandwidth. (c) Group delay dispersion profiles $\beta(\omega)$ for warped ($\beta(\omega) = A \cdot \tan^{-1}(B\omega)$, where $A = 200\,\text{ps}$, $B = 1.2\,\text{ps}$) and linear ($\beta(\omega) = A \cdot B\omega$, $A \cdot B = 240\,\text{ps}^2$) stretches. Here, A is related to the dispersion strength and parameter B is related to the degree of warping. The ratio of the dash-dot and dotted lines correspond to the designed time-bandwidth compression, and are referenced in Figures 4.3(e) and 4.3(f). (d) Discrimination (STARS) filter amplitude, with the output intensity spectrum of the linear case as comparison.

that interference between pulses after dispersion does not nullify the compression, and (iii) it contains sufficient spectral sparsity and temporal diversity (having both long and short pulses). The simulations include thermal noise and ADC quantization noise (measured as bits). We assume a moderately high average pulse power such that the shot noise-limited SNR is negligible relative to quantization noise-limited SNR, yet low enough to avoid nonlinear effects.

Figures 4.2(a) and 4.2(b) show the temporal profile and the spectrum of input signal under test. The input intensity single sideband bandwidth is roughly 1.2 THz (measured at the -30 dB point). We also assume a digitizer bandwidth of 32 GHz and compare the linear stretch (TS-DFT) with the warped stretch. Figure 4.2(c) shows the group delay dispersion profiles used in each case and the legend shows their mathematical description. Figure 4.2(d) shows the transfer function of the optical discrimination filter employed for phase recovery (see Figure 4.1) overlapped with the output signal spectrum.

The fidelity of the encoding process depends on the sparsity/redundancy of the input signal, while the decoding accuracy is influenced by the digital phase recovery and back-propagation algorithms and their tolerance to SNR. The amount of group delay dispersion used is dictated by the need to compress the main portion of the signal spectrum to the bandwidth of the analog-to-digital converter (ADC). The latter is the target bandwidth for time-bandwidth compression systems. In the case of time-bandwidth engineering, the warped shape of the group delay is further dictated by the desired output temporal duration. In other words, the kernel of the transform is designed based on the input signal bandwidth and duration, the target output (digitizer) bandwidth, and the desired output time duration. As previously demonstrated [1], the information about the input signal bandwidth and spectral resolution as well as the desired output intensity bandwidth and the effective number of bits of the ADC are used to design the GD profile.

To achieve intensity time-bandwidth compression, the warped case uses a warped GD with sublinear frequency dependence. The strength of the dispersion (A) and warping (B) are calculated based on the expected range of signal durations and the statistics of the spectral sparsity. It is noted that if the center wavelength of the input signal drifts from its nominal value, the relative high and low frequencies change with respect to the center frequency of the dispersive element. Consequently, the frequency-to-time mapping shifts to different spectral features, which in general decreases the maximum compression ratio.

The stretched modulation distribution [53] is a time-frequency distribution that visualizes the chirp caused by the linear and the warped GD. It plots the envelope intensity as a function of modulation frequency and the group delay. Figures 4.3(a),(b) show the SM plots for the warped and linear transformed signals. The bandwidth of the central lobe in the spectrum is given by the intercept of the distribution with the horizontal axis and is determined by the slope of the GD dispersion near the origin.

In both cases, the GD dispersion slope is designed to reduce the central lobe bandwidth to the target bandwidth of 32 GHz. The target bandwidth is the ADC bandwidth and to model it a 32 GHz low pass filter is applied to the stretched signal before the quantization. This limits the signal bandwidth that is used for reconstruction to the designed (ADC) bandwidth.

Figure 4.3(c) show the RF (intensity) spectra for both cases (linear and warped) before and after application of the 32 GHz anti-aliasing RF filter. We note that although the spectrum of the warped stretched waveform extends beyond the central lobe, the reconstruction only uses the portion of the spectrum within the compressed target (ADC) bandwidth. Also, the same bandwidth is used for reconstruction in both the linear and the warped stretched signals. Figure 4.3(d) shows the same for stretched output in Arm 2, i.e. after the discrimination filter (Figure 4.1). The analog temporal signals, after the stretch transformation and application of the RF filter, are shown in Figures 4.3(e) (Arm 1) and 4.3(f) (Arm 2). While the intensity bandwidth in both cases is compressed to 32 GHz, the temporal record length (sum of two arms) is reduced by 2.75 times for the warped

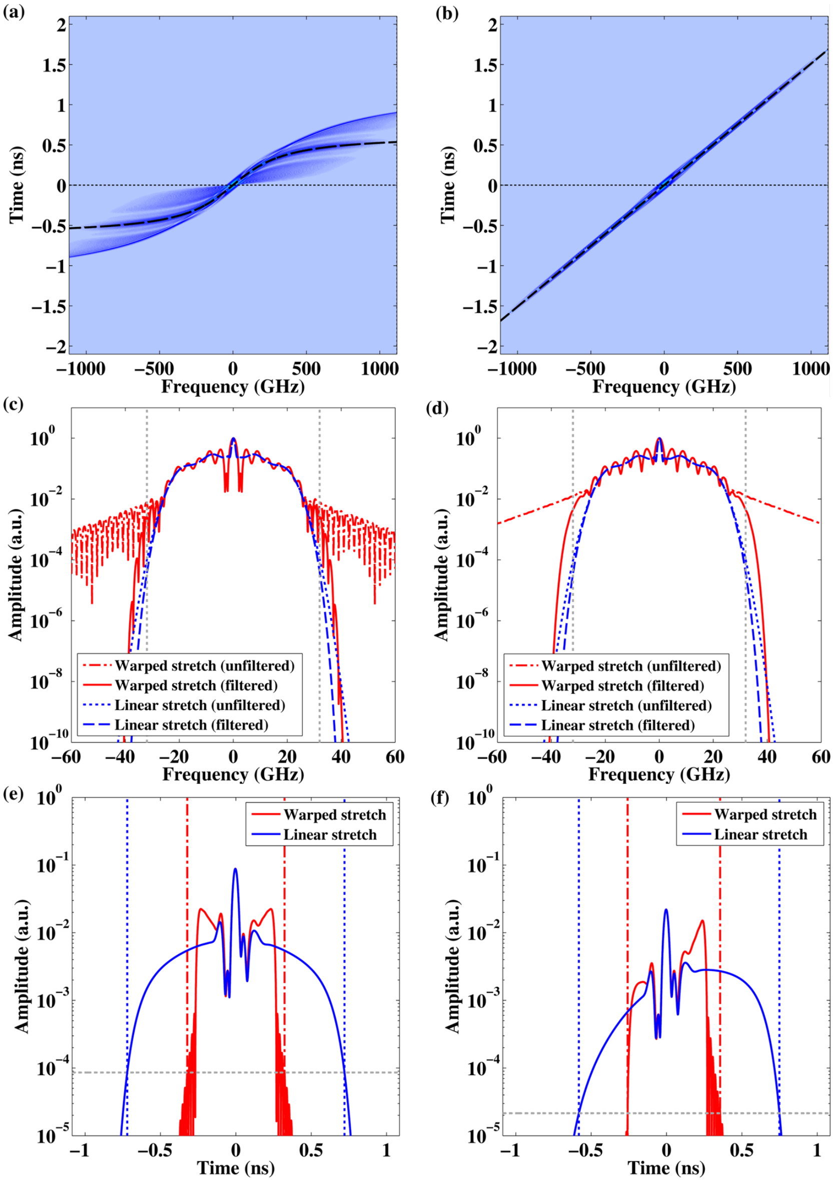

Figure 4.3: The stretched modulation distribution for the case of (a) warped stretch (b) linear stretch. (c) The RF spectrum of Arm 1 (see Figure 4.1) before and after application of the 32 GHz RF filter. (d) The same for Arm 2. The corresponding output time domain signals after the photodiode is shown (e) without and (f) with the discrimination filter; the filter is used for phase recovery. The horizontal dotted line is the digitizer least significant bit (LSB) and defines the effective temporal duration, as shown by the vertical dotted lines. Note how 4.3(f) differs from the ideal time duration as defined by the group delay in Figure 4.2(a), due to limitations in resolution (i.e. the number of bits).

stretch leading to the time-bandwidth compression by the same factor.

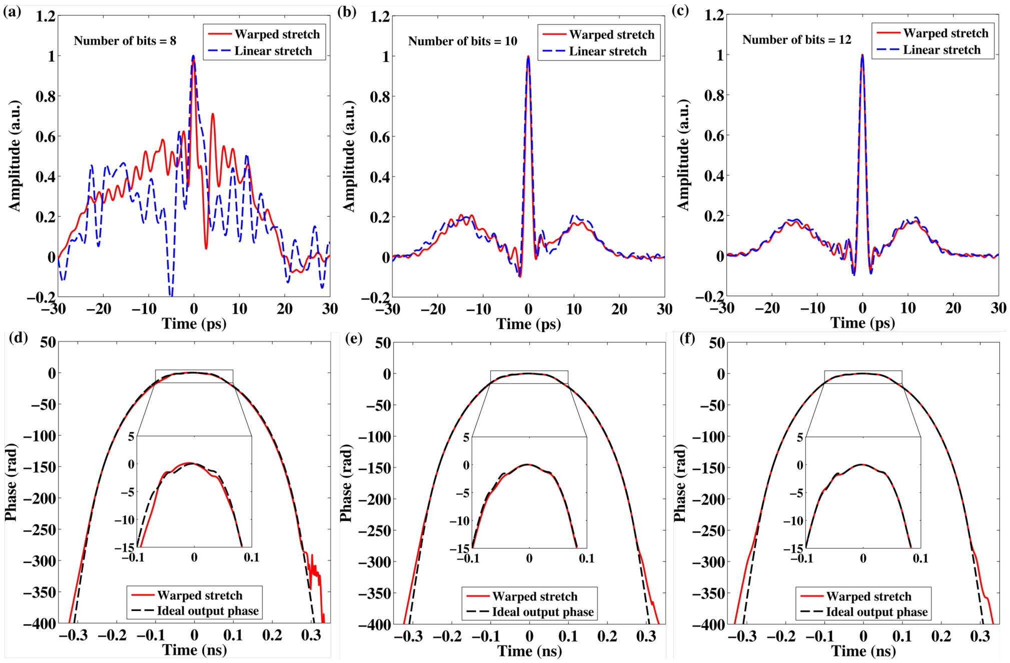

Figure 4.4: Reconstructed input signal after digital phase recovery and back-propagation for both linear and warped stretch cases. Digitizers with (a) 8 bits, (b) 10 bits and (c) 12 bits were simulated, each with their corresponding reconstructed phase plots (d-f). The number of bits affects the SNR of amplitude measurements (Arm1 and Arm2 in Figure 4.1) from which the phase is recovered which then affects the reconstruction accuracy. Results are for single shot, i.e. no averaging has been used.

The input temporal waveform is reconstructed through digital back-propagation using the measured amplitude and the recovered phase. Figure 4.4 shows the reconstructed temporal waveform for the linear and warped stretch cases for different number of bits. The plots are for single shot capture and reconstruction (no averaging has been employed). The accuracy of digital reconstruction depends on the SNR of the digitized signals. This is not unique to the warped stretch system and is also true for the linear stretch (TS-DFT). Playing a dominant role in the SNR, the ADC quantization noise depends on the resolution of the ADC and is reflected in the number of bits of the digitizer. The reconstruction accuracy is similar for both linear and warped cases and is limited by the phase recovery and reconstruction accuracy. Figure 4.4 demonstrates that as the number of bits increases, the reconstruction accuracy improves. We note that without stretching (whether linear or warped), the 1.2 THz bandwidth input waveform would have been too fast to be digitized in real-time by any digitizer.

Finally, we point out that the degree to which digital phase recovery is influenced by the SNR depends on the specific recovery algorithm. The present results are for one particular recovery algorithm described above. The concept of data compression based on the warped stretch transform is not dependent on a particular phase recovery algorithm. There are many well-established phase recovery techniques that aim to extract the phase information from intensity-only measurements (such as that from a photodetector) [13,39–47]. While the mechanisms for different phase recovery techniques may vary (and indeed is a respectable field of research in itself), their effect on the SNR can ultimately be quantified using the same methodology described here.

4.4 Conclusion

Linear and warped stretch transforms are useful for capture of wideband intensity modulated optical waveforms, such as for real-time instruments where high speed signals must be digitized in real-time. Compressing the intensity time-bandwidth product using warped group delay dispersion enables real-time digitization of an ultrafast signal and at the same time reduces the record length. Digital reconstruction of the original signal requires optical phase recovery in both the linear and warped stretch cases and its accuracy depends on the SNR. For wideband systems, the SNR is typically limited by the resolution of the ADC [57]. By way of example, we have simulated waveform reconstruction for the cases of linear and warped stretches, where the warped case achieves a time-bandwidth compression of 2.75 times when compared to the linear case.

CHAPTER 5

Time-bandwidth product engineering with warped time stretch

5.1 Introduction

With the quantity of data growing exponentially, new approaches to data capture and compression are urgently needed. With respect to the field of optics, this predicament arises in fiber optic communication and in real-time optical instruments [58]. Such instruments are used in study of optical rogue waves [59–62], in ultrafast signal measurement [37,63–68] , and ultrafast imaging [16,69,70]. Owing to their high measurement rate, real-time instruments produce a fire hose volume of data that overwhelms even the most advanced computers [71]. This necessitates innovations in data management and inline processing techniques. Time–bandwidth compression can alleviate this problem.

The generation of waveforms with wide instantaneous bandwidth can be a bottleneck in radar, communication systems, and laboratory instruments. To this end, photonic arbitrary waveform generation that employs spectrum to time mapping has been proposed as a potential solution [72–74]. These systems are limited by the time bandwidth of the component used for spectrum encoding. Time–bandwidth expansion may improve the performance in these applications.

In this work, we present foundations of methods to manipulate the time bandwidth of optical signals using photonic platforms. We employ the stretch modulation (S_m) distribution to design time–bandwidth engineering (TBE) systems in both near-field and far-field regimes. Using the S_m distribution we derive, for the first time to the best of our knowledge, the equations governing the time-bandwidth product identify an important criterion on the maximum curvature of warped group delay (GD) that must be met in order to achieve time–bandwidth compression. This criterion is then used to compare various GD profiles as it relates to their utility for engineering the time-bandwidth product.

To analyze the time-bandwidth product (TBP), we introduce a time-frequency distribution, called the stretched modulation distribution, to visualize the time duration and intensity bandwidth of the input signal. We also develop mathematical equations to show the influence of chromatic dispersion on the overall time-bandwidth product of the optical input.

5.2 Time frequency analysis

The stretch modulation distribution is a time-frequency distribution as a shifted variation of the ambiguity function in the freqeuency domain, as follows:

$$S_m(\omega_m, t) = \int_{-\infty}^{\infty} \tilde{E}_{in}(\omega)\tilde{E}_{in}^*(\omega + \omega_m)\tilde{H}(\omega)\tilde{H}^*(\omega + \omega_m)e^{j\omega t}d\omega \tag{5.1}$$

where t, ω and ω are the time, optical frequency and envelope frequency variables, $\tilde{E_i}n(\omega)$ is the complex input field spectrum, and $H(\omega) = \exp j\phi(\omega)$ is the (lossless) dispersion kernel representing the photonic operation performed on the input signal. Physically speaking, the distribution can be interpreted as the cross correlation of the dispersed input system after simultaneously undergoing a time shift of t. It allows us to plot the time duration and the intensity bandwidth of the input signal simultaneously:

The stretched modulation (S_m) distribution provides a tool to design TBE systems through proper choice of the operation kernel. The top and bottom plots in Figure 5.1 are schematics showing the S_m distribution of the input (top plot) and output (bottom plot) in an optical system where the kernel describes a filter

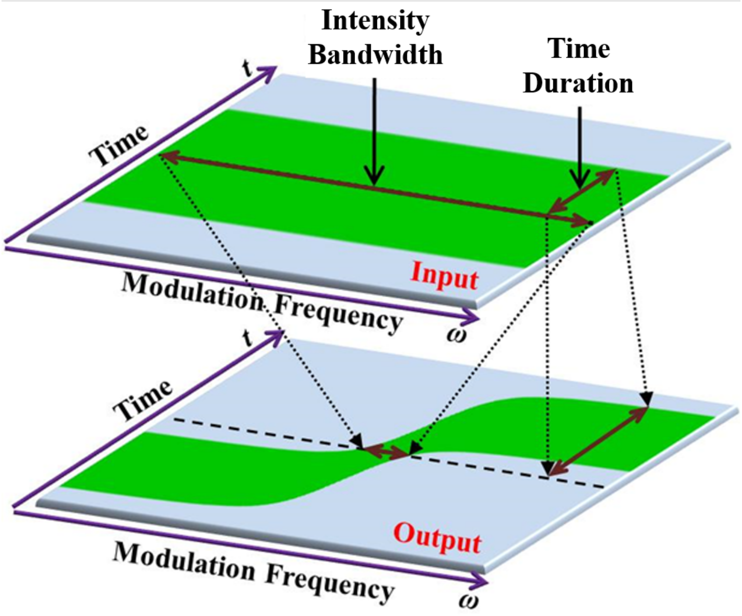

Figure 5.1: The stretch modulation distribution is a time-frequency plot for designing and benchmarking optical TBE systems, graphically displaying the time duration and intensity bandwidth of the optical intensity of an optical pulsed signal simultaneously, while under the influence of chromatic dispersion. The top and bottom plots are qualitative and show the magnitude of the S_m distribution of the input and output signals in a system with a sublinear group delay profile. The S_m distribution shows how the TBP of the signal intensity can be engineered.

with sublinear phase derivative (group delay) $\tau_g = \frac{\mathrm{d}\phi}{\mathrm{d}\omega}$. Such a system compresses the TBP of the information envelope [75, 76].

To show how the distribution can be used to design and analyze TBE systems, we will consider systems in which operation kernel represents a phase filter with different group delay profiles. In practice the filter operation can be implemented with a dispersive optical element with tunable group delay profile. After dispersion, the signal can be in the far field or near field regime, depending on whether the stationary phase approximation is satisfied or not. The far field is achieved for a large amount of group delay dispersion and/or when the signal has a very large bandwidth leading to one-to-one mapping of frequency into time. Conversely, the near field refers to the regime prior to the stationary phase approximation being satisfied. We note that in the far-field there is warped (nonlinear or non-uniform) frequency-to-time mapping (i.e. warped stretch transform), whereas in the near field there is no one-to-one mapping. Therefore near-field case, on its own, is not a Fourier transform or frequency-time mapping for arbitrary signals. We consider three types of group delay profiles, namely, linear, sub-linear and super-linear. These group delay profiles are compared in Figure 5.2(c). Here the sub-linear and super-linear profiles are defined as functions that grow slower or faster than a linear function when its argument becomes very large.

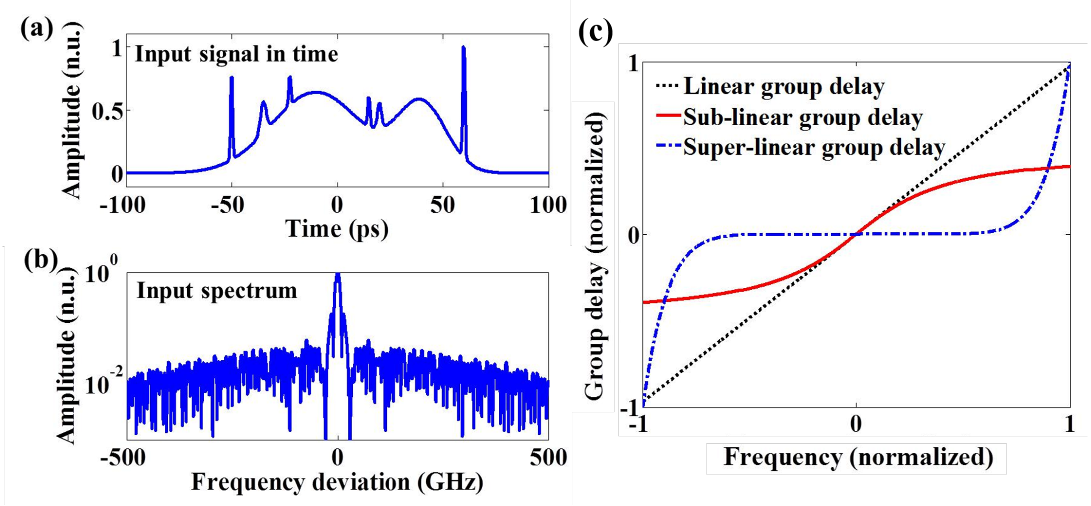

Figure 5.2: Arbitrary input signal in (a) time and (b) spectral domains used in this paper. (c) Three different qualitative GD profiles that can be used to engineer the TBP of optical signals. S_m distribution plots corresponding to these profiles are shown in Figure 5.3.

The input used for the S_m distribution, as shown in Figure 5.2(a) and (b), was designed to have a collection of different temporal features such as coarse and fine temporal features with different durations. It also includes both closely spaced as well as sparsely spaced features. We take this complex input to be transform-limited, although most inout chirp is negligible relative to the dispersion we use in time-stretch systems. The temporal duration and the bandwidth here are defined as being 30 dB from the peak value. Figure 5.3 compares the S_m distribution plots of the output in the near field and the far field regimes when the operation kernel has the normalized group delay profiles shown in Figure 5.2(c).

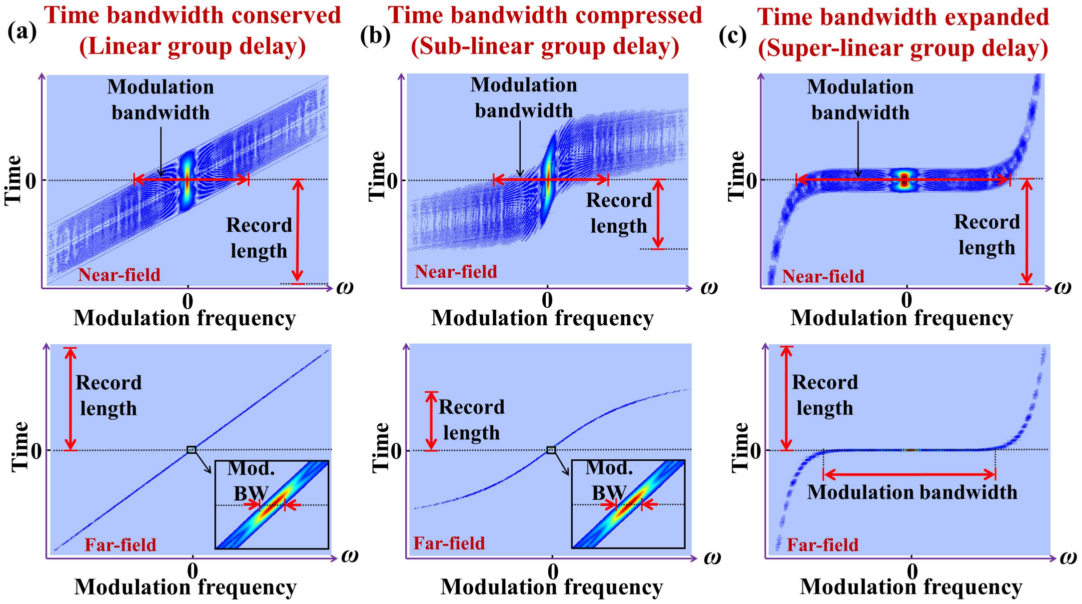

Figure 5.3: The stretched modulation (S_m) distribution is used to design time-bandwidth engineering systems with engineered time bandwidth product (TBP). At time $t = 0$ (horizontal axis), it represents the modulation bandwidth. The half-extent along the vertical direction is the record length. Here we have compared the distribution for three cases: time-bandwidth (a) conserved, (b) compressed and (c) expanded. In each case we have shown operation in the near field and far-field. The group delay profiles corresponding to each case is shown in Figure 5.2(c).

As shown in Figure 5.3(a), when the group delay has a linear profile, the distribution is linearly tilted, resulting in a reduced modulation bandwidth. However, record length is proportionally increased. In this case the time bandwidth product is either conserved (in far-field regime) or expanded (when in the very near-field regime).

However, if we introduce a spectrally-tailored dispersion profile, having the shape shown in Figure 5.3(b), corresponding to sub-linear group delay profile shown in Figure 5.2(c), the bandwidth is reduced but the record length is not increased proportionally. In this case, one achieves time bandwidth product compression in both near field and far field regimes. Finally, if the distribution is warped in the manner shown in Figure 5.3(c), corresponding to super-linear group delay profile shown in Figure 5.2, the time-bandwidth product is expanded in both near field and far field regimes.

5.3 Methods

We now define the record length (ΔT) and intensity bandwidth (ΔB) expressions using the S_m distribution. Assuming near-even parity for the phase profiles $\phi(\omega + \frac{\omega_m}{2})$ and $\phi(\omega - \frac{\omega_m}{2})$, we perform a Taylor series expansion near $t = 0$ and arrive at the following approximation:

$$\phi\left(\omega + \frac{\omega_m}{2}\right) - \phi\left(\omega - \frac{\omega_m}{2}\right) \approx 2\omega\tau_g\left(\frac{\omega_m}{2}\right) \tag{5.2}$$

This approximation assumes that the group delay profile is sufficiently smooth (i.e. $\left|\tau_g^{`\prime}\left(\frac{\omega_m}{2}\right)\right| \ll \frac{6}{\Delta\omega^2}\left|\tau_g\left(\frac{\omega_m}{2}\right)\right|$), where $\Delta\omega_{in}$ is the input optical bandwidth. Given this approximation, we thus have:

$$S_m\left(\omega_m, t + 2\tau_g\left(\frac{\omega_m}{2}\right)\right) = \int_{-\infty}^{\infty} \tilde{E}_{in}\left(\omega - \frac{\omega_m}{2}\right)\tilde{E}_{in}^{*}\left(\omega + \frac{\omega_m}{2}\right)e^{j\omega t}d\omega \tag{5.3}$$

Note that we do not have to assume far-field conditions to achieve this result. Consider each vertical (temporal) slice of the distribution as a cross correlation of the post-dispersion output signal spectrum $\tilde{E}_{out} = \tilde{E}_{in}(\omega) \cdot \tilde{H}(\omega)$ with its time-shifted waveform. Then, the maximum absolute amount of time variable t at which $S_m(\omega_m, t)$ has non-zero values is the duration of output signal ΔT_{out} (up to the least significant bit measurable by the digitizer). Graphically speaking, the record length of the output signal can be measured by the vertical (temporal) slice of the distribution, as the half-maximum span of the plot in S_m distribution in the temporal direction. By Equation (5.3), this is equal to:

$$\Delta T_{out} = \Delta T_{in} + 2\tau_g \left(\frac{\Delta B_{in}}{4} \right) \tag{5.4}$$

where ΔB_{in} is the intensity bandwidth of the input signal, and is half that of the optical bandwidth. Note that we have assumed that the group delay profile to be monotonic on average for this to be true (otherwise the half-maximum would occur elsewhere than $\omega_m = \frac{\Delta B_{in}}{4}$. In the far-field case, we can further simplify this expression to be $\Delta T_{out} \approx 2\tau_g \left(\frac{\Delta B_{in}}{4} \right)$.

To derive an analytical expression for the output intensity bandwidth ΔB_{out}, we begin with the intensity spectrum $\tilde{I}(\omega_m)$:

$$\tilde{I}(\omega_m) \triangleq \mathcal{F}\left\{ |E(t)|^2 \right\} = \int_{-\infty}^{\infty} \tilde{E}\left(\omega - \frac{\omega_m}{2} \right) \tilde{E}^*\left(\omega + \frac{\omega_m}{2} \right) d\omega \tag{5.5}$$

where in the second equality we have used the well-known fact from the Weiner-Khinchine therorem that the intensity spectrum is equal to the cross-correlation of the electrical field sprectum [75]. Using Equation (5.1), we can see that each horizontal slice of the S_m distribution can be interpreted to be time-shifted versions of the intensity spectrum of the post-dispersion pulse. The intensity bandwidth I can thus be measured from the S_m distribution from the horizontal slice at $t = 0$. Note that the intensity bandwidth is measured not at the 3 dB point, but at the "base" where the spectrum is limited by the bit depth of the digitizer or noise floor, whichever is limiting in this case. Evaluating the output intensity spectrum at the maximum modulation frequency $\omega_m = \frac{\Delta B_{out}}{2}$, we then have:

$$\tilde{I}_{out}\left(\frac{\Delta B_{out}}{2} \right) = \int_{-\infty}^{\infty} \tilde{E}_{in}\left(\omega - \frac{\Delta B_{out}}{4} \right) \tilde{E}_{in}^*\left(\omega + \frac{\Delta B_{out}}{4} \right) e^{-j\omega 2\tau_g (\frac{\Delta B_{out}}{4})} d\omega \tag{5.6}$$

In the far-field approximation, since $\Delta B_{in} \gg \frac{\Delta B_{out}}{4}$, we can further simplify this expression to be:

$$\begin{aligned}\tilde{I}_{out}\left(\frac{\Delta B_{out}}{2}\right) &\approx \int_{-\infty}^{\infty} \left|\tilde{E}_{in}(\omega)\right|^2 e^{-j\omega 2\tau_g\left(\frac{\Delta B_{out}}{4}\right)} d\omega \\ &= \mathcal{F}\left\{\left|\tilde{E}_{in}(\omega)\right|^2\right\}\Bigg|_{t=2\tau_g\left(\frac{\Delta B_{out}}{4}\right)} \\ &= \int_{-\infty}^{\infty} E_{in}(t)E_{in}^{*}\left(t+2\tau_g\left(\frac{\Delta B_{out}}{4}\right)\right) dt\end{aligned} \tag{5.7}$$

in which the last equality again uses the Weiner-Khinchine theorem. This last expression is an autocorrelation with a total duration of $2\Delta T_{in}$. However, since we substituted half the output intensity bandwidth for Equation (5.6), we equate the half-duration ΔT_{in} with the argument for E_{in}^{*}, and arrive at the expression for the output bandwidth as:

$$2\tau_g\left(\frac{\Delta B_{out}}{4}\right) = \Delta T_{in} \Longrightarrow \Delta B_{out} = 4\tau_g^{-1}\left(\frac{\Delta T_{in}}{2}\right) \tag{5.8}$$

In general, to account for very near-field group delay effects, in which the pulse lengthens but the change in bandwidth is negligible, we have our final bandwidth expression as:

$$\Delta B_{out} = \min\left\{B_{in},\, 4\tau_g^{-1}\left(\frac{\Delta T_{in}}{2}\right)\right\} \tag{5.9}$$

The above conclusion assumes that the signal is broadband, comprising both fast and slow features, i.e., high and low instantaneous frequencies with respect to the bandwidth of the GD. Such a signal has redundancy in the time domain, as shown in Figure 5.2. If the signal has only high frequencies, for example, then the effect of GD will be different than that described above. Also, as with any other data compression method, the maximum compression that can be achieved is signal dependent. In particular, it will depend on the amount of redundancy in the signal, a quantity that will be reflected in the probability distribution function of the signal instantaneous frequency.

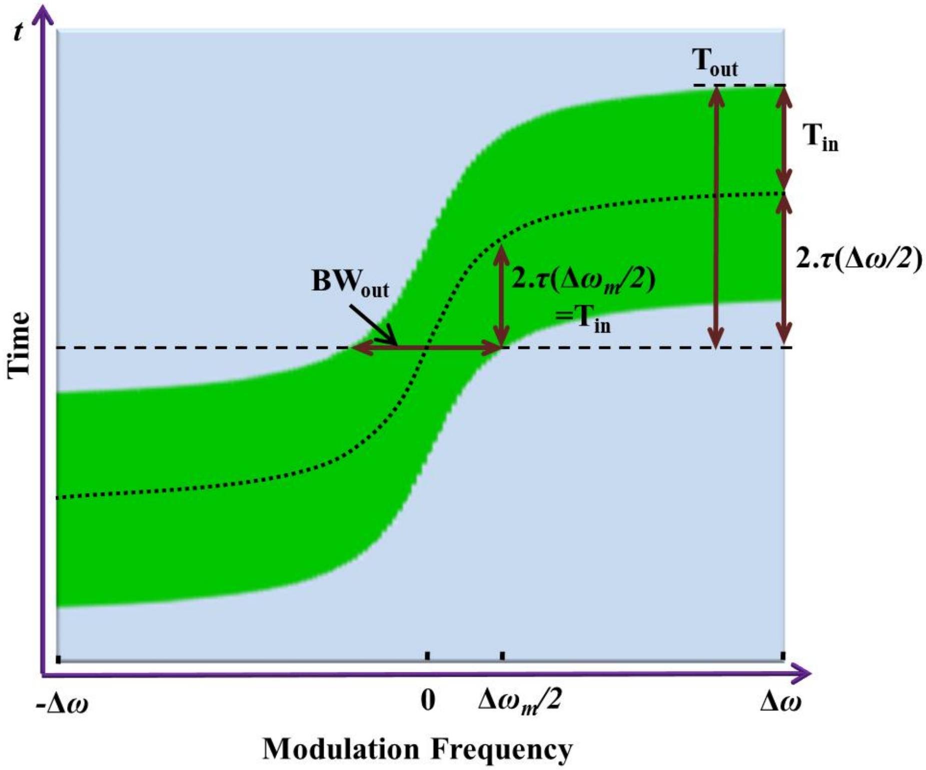

Figure 5.4: Graphical demonstration of the relation between the input signal and system parameters of the kernel to the output signal duration and modulation bandwidth, simultaneously, using the S_m distribution.

We have shown how the output signal duration is analytically completely dependent on the input signal and the kernel. This relation can also be graphically shown with the S_m distribution, as annotated in Figure 5.4.

5.4 Simulations

To examine the output TBP, we have compared the calculated value from Equations (5.4) and (5.9) to numerical simulations. The input optical signal is shown in the time and spectral domains in Figure 5.2. The input signal has duration of 200 ps and complex-field bandwidth of 1 THz. Duration and the bandwidth here are defined as the 1% value (from peak). We have considered three systems with different types of GD profiles, i.e., with linear, sub-linear, and super-linear GD profiles, as shown in Figure 5.5. The super-linear case has the same total GD as the linear case and the sub-linear case has the same slope as the linear case at the origin. The linear, sublinear and superlinear GD profiles of these functions are, respectively:

$$\begin{aligned}\tau_{lin}(\omega) &= A \cdot B \cdot \omega \\ \tau_{sub}(\omega) &= A \tan\left(\frac{B}{2} \cdot \omega\right) \\ \tau_{sup}(\omega) &= A \cdot \tan^{-1}\left(B \cdot \omega\right)\end{aligned} \tag{5.10}$$

where $A = k{\cdot}2.81\,\mathrm{ns}$ and $B = 0.22\,\mathrm{ns}$, and k is the dispersion strength factor. We have plotted the numerically calculated output TBP using Equations (5.4) and (5.9) in each case as a function of the k factor in Figure 5.5(b). Calculated TBP of the linear, superlinear, and sub-linear cases are shown with red solid, green dashed–dotted, and blue dashed lines, respectively. The TBP in each case is normalized to the input signal TBP. Small k factors correspond to the near-field regime and large k factors correspond to the far-field regime. We have also simulated the output signal in each case and calculated the output signal TBP and compared them to predictions by Equations (5.4) and (5.9) in Figure 5.5(b). Simulated output signal TBP for the linear, super-linear, and sub-linear cases are shown with red triangles, green circles, and blue squares, respectively. As seen from the simulation results, there is an excellent agreement with the output TBP equations given by Equations (5.4) and (5.9).

We can identify three regions of operation spanning the near- to far-field regimes. For the case of linear GD, an example of the S_m distribution in each region is shown in Figure 5.6. Region 1 ($k < 0.5$) corresponds to the case when $\Delta\omega_m = 2 \cdot \Delta\omega$. Since in this region the output bandwidth is fixed but the output duration is increased, the TBP is enlarged, as shown in Fig. 5.6(a). However, in Regions 2 and 3, the TBP gets close to unity as dispersion is increased (compare

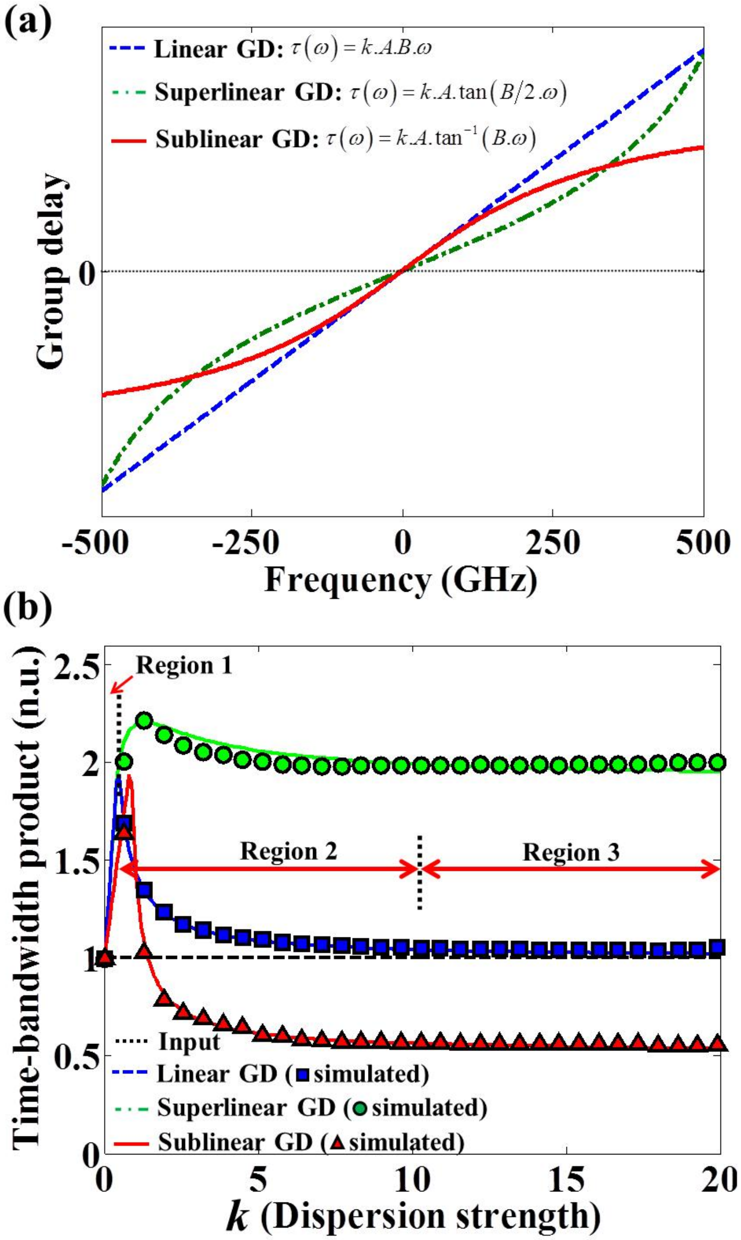

Figure 5.5: (a) Three different group delay profiles simulated to engineer the time bandwidth product. (b) Simulated output time bandwidth product (TBP) as a function of dispersion strength, k, compared to the calculated TBP using Equations (5.4) and (5.9). The three near-, mid-, and far-field regions defined here correspond to the same regions shown in Figure 5.6.

Figures 5.5(b), 5.6(b), and 5.6(c)).

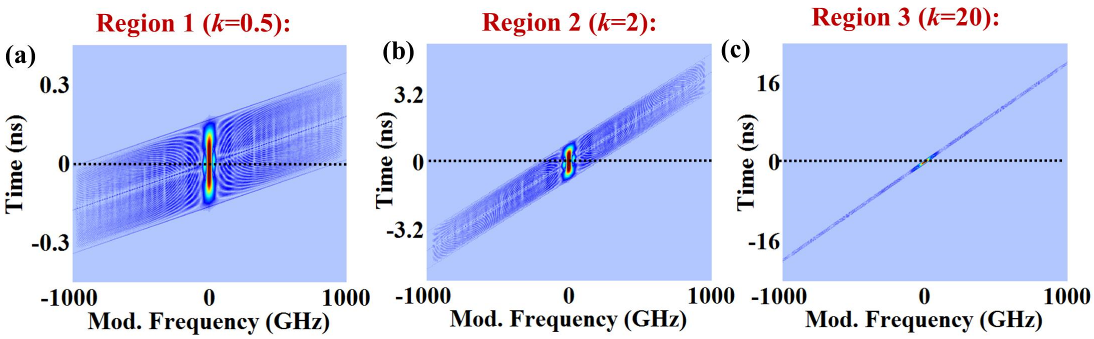

Figure 5.6: An example of the effect of varying k on the S_m distribution in the near, mid, and far-field regions, for the case of the linear GD profile.

5.5 Distortion Analysis for Group Delay Nonidealities

The desired phase kernel profile for TBE can be obtained using a chirped fiber Bragg grating (CFBG). A CFBG offers great flexibility in dispersion profile and has low insertion loss, but exhibit GD ripples, which are problematic. There are demonstrated techniques for mitigating the effect of ripples that can be employed in our technique to calibrate the GD ripples in post-processing analysis [67,68,77]. We note that the transformed signal has both phase and amplitude requiring complex field recovery before reconstruction in the digital domain [54, 75, 76]. The S_m distribution can also be used to assess the impact of nonidealities in the performance of TBE. In a dispersive TBE system, nonidealities include GD ripples, polarization dependence, and temperature fluctuations. The distribution can be used to visualize the effect of nonidealities on the modulation bandwidth and record length and provides insight into how to mitigate them.

In the examples studied here, we consider four systems with GD profiles shown in Figure 5.7. We consider operation in the far field (Figures 5.7(a),(b)) as well as the near field (Figures 5.7(c),(d)). In each regime we consider two cases: GD

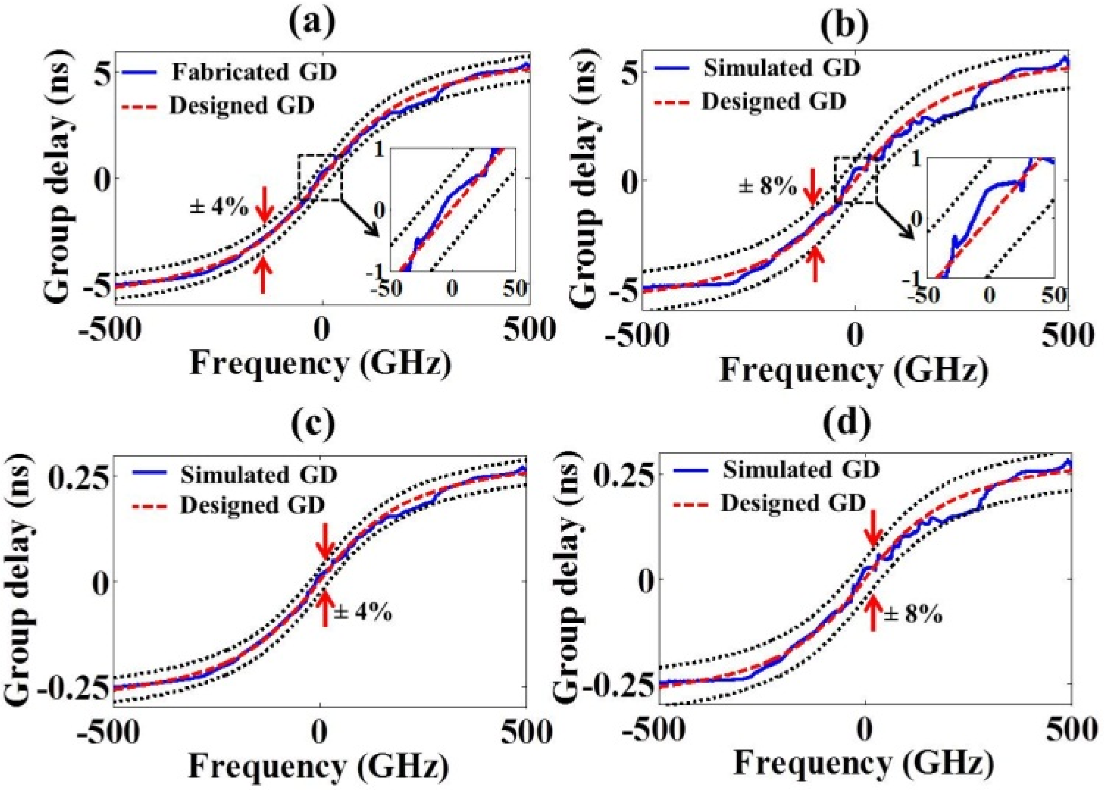

Figure 5.7: Four different GD profiles used to study the effect of GD ripples on the performance of TBE systems. We consider operation in (a,b) the far field as well as (c,d) the near field. In each regime we consider two cases: GD ripples of less than 4% and 8% of the maximum GD. S_m distribution plots corresponding to these profiles are shown in Figures 5.8 and 5.9.

ripples of less than 4% and 8% from the ideal GD.

The far-field GD profile with 4% ripples is the experimentally measured result for a fabricated grating that was recently used to demonstrate optical real-time data compression [76] (see Figure 5.7(a)). The grating was designed to compress the bandwidth of a signal with 1 THz bandwidth to 8 GHz so it can be digitized in real time, and at the same time to compress the record length and, hence, the digital data size. For the far-field example with 8% GD ripples (Figure 5.7(b)), GD profile is simulated, with the same profile but artificially twice the ripple amplitude. For the near-field examples, Figures 5.7(c) and (d), we have scaled down the measured profiles in Figures 5.7(a) and 5.7(b) each by 20 times. In these simulations, we continue to use the broadband input signal used in previous sections; the time domain and spectrum plots are shown in Figure 5.2.

Figure 5.8 shows the S_m distribution corresponding to the large GD profiles with 4% and 8% GD ripples. Since in both cases the system is operating in the far-field regime, the expected output duration is 10 ns, which is the total system GD. The S_m distribution shows that systems with 4% and 8% ripples have similar output durations (10 ns), suggesting that the effect of GD ripples on the output signal duration is limited. Due to the presence of the ripples, the even parity of the phase due to the dispersive elements is broken. Therefore, the approximation in Equation (5.2) no longer holds:

$$\phi\left(\omega+\frac{\omega_m}{2}\right)-\phi\left(\omega-\frac{\omega_m}{2}\right)\approx\omega\left(\tau_g\left(\frac{\omega_m}{2}\right)-\tau_g\left(-\frac{\omega_m}{2}\right)\right) \tag{5.11}$$

The second term on the right hand side of Equation (5.11) results in an artifact (marked by the black squares in Figure 5.8) which resembles a 180 deg-rotated version of the S_m distribution (marked by the triangles).

The distribution also shows that, in the case with 4% GD ripples, the bandwidth is compressed to the desired 8 GHz baseband bandwidth (16 GHz passband bandwidth). However, the case with 8% GD ripples results in 27 GHz intensity

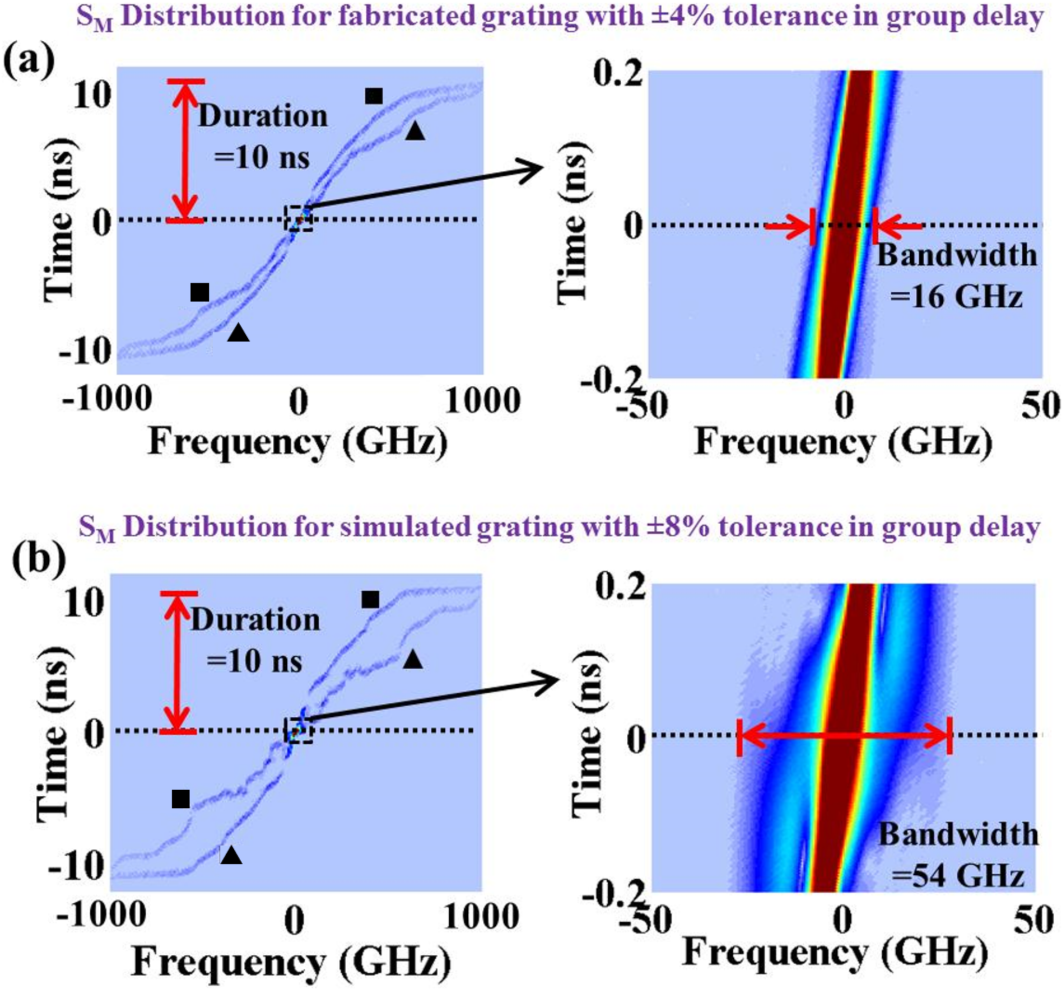

Figure 5.8: The S_m distribution can be used to analyze the effect of nonidealities on the performance of TBE systems. Here we have compared the S_m plots for two systems operating in the far field with (a) 4% and (b) 8% GD ripples, respectively, corresponding to the GD profiles shown in Figures 5.7(a) and (b). The "ideal" distribution is marked by black squares, and is accompanied by an artifact (marked by the black triangles) which is due to the GD ripples. This figure shows that the output modulation bandwidth in the far-field regime is determined mainly by the GD ripples at frequencies near the carrier frequency.

bandwidth. This suggests that, depending on its relative magnitude, GD ripples can dramatically impact the TBP in a TBE system. In the present example, limiting tolerances to 4% ensures the system reaches the desired 8 GHz output bandwidth, while the effect is mainly related to ripples near the carrier freqency. This can be seen by considering each vertical slice of the S_m distribution as a cross-correlation of the electric field spectrum.

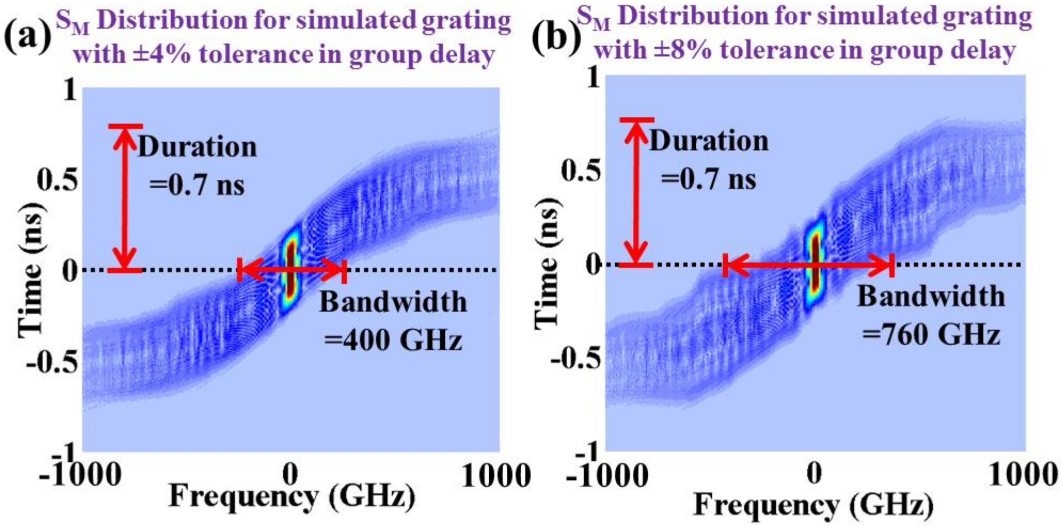

Figure 5.9: The S_m distribution can be used to analyze the effect of nonidealities on the performance of TBE systems. Here we have compared the S_m plots for two systems operating in the far field with (a) 4% and (b) 8% GD ripples, respectively, corresponding to the GD profiles shown in Figures 5.7(a) and (b). The "ideal" distribution is marked by black squares, and is accompanied by an artifact (marked by the black triangles) which is due to the GD ripples. This figure shows that the output modulation bandwidth in the near-field regime is determined mainly by the GD ripples at higher frequencies - the more near-field the optical output, the more likely bandwidth is determined by GD ripples at higher frequencies.

We have also investigated the use of S_m plots to analyze the effect of ripples on the TBP in the near field. The near-field GD profiles with 4% and 8% GD ripples are shown in Figures 5.7(a) and 5.7(b). The corresponding S_m distributions are shown in Figure5.9(a) and (b). Similar to the far-field case, the distribution plots also show that the effect of GD ripples on the output duration remains small and the main impact is on the output modulation bandwidth. In particular, in the case with 4% ripples the bandwidth is compressed to 200 GHz (400 GHz intensity bandwidth), as opposed to 380 GHz in the 8% case. However, relative to the ideal case, we find that the output bandwidth is dramatically increased. The ripple artifact found in the far-field case is not pronounced, since in the near-field conditions the difference in group delay shown on the right hand side of Equation 5.11 is comparable to the input time duration.

Finally, we note that, if the carrier wavelength is moved away from the center of symmetry of the GD curve, a different characteristic for the TBE system is achieved. In particular, “sub-linear” and “super-linear” descriptions assume the carrier wavelength is at the center of symmetry. If the carrier is moved away from the center of symmetry, we expect fromEquation (5.11) that this will lead to an increase in the temporal duration ΔT_{out} while the bandwidth increase follows similar principles as to what was discovered for GD ripples. The S_m distribution can be used to study such effects.

5.6 Conclusion

We have described foundations of optical methods to engineer the time bandwidth of information-carrying signals. Here the time represents the record length and the bandwidth is the modulation, i.e., the information bandwidth. To design such systems, we employ the S_m distribution, a mathematical tool that describes the bandwidth and temporal duration of the signal intensity (instantaneous power) before and after operation with a phase filter with an arbitrary GD. We provided closed-form mathematical expressions that describe how the signal's duration and bandwidth are shaped by the GD characteristics. We also showed how the distribution can provide visual insight and tolerances to nonidealities, such as GD ripples. Finally, the mathematical tools presented in this paper offer opportunities for follow-up work directed to detailed study of different implementations of the TBE system, including studying and benchmarking various GD profiles.

CHAPTER 6

SNR engineering with warped time stretch

6.1 Introduction

The signal-to-noise (SNR) ratio or, when distortion is introduced into the signal, the signal-to-noise-with-distortion (SNDR) ratio, is an important measure of signal fidelity acquired from non-ideal environments. The desire to improve it via signal processing is not new: indeed, a discussion on performance in sigma-delta analog-to-digital converters in terms of noise shaping is well established in literature [78–80]. We have previously demonstrated that warped stretch enables the engineering of the time-bandwidth product (TBP) of broadband optical signals in real time [53]. We would now like to extend this analysis to engineering the SNR and SNDR.

6.2 Mathematical framework

There are subtle but important differences between tailoring the TBP and tailoring the SNR. For TBP, both the temporal duration and the modulation bandiwdth are the global properties of the signal, and are generally constant for a given input waveform; it is meaningless to talk about "TBP per unit wavelength", for example. In contrast, the SNR of an acquired waveform can vary along the duration of a broadband optical signal, whether one considers the temporal or spectral domain. This is because the characterization of noise is ultimately a statistical one, which are quantified via some form of ensemble averaging. It therefore becomes meaningful to establish local and/or instantaneous SNR metrics of warped stretching, which can later on be averaged if desired. Here, we define the "instantaneous" SNR as that the average SNR over the integration period in the range of a given time sample.

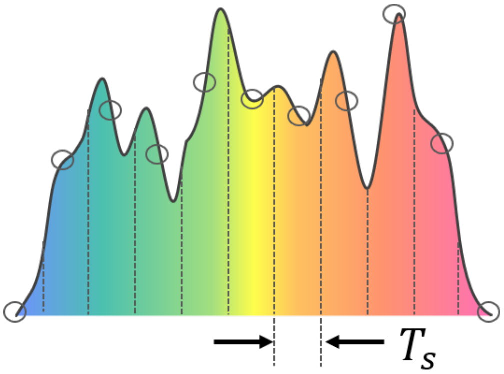

Figure 6.1: The "instantaneous" SNR is defined per sample at time $t = t_0 + nT_s$, averaged over the integration period of T_s.

There are two major ways that dispersion has over the SNR: the reduction in optical power and in the modulation bandwidth of the acquired waveform as the waveform is being time-stretched. We denote the optical power reduction factor as $\alpha(t)$ and the noise bandwidth reduction factor $\mu(t)$. There are multiple ways to define the power and bandwidth reduction factors: for example, in the previous section, we defined the two factors $\langle\alpha\rangle$ and $\langle\mu\rangle$ to be relative to the unstretched input pulse. Here, we define instead "local", or wavelength-dependent reduction factors, under a differential increase in dispersion δD_λ. The noise bandwidth is ultimately defined by the acquisition bandwidth (whether limited by the photodetector or the digitizer), which is constant, and thus technically we only need to match the overall bandwidth of the signal to the detection bandwidth requirements, and the expression for the global bandwidth as defined in chapter 5 would suffice. However, a local bandwidth measure would nevertheless aid the proper frequency-dependent design of the group delay profile to better match the signal spectrum.

Thus, for the local scaling factors, we assume that the stationary phase approximation is satisfied prior to the change in dispersion (one can consider this to referring be post-modulation dispersion $D_2 = \delta D_\lambda$). The instantaneous power and bandwidth will then be defined within a neighbourhood $\delta t = D_\lambda(\omega_s)L \cdot \delta\omega$ as defined by the spectral resolution $=\delta\omega$ of the system at a given time point t (and the corresponding frequency $\omega_s = \tau^{-1}(t)$). This spectral resolution can be limited by either the distortion from the frequency-to-time mapping itself, or the spectral resolution of the photodetector or analog-to-digital converter [1].

As shown in chapter 2, given an input optical spectrum $\tilde{E}_i(\omega)$, after the initial stretch D_1, the broadband envelope electric field intensity is $|E_{D1}(t)| = \frac{|\tilde{E}_i(\omega-\omega_c)|}{\sqrt{2\pi|\tau'_{D1}(\omega_s)|}}$. After the modulation event $s(t)$ and the second stretch with dispersion $D_2 = \delta D_\lambda$, the signal intensity can now be written as $|E_{D2}(t)| = |\mathcal{E}_{D2}(t)| \cdot s_{TS}(t/M(t))$, where $|\mathcal{E}_{D2}|$ is the electric field intensity of the carrier envelope, and s_{TS} is the envelope modulation that has been time-stretched by a factor of $M(t)$. The broadband carrier envelope $\mathcal{E}_{D2}(t)$ now has an intensity of $\frac{\tilde{E}_i(\omega_s)}{\sqrt{2\pi|\tau'_{tot}(\omega_s)|}}$. Therefore, the reduction in optical power (which is proportional to the square of the electric field intensity) is:

$$\alpha(t) = \frac{\tau'_{tot}(t)}{\tau'_{D1}(t)} \approx 1 + \frac{\delta D_\lambda}{D_1} = M(t) \tag{6.1}$$

where $M(t)$ is the generalized stretch factor as shown in Chapter 2. Thus, the instantaneous power reduction factor of the acquired waveform at time t is equal to its instantaneous stretch factor $M(t)$ (which we have taken the liberty to express in terms of time, possible due to the frequency-to-time mapping enabled by the stationary phase approximation). Note that strictly speaking, the modulation event need not be after the second stretch, but also prior to the first stretch, but the same argument follows.

For the instantaneous bandwidth, we follow the methodology in [1] and first define a local bandwidth measure B_t associated with each time point t over a neighbourhood of δt. Although not limited to such, one example of a local bandwidth measure is the a temporal slice of the short-time Fourier transform (STFT) that is centred at t. Given a choice of local bandwidth measure, the overall bandwidth can then be expressed as $\Delta\Omega = \max_t \{B_t\}$. Note that the bandwidth $\Delta\Omega$ should be approximately equal to the bandwidth expression found in (5.9) of chapter 5, as long as the same ADC ENOB is assumed to define the cutoff magnitude at which the bandwidth is measured. It should be noted that we assume the use of a photodetector with a fixed analog receiver circuit and digitizer with a fixed sampling rate; these define a fixed noise bandwidth. We hence use a fixed value for the overall bandwidth expression since we physically assume a proper design of the signal stretch such that it is bandlimited to match the noise bandwidth.

As aforementioned, after the optical modulation has been stretched by the dispersion δD_λ, the signal (with local bandwidth $\{B_t\}$ and overall bandwidth $\Delta\Omega_{D1}$) at each time t is slowed down by a factor of $M(t)$. Thus, the stretched signal after dispersion δD_λ has a bandwidth $\Delta\Omega_{tot} = \max_t \left\{\frac{B_t}{M(t)}\right\}$, and:

$$\mu(t) = \frac{\Delta\Omega_{D1}}{\Delta\Omega_{tot}} = \max_t \left\{\frac{M(t)}{B_t}\right\} \max_t B_t \tag{6.2}$$

To give an expression for the instantaneous SNR gain for a photocurrent $i(t)$ at time t, let us first assume a signal with ASE-limited noise floor, with an ensemble-averaged noise photocurrent of $i_{\mathrm{ASE}}(t) = 2qGi(t)\Delta\Omega$, which is sampled by an ADC with sampling rate F_s. The net gain in the instantaneous SNR G_{SNR} can be shown to be:

$$\begin{aligned} G_{\mathrm{SNR}} &= 10\log_{10}\left(\frac{i(t)/M(t)}{2qGi\Delta\Omega_{tot}/2\pi}\right) - 10\log_{10}\left(\frac{i(t)}{2qGi(t)\Delta\Omega_{D1}/2\pi}\right) \\ &= -10\log_{10}\left(M(t)\right) + 10\log_{10}\left(\max_t\left\{\frac{M(t)}{B_t}\right\}\max_t B_t\right) \\ &\equiv -10\log_{10}(\alpha) + 10\log_{10}(\mu) \end{aligned} \tag{6.3}$$

where the first term after the last equal sign corresponds to the instantaneous loss due to power reduction, whereas the second term corresponds to the gain due to reduced bandwidth. As dispersion is ultimately a linear process (and hence conservative when assuming lossless conditions), it can be shown that if we use the "instantaneous" bandwidth measure directly for the output bandwidth, it can be shown that $\mu(t) = \alpha(t)$, and the SNR gain is always zero.

If we design the stretch factor $M(t) \propto B_t$ to match the local bandwidth at every time point t, then the gain can be simplified to become:

$$G_{\mathrm{SNR}} = 10 \log_{10} \left(\frac{\max_t M(t)}{M(t)} \right) = 10 \log_{10} \left(\frac{\max_t B(t)}{B(t)} \right) \tag{6.4}$$

In the specific case of linear stretch, Equation (6.4) again reduces to zero; this matches our result using the stretched modulation distribution in Chapter 5.

To then capture the time dependent effects of the tailored dispersion, we now define the instantaneous SNR of the output signal as:

$$SNR_i(t) = \frac{P_{out}(t)}{\sum_j N_j(t)} \tag{6.5}$$

where the instantaneous input signal power$P_{out}(t) = i_{out}^2(t)R$ and the noise powers $\{N_j(t)\}$ are understood to be time-averaged over a duration equal to the time resolution of photo detection and analog-to-digital conversion, whichever is limiting.

6.3 Simulations

Following the result in Equation (2.5), the output photocurrent $i_{out}(t)$ following photodetection in a singly dispersed optical system can be described as:

$$i_{out}(t) = \frac{c\epsilon_0 n r_d}{4\pi} \left[\tau_g'(\Omega_s)\right]^{-1} \left|\tilde{E}_{in}(\Omega_s)\right|^2 \tag{6.6}$$

where r_d is the detector responsivity, c is the speed of light, ϵ_0 is the vacuum permittivity, n is the refractive index of the medium, and$\tilde{E}_{in}(\Omega_s)$ is the electric field spectrum. Implicit in the equation is the frequency-to-time mapping; for an input signal with negligible chirp relative to the added dispersion of the optical system, we have the mapping of the envelope angular frequency $\Omega_s = \tau_g^{-1}(t)$ to a corresponding time t, given dispersive elements with a total group delay of $\tau_g(\Omega_s)$.

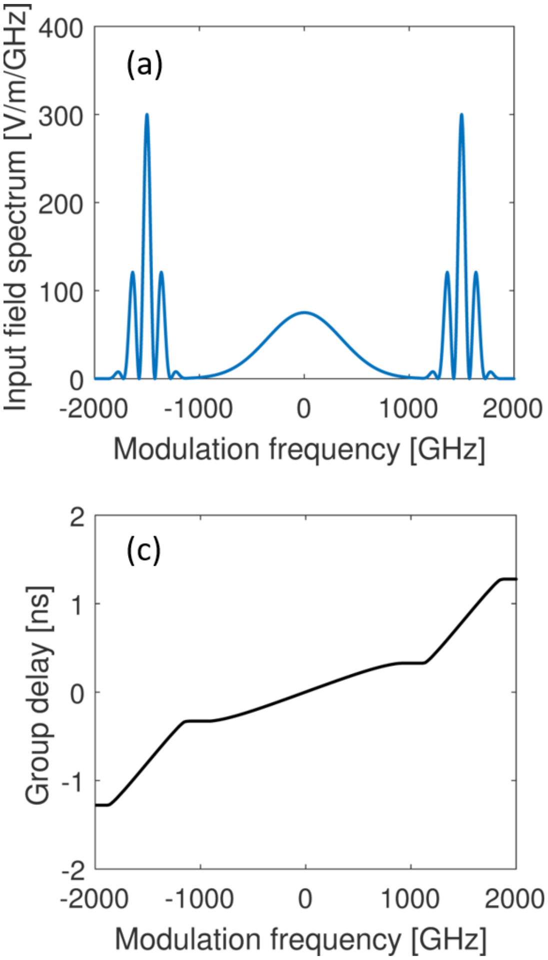

Figure 6.2: (a) Electric field of input test signal. (b) Electric field spectrum amplitude of input. (c) Group delay of dispersive element. (d) Amplified output photocurrent in time. Note the occurrence of the warped frequency-to-time mapping between subplots (b) and (d).

Figure 6.3 shows the simulated setup. The SNR was simulated, taking into account the relative intensity noise (RIN) of the laser (0.1% relative to the electrical

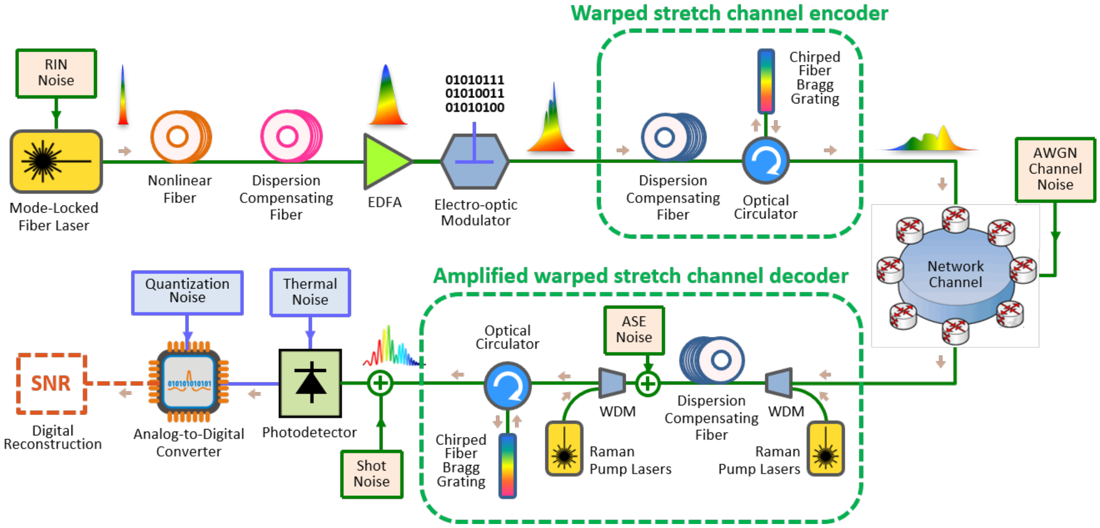

Figure 6.3: Schematic of the simulated setup, including noise sources

bandwidth, for a propagation length of $L_{eff} = 1\,\mathrm{km}$ and $100\,\mathrm{mW}$ pump power, following the metholodogy outlined in [81] and [57]), AWGN channel noise (noise factor = 20 with respect to thermal noise), thermal noise ($T = 300\mathrm{K}$), shot noise and ASE noise (with an amplifier gain of 5) of the photocurrent, then quantization noise from digitization (ENOB = 8 bits). All noise sources other than quantization noise assume AWGN statistics in the time domain, such that the noise powers area summable. In the simulation, an optical test signal is passed through a tailored dispersive element, then photodetected and digitized. The input optical power was varied to investigate the effect of the power scaling $\alpha = \langle\alpha(t)\rangle$ on the SNR. For the bandwidth reduction factor μ, both the group delay and the detection bandwidth of the photodetector were simultaneously varied, such that the simulated setup always remains at the optimal detector bandwidth.

6.4 Results and discussion

Figure 6.4 shows the effect of scaling the input power on the SNR of a warped stretch system. The SNR can be considered in three regimes: the thermal noise-

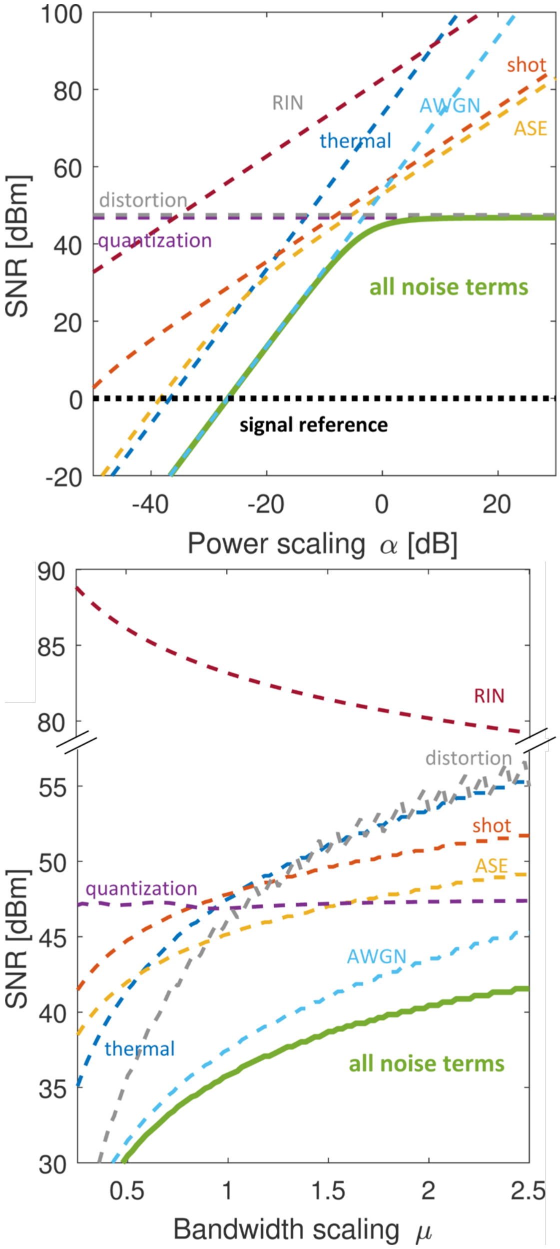

Figure 6.4: (a) Power and (b) bandwidth reduction scaling of the instantaneous SNR. The SNR in general has three regimes: the thermal noise-limited regime (SNR scaling by $(\alpha\mu)^2$), the shot and ASE noise-limited regime (SNR scaling by $\alpha\mu$), and the quantization noise-limited regime (SNR constant with input power).

limited regime occurs at low signal powers and high bandwidths (where the SNR scales by $(\frac{\mu}{\alpha})^2$). At moderate stretch factors, we encounter the shot and ASE noise-limited regime (SNR scaling by $\frac{\mu}{\alpha}$), and, finally, the quantization noise-limited regime (where SNR is constant with input power).

Overall, while the instantaneous SNR is limited at high optical powers by the quantization noise, the instantaneous SNR can be improved for weak portions of the signal which are below this threshold. This is achieved by a decrease of dispersion (i.e. increase in α) in the corresponding spectral region of the input. Meanwhile, the increase in dispersion (i.e. increase in μ) can improve the SNR by creating oversampled regimes of fast, high power signal portions. Noisy weak signals can thus be SNR-boosted, as long as prior knowledge exists of the input spectrum. The combined degree of warped stretch in which the gain is opitmized depends on the spectral shape of the input pulse and the limiting noise source at a given input power along the signal.

6.5 Conclusion

Our simulation results show that it is possible to manipulate both the power and bandwidth of the optical signal, which allows us to engineer the SNR. Given statistics of a non-stationary optical pulse train, the group delay can be designed to optimize the effective sampling rate at detection, which improves the SNR for signals in which fast and high power portions exists. The results with warped stretch also show the potential for optical encryption by engineering a dispersive element according to the signal's time-averaged spectral characteristics. A broadband signal can be buried under noise floor upon transmission. Upon reception, the inverse dispersion is used to reproduce the optical data. Given prior knowledge of a signal's spectral statistics, its SNR can be manipulated (boosted or lowered) in a reversible way. This has applications to weak signal detection and in cybersecurity.

CHAPTER 7

Dynamic chromo-modal dispersion for reconfigurable dispersion profiles

7.1 Introduction

Dynamic correction for temporal distortions (e.g. from chromatic dispersion or polarization mode distortion), over sub-ns timescales is a desirable functionality in modern 10-100s-of-Gb/s optical telecommunications systems [82]. Current solutions to this problem in long-haul communications include digital correction with coherent detection [82], passive correction with dispersion compensation fibers [83] or fiber Bragg gratings [84]. Dispersion engineering also has application in time stretch systems for real-time acquisition of fast dynamic phenomena [9, 85].

Chromo-modal dispersion (CMD) provides a passive alternative to the use of dispersion compensation fibers and fiber Bragg gratings. In CMD, the incidence angle-dependent waveguide dispersion of multimode fibers is exploited to generate chromatic dispersion [86]. By dispersing a modelocked pulse with a spatial grating, then focusing into a multimode waveguide, a one-to-one wavelength-to-angle mapping can be achieved, such that different wavelength excites different spatial waveguide modes for chromatic broadening. This mapping can be further fine-tuned with customized hyperbolic mirrors [9, 32, 87]. The mapping of excitation angle to wavelength and RF frequency has previously been used to create new types of dynamic light scattering techniques for blood cell characterization [31,88], where the proposed technique may find additional applications.

While the zero-dispersion wavelength can be shifted, reconfigurability in CMD remains limited. To render temporal corrections as truly dynamical, we generalize the chromo-modal dispersion technique with acousto-optic switching to provide real-time temporal control of dispersion. We call this generalization dynamic CMD to distinguish the technique from CMD. Here we demonstrate its application to narrowband pulses but over a large operational bandwidth.

7.2 Experimental setup

Figure 7.1 shows the proof-of-concept experimental setup. A tunable 1550-nm CW fiber laser is modulated with 200-ps pulses (10 MHz repetition rate), then amplified with an EDFA and passed through the acousto-optic deflector (AOD). The first-order AOD-diffracted beam is then coupled into an multimode waveguide, where it is photodetected at the output. While the technique is not limited by the waveguiding structure chosen, we choose to use a multimode fiber (MMF) with a numerical aperture of NA = 0.37 and core diameter r of 200 µm.

The AOD incidence angle is $\theta = \sin^{-1}(\frac{F\lambda}{2v_a})$, where λ is the optical wavelength, and v_a is the AOD acoustic velocity. It can be tuned by varying the AOD input RF frequency F, which in turn couples the optical beam to a different Laguerre-Gaussian (L-G) fiber mode. Each fiber mode with its associated temporal delay:

$$\tau_d(\lambda) = \frac{n_1 L}{c}\sqrt{1 - \left(\frac{1}{n_1}\right)^2 \left[1 + \left(\frac{f_2}{f_3}\frac{F\lambda}{2v_a}\right)^2\right]^{-1}} \tag{7.1}$$

where n_1 is the refractive index of the fiber core, L is the fiber length, and f_2,f_3 are the focal lengths of the post-AOD telescoping lens, as indicated in Figure 7.1. By selecting the desired waveguide mode with the corresponding AOD RF frequency, the temporal position of the input pulse can therefore be dynamically reconfigured. Furthermore, the pulse can also be attenuated by reducing the AOD RF power, which decreases the diffraction efficiency.

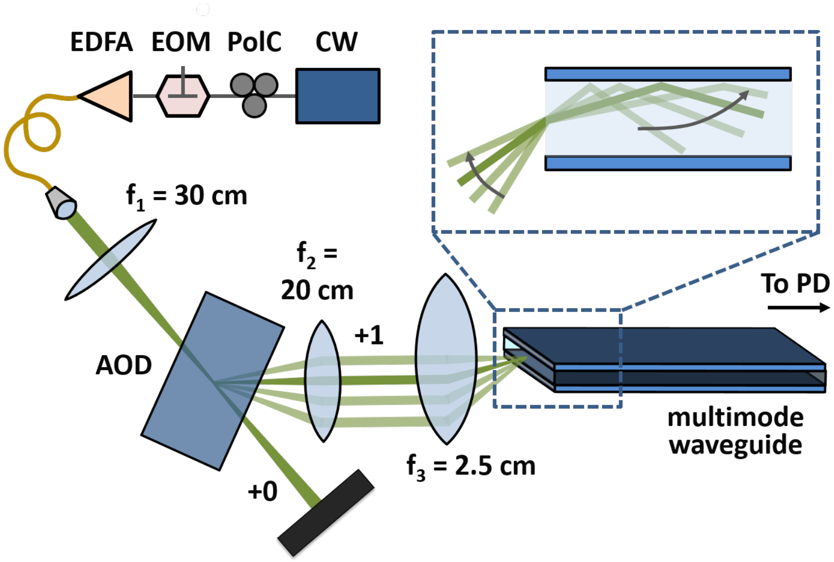

Figure 7.1: Schematic of the dynamic chromo-modal dispersion (dynamic CMD) setup. A tunable 1550-nm CW fiber laser is modulated with 200-ps pulses with an EOM, then amplified with an EDFA. The pulses are collimated into free space and focused into an AOD. The first-order diffracted beam is coupled into a multimode waveguide (here we use a multimode fiber), where it is photodetected at the output. The incidence angle into the AOD can be tuned by varying the RF frequency of the AOD input, which in turn couples to a different Laguerre-Gaussian (L-G) fiber mode in the multimode fiber (MMF), each with its own associated delay. By selecting the desired L-G waveguide mode, the temporal position of the input pulse can therefore be dynamically reconfigured.

7.3 Results and discussion

Figure 7.2 shows the excited L-G modes of the MMF, which correspond to different AOD RF frequencies. As only $LG_{0\ell}$ modes are being excited across the range of the AOD RF sweep, this validates the use of the temporal delay formula in the text, which is only valid for meridional rays. In general, a ray-optics derivation for skew rays can be found in [89]; however, skew rays are avoided for our application, as it broadens the linewidth of the output – which lowers the resolution of the dispersion

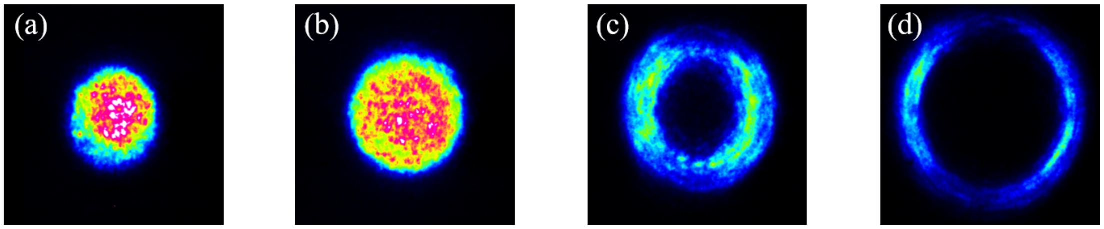

Figure 7.2: Beam profile corresponding to RF frequencies of (a) 110, (b) 130, (c) 150 MHz, and (d) 170 MHz, respectively.

– and unecessarily increases the insertion loss [90]. Note that the annulus thickness and amplitude of the $LG_{0\ell}$ mode decreases with increasing excitation radius $r_\ell \approx \sqrt{\frac{|\ell|}{2}}w_0$, where w_0 is the beam waist parameter of a Gaussian mode. The lower amplitude is due to a lowered coupling efficiency at large MMF incidence angles from a decreasing overlap integral, in addition to lower peak values from the nornmalized theoretical expression; the lower intensity also causes the annulus thickness to be perceived as thinner despite being wider with increasing ℓ .

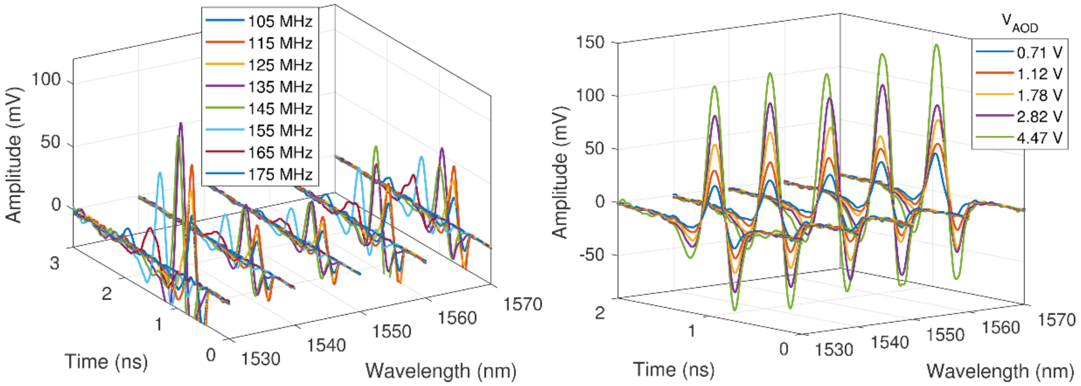

Figure 7.3: (a) Tunability in pulse position for different optical wavelengths. (b) Tunability in pulse amplitude at different optical wavelengths.

Figure 7.3(a) and (b) demonstrates the tunability over pulse amplitude and position, respectively, over the wavelength range of the tunable CW laser, demonstrating a delay range tunable over 1.27 ns over 40 nm of optical bandwidth. Fig. 7.3(a) also shows that the wavelength range was limited by the tunable range of the CW laser, and that the overall effect of chromatic dispersion is negligible.

In the current setup, the system resolution can be limited in terms of the number of MMF modes M, which is approximately $M \approx V^2/2$ [cite JM Liu], where $V = \frac{2\pi r}{\lambda}$ NA is the V-number of the fiber. For our system, this would correspond to $M \approx 11250$. The resolution can also be limited by the acquisition bandwidth [1,2]; however, the photodetector and digitizer were chosen to be larger than the signal bandwidth and thus is not limiting.

7.4 Conclusion

We have demonstrated dynamic tuning of dispersion by acousto-optic mode excitation of a multimode structure offering tuning of optical dispersion via RF frequency. Also featuring wavelength tuning, our device achieves real-time temporal tuning of narrowband pulses over 1.27 ns and 40 nm of optical bandwidth. It also provides amplitude control, making it potentially useful for amplitude distortion compensation in single optical telecommunications channels, as well as the tuning of virtual imaging phase array (VIPA) devices [91].

CHAPTER 8

Warped stretch image compression

8.1 Introduction

Digital image compression is required for practical storage and transfer of digital images. In addition to conventional photography and online photo sharing applications, it is employed in astronomy [92–94], remote sensing [95–97], machine vision [98,99], digital pathology and radiology [17,100,101], real-time system monitoring [102, 103], and particle-tracking velocimetry [104].

Our prior work has considered the potential for image compression of a process whereby the image is intentionally distorted such that sharp features are self-adaptively expanded before uniform downsampling. The discrete anamorphic stretch transform (DAST) [105] Is inspired by the physics of photonic time stretch, an analog signal processing technique which employs a frequency-dependent all-pass filter with a group delay $\tau(\omega) = \frac{\mathrm{d}\phi(\omega)}{\mathrm{d}\omega}$ to slow down fast analog temporal waveforms so they can be digitized in real time [10, 33, 37, 106]. By doing so, photonic time stretch has led to the discovery of optical rogue waves [59], the creation of a new imaging modality known as the time stretch camera [16], which has enabled detection of cancer cells in blood with record sensitivity [17] and a portfolio of other fast real-time measurements, such as an ultrafast vibrometer [20], the discovery of soliton explosions [26] and the observation of relativistic electron structures [27]. While time stretch slows down the fast time series so it can be digitized in real-time, it conserves the time-bandwidth product. Recently, it has been shown that this product can be reduced or expanded for the information carried by the signal envelope, leading to time-bandwidth engineering [53]. This in turn has led to the concept of the "information gearbox" [107], as well as photonic hardware accelerators, for real-time data acquisition, analytics and high performance computing [32].

In DAST, two dimensional discrete spatial coordinates $[x, y]$ replace one dimensional time coordinate t. A warped version, $\tilde{E}[x, y]$, of the input image $E[x, y]$ is generated by applying a warp kernel $\tilde{K}[u, v]$ to the input spectrum $\tilde{E}[u, v] = \mathcal{F}\left\{E[x, y]\right\}$ in the following transformation:

$$\tilde{E}[x, y] = \left|\mathcal{F}^{-1}\left\{\tilde{E}[u, v]\, \tilde{K}[u, v]\right\}\right|, \tag{8.1}$$

where $\mathcal{F}^{-1}$ is the two-dimensional discrete inverse Fourier transform operator. The warping kernel preferentially stretches the sharp features so that it can be downsampled at rates much lower than what was previously possible with naïve uniform downsampling. This property is conducive to image compression and its digital implementation has also led to a new powerful edge detection algorithm for extracting features from digital images [108].

As seen in Equation (8.1), the warped mapping is performed in the frequency domain. Image reconstruction then requires knowledge of the phase of the transformed image. In the previous work, ideal phase recovery was assumed to show the potential of warped stretch for data compression [105]. The accuracy of phase recovery from intensity (brightness) data is subject to the signal to noise ratio (SNR) [109–114] and this limits the fidelity of image reconstruction from dewarping [54].

Here, we report a related approach to warped stretch that does not require phase recovery. This physics-inspired numerical algorithm is inspired by the recent report of the first demonstration of analog image compression [3]. In this technique, a laser pulse is spread out spatially into a one-dimensional rainbow by a diffraction grating, then incident onto a single line of the input sample. Pixels of the to-be-compressed image are therefore mapped onto this incident laser pulse rainbow as intensity changes in each wavelength along the 1D rainbow. The pulse is then time stretched with a fiber Bragg grating with a highly nonlinear group delay profile that imparts warped mapping of spectrum (space) into time. The resulting temporal signal is digitized followed by reconstruction by performing inverse mapping numerically. Similar to the previous compression method, the non-linear dispersion relation of the optical fiber functions as the warp kernel. Since the image information is mapped directly onto the signal spectrum, no phase recovery is needed.

We are inspired to implement this process in a numerical algorithm and investigate its utility for application to digital image compression. In this technique, the input signal is directly warped then uniformly sampled. This two-step process achieves context-aware non-uniform sampling but without the need for Fourier transformation and phase recovery. With proper design of the warp kernel [1], sharp spatial features are stretched much more than slow-varying ones in a context-aware manner. The redistribution of the local signal entropy lowers the overall Nyquist sampling rate and is the basis of the “information gearbox” concept proposed in [32] and [107].

8.2 Methods

Figure 8.1 illustrates how the direct warped stretch transform can be used as a compression codec. We consider signal-dependent warp kernels that are specifically tailored to the spatial sparsity patterns in the input signal for optimal non-uniform sampling. Since the warp kernel is signal-dependent, it must also be sent along with the downsampled image as reconstruction metadata. The compressed

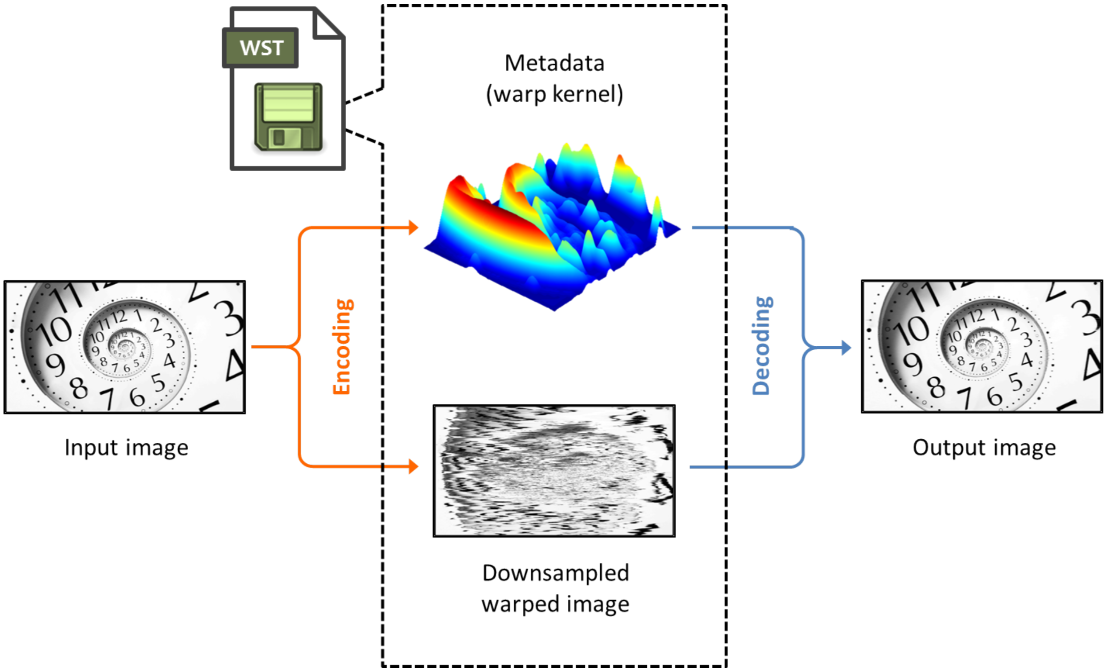

Figure 8.1: Overview schematic for image compression codec with warped stretch. The input is split into two components: i) the downsampled warped image and ii) the metadata, which contains a compressed version of the warp kernel. These two components are jointly used for recovering the original input. Since the warp kernel is image-dependent, we must send it as part of the compressed file, which creates extra overhead relative to an image-independent compression technique, such as uniform sampling. However, if the metadata can be compressed extremely compactly, the overall compression ratio can still be significant.

image can then be recovered by de-warping and upsampling.

Traditional non-uniform sampling avoids the overhead associated with the metadata by considering irregularly spaced samples in 2D space (such as 2D contours [115, 116]), by requiring strong statistical assumptions on the input [117], or by ignoring the need to know the positions of the non-uniform samples [118]. The overhead associated with knowing the sample positions in conventional non-uniform sampling is equivalent to the metadata that contains the warp kernel in our approach. Furthermore, the information about sample position in such techniques is often non-sparse and thus the overall compression from non-uniformly sampling will be limited by the compressibility of the sample position metadata. This important problem is mitigated in our approach because the warp kernel only specifies the recommended local sampling density of the image, not the exact sampling locations. This results in a more compact metadata albeit at the cost of a marginally lower SNR.

Additionally, separating the warping information from both the downsampling stage and the exact image pixel locations frees us to re-use the warp kernel elsewhere. For example, in the situation where one wants to compress the same file at a different quality, the same warp kernel design can be re-used at different downsampling rates (i.e. compression ratios), thus reducing the overall pre-processing burden. Alternatively, one can consider simultaneously compressing any set of inputs that share similar sparsity statistics (e.g. different colour channels, passport photo libraries) together, by generating a single warp kernel tailored to warp the "average" of the input set.

As a proof-of-concept demonstration, we show the performance of warped stretch compression using piecewise decomposition of the warp kernel. Figure 8.2 shows this implementation. We emphasize that this is just one instantiation of the general compression scheme shown in Figure 8.2; other implementation schemes are possible with potentially better performance.

The optimal warp kernel is designed according to the methodology adapted from [1]. In [1], the short-time Fourier transform (STFT) was employed to evaluate the relative local bandwidth $B_\omega(\omega)$ of the input spectrum (called the "frequency of spectrum"). When hardware bandwidth limitations do not exist, the required bandwidth to capture the stretched signal can be expressed as:

$$B_\omega(\omega) = \frac{1}{4\sqrt{\pi}} \sqrt{\frac{\mathrm{d}\tau_g(\omega)}{\mathrm{d}\omega}} \tag{8.2}$$

This relates the ideal 1D warp kernel $\tau_g(\omega)$ to the local bandwidth via its deriva-

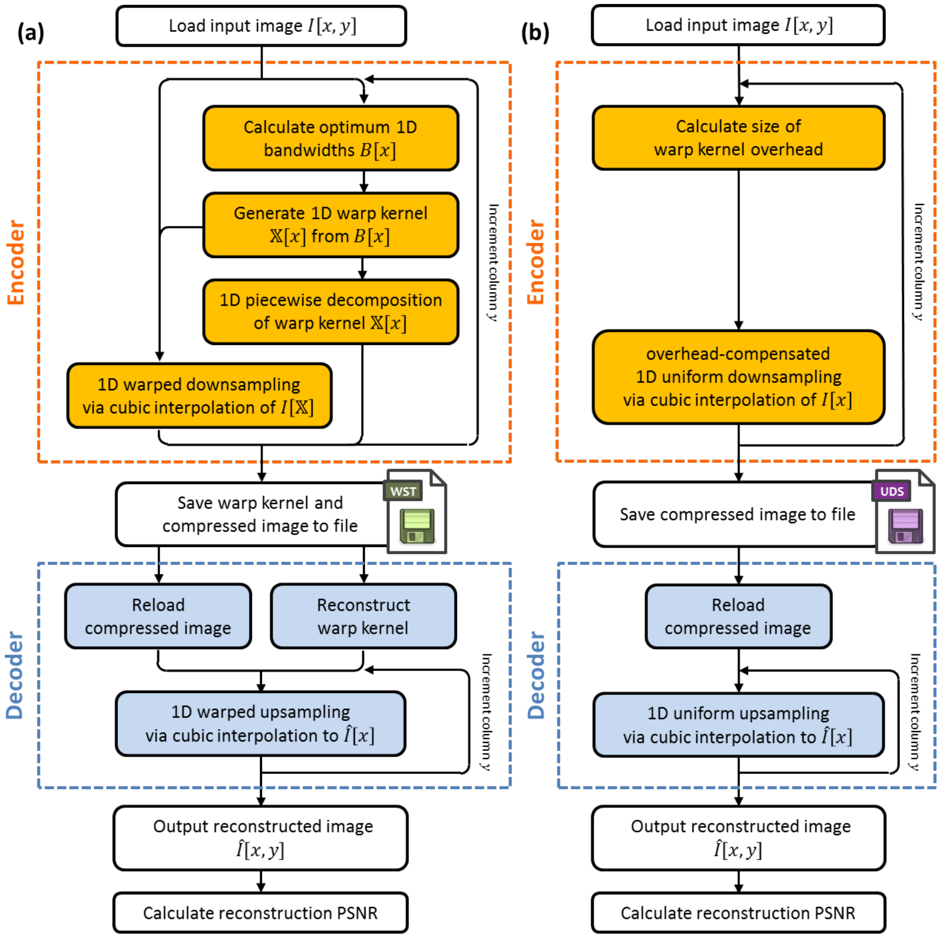

Figure 8.2: Flowchart for warped stretch compression using piecewise decomposition. (a) A separate warp kernel is generated for each row of the image. The warp is based on the local row bandwidth, i.e. the derivative of the image intensity. The input image is then warped by the kernel and downsampled at a uniform rate. The compressed image is then saved into a custom binary file format (WST), along with the warp kernel, which itself is compressed via piecewise decomposition. To reconstruct the image, we decompress the piecewise-decomposed warp kernel and use it to perform non-uniform upsampling on the reloaded compressed image. (b) For comparison purposes, we also uniformly downsample the input image in 1D with a lower downsampling rate that accounts for the warp kernel overhead saved in the WST binary format.

tive:

$$\tau_g(\omega) = \int \left| \frac{\mathrm{d}\tau_g(\omega)}{\mathrm{d}\omega} \right| d\omega \tag{8.3}$$

The method in [1, 3] guarantees a warp kernel that is ideal for minimizing the time-bandwidth product of the signal envelope in 1D. In terms of compression, the ideal warping kernel for image compression should minimize the Nyquist sampling rate after stretching. Given a discrete bandwidth measure $B_x[x]$ and barring any additional constraints imposed by the compression itself (e.g. kernel overhead constraints), the ideal sampling locations after warping $\mathbb{X}[x]$ are those which reshape the bandwidth of the warped output $B_{\mathbb{X}}[\mathbb{X}]$ to be as close as possible to the average original bandwidth $\langle B_x[x] \rangle$ across the image row:

$$\arg\min_{\mathbb{X}} \left\| B_{\mathbb{X}}[\mathbb{X}] - \langle B_x[x] \rangle \right\|_1 \tag{8.4}$$

We will limit our consideration to kernels that provide ideal one-to-one warped mapping, as defined by the warp kernel $\tau_g = \mathbb{X}[x]$. Note that while we have borrowed the mathematical notation used in [1, 3, 119], here original and warped sampling locations x and $\mathbb{X}[x]$ both denote pixel locations and no longer carry physical meaning. A kernel bandwidth measure $B_{\mathbb{X}}[\mathbb{X}]$ that simultaneously minimizes Equation (8.4) and provides one-to-one mapping is possible for an STFT window size of 2 pixels, in which case the STFT reduces to the magnitude of the discrete signal derivative $\left|\frac{\Delta \tilde{E}}{\Delta \mathbb{X}}\right|$:

$$B_{\mathbb{X}}[\mathbb{X}] = \left| \frac{\Delta \tilde{E}[x]}{\Delta \mathbb{X}[x]} \right| = \left| \frac{\Delta \tilde{E}}{\Delta x} \right| \left| \frac{\Delta \mathbb{X}}{\Delta x} \right|^{-1} \tag{8.5}$$

where $\Delta x = x_i - x_{i-1}$ is the original (uniform) sample spacing, and $\Delta\mathbb{X}[x_i] = \mathbb{X}[x_i] - \mathbb{X}[x_{i-1}]$ is the non-uniform sample spacing. Due to the differing objectives of optimization, we see that the derivative of the kernel is now inversely proportional to the bandwidth measure, instead of having a quadratic dependence, as shown in Equation (8.2). Using the same bandwidth measure for the original signal, i.e. the magnitude of the signal derivative, we find that the expression in Equation

(8.4) can be minimized with:

$$B_{\mathbb{X}}[\mathbb{X}] = \langle B_x[x] \rangle \triangleq \left\langle \left| \frac{\tilde{E}[x]}{\Delta\mathbb{X}[x]} \right| \right\rangle \tag{8.6}$$

Using Equations (8.3), (8.5) and (8.6), we then arrive at our expression for the optimal kernel:

$$\mathbb{X}[x] = \sum_i \left| \frac{\Delta\tilde{E}[x_i]}{\Delta x} \right| \frac{\Delta x}{\langle B_x[x] \rangle} = \sum_i \frac{\left| \Delta\tilde{E}[x_i] \right|}{\left\langle \left| \frac{\Delta\tilde{E}[x]}{\Delta\mathbb{X}[x]} \right| \right\rangle} \tag{8.7}$$

To compress the input image, the kernel is applied via cubic interpolation, and the warped output is uniformly downsampled. Because of the redistribution in local entropy, this downsampling rate is in general greater than a uniform downsampling rate that achieves the same resultant image quality. It should also be noted that Equation (8.6) implies that images with high average bandwidth $\langle B_x[x] \rangle$ will also have limited compressibility.

Representing the metadata, the kernel itself is compressed via piecewise decomposition: compression is achieved by saving only the positions of the turning points of each kernel row, which are identified by placing an energy threshold on the discrete derivative of the local bandwidth $B_x[x]$. Alternatively, STFT with a larger window size can be used, but this will be computationally more expensive.

As an initial demonstration, we used an 8-bit 1672 × 2800-pixel image of a grayscale fractal clock and performed compression on each row. The compressed image (saved with 8-bit precision) was saved along with the metadata kernel (saved in single precision) in a custom binary file format, identified with extension WST. To reconstruct the input image, the sampling positions of the compressed image were regenerated by the piecewise-decomposed warp kernel by cubic interpolation, then used to perform non-uniform upsampling on the reloaded compressed image (again by cubic interpolation).

To benchmark our results, we created a similar binary file containing the uniformly downsampled image (saved at a bit depth of 8 bits). To normalize our compression performance over file size, we decreased the uniform downsampling rate such that the resultant file size was equal to the file size of the WST binary file, which contains the metadata kernel in addition to the compressed image. The reconstructed images were then compared in terms of the peak signal-to-noise ratio (PSNR) relative to the original input image.

8.3 Results and discussion

Figure 8.3 shows the warping / de-warping process for one row of the fractal clock image at 6x compression. The waveform is first rescaled using non-uniform cubic interpolation as defined by the warp kernel generated for this row. In this warped state, the signal can now be downsampled at a uniform rate that is lower than what is possible using uniform downsampling, with equivalent reconstruction quality. Both the warping and the downsampling operations can be reversed to reconstruct the original line signal, and can be seen as abstractions of the analog spectrotemporal reshaping operations, fulfilling the role of an information gearbox [32].

In principle, the warping process redistributes the signal, such that the local entropy becomes uniformly distributed. However, as mentioned in the previous section, the ideal warp kernel is overly complex (i.e. as complex as the input itself) and thus merits compression. In the present case, this was achieved by piecewise decomposition. Compressing the warp kernel results in some loss of information in the overall compression; this is reflected in the non-ideal allocation of points in Figure 8.3(b).

Figure 8.4 compares the reconstructed fractal clock images from the warped stretch compression and the uniformly downsampled compression methods at an overall compression ratio of 4x and 5.3x compression, respectively. Even after the rate in the uniform downsampling case was decreased to account for not having

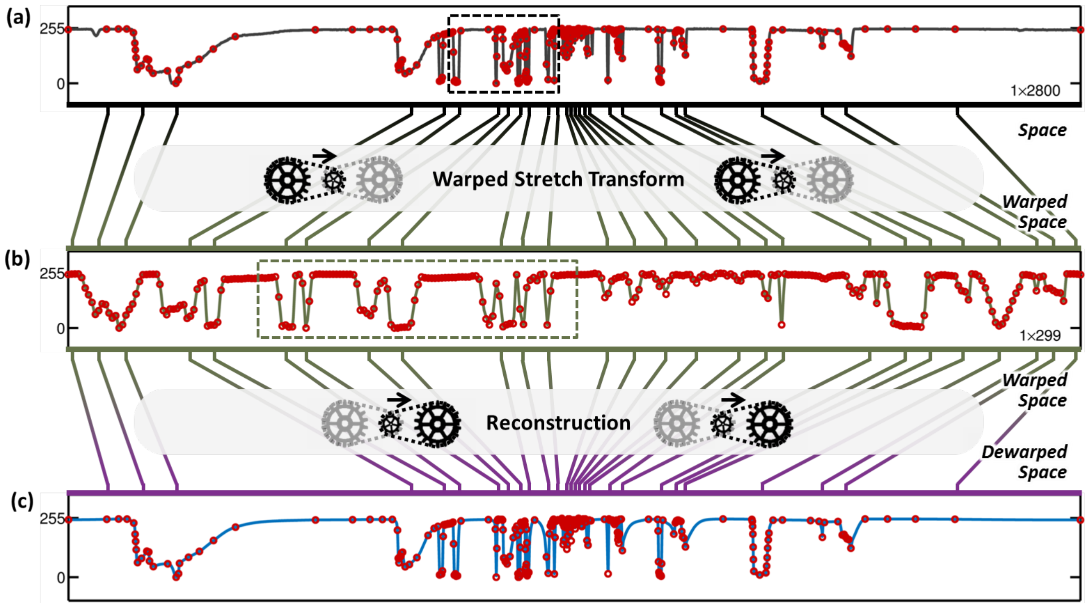

Figure 8.3: Results for row 838 (out of 1672) of the fractal clock image at 6x warped stretch compression with overhead compensation. The line signal (a) is first rescaled using non-uniform cubic interpolation as defined by the warp kernel, generated according to Equation (8.7). In this warped space (b), the signal can now be downsampled at a uniform rate (indicated by the red circles) that is lower than what is possible using uniform downsampling, at a given reconstruction quality. The number of downsampled points is less than 1/8th of the number of pixels in the original line signal so that the compression ratio becomes 8x after taking the warp kernel overhead into consideration when saving to file. Both the warping and the downsampling operations can be reversed to reconstruct the line signal (c). The corresponding locations of the downsampled points (red circles in (b)) overlay the (a) original and (c) reconstructed line signals for visual reference. The dashed frames in (a) and (b) in particular denote a one-to-one correspondence of the same sample sub-region.

to save any kernel (which improved its output quality), the warped stretch image (Figure 8.4(h)) still significantly outperforms the uniformly downsampled image (Fig 8.4(e)). This is confirmed by an overall PSNR improvement of 6.32 dB.

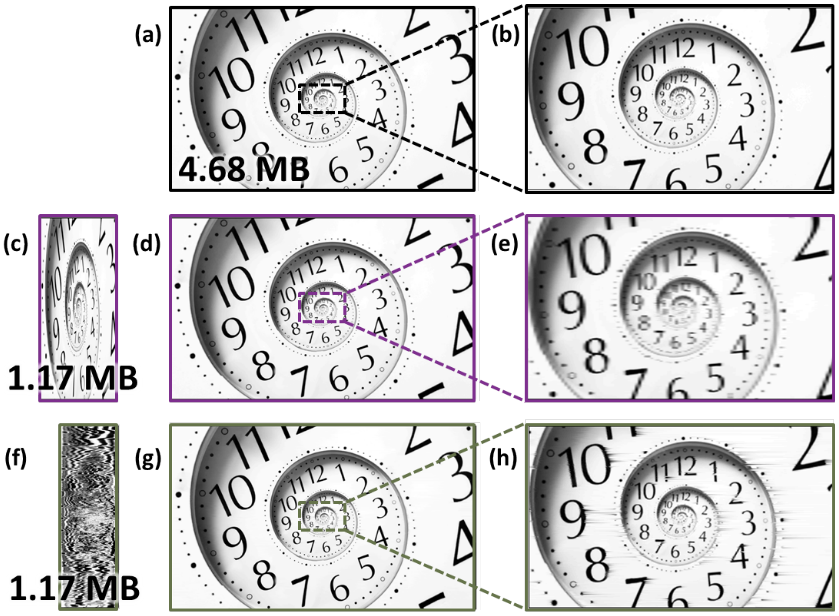

Figure 8.4: Comparison of compression performance with the fractal clock image. The original input image (a-b) and the 4x uniformly downsampled case (c-e), as compared with the reconstructed image after 5.25x warped stretch compression (f-h). The downsampling rate for the uniform case was increased (hence the image quality improvement) such that the resultant file sizes for both warped and uniform compression become equal (to compensate for the warp kernel overhead). After reconstruction, the warped case (g-h) achieved a PSNR of 37.7 dB, which was 6.32 dB better than the uniform downsampling case (d-e).

We also performed warped stretch compression on a 3-channel RGB colour portrait image. Figure 8.5 shows the comparison in compression performance between uniform downsampling and warped stretch compression at 8x and 10x compression, respectively. All three channels here are able to share the same warp kernel, which reduces the metadata overhead. The warp kernel was generated using only the blue channel as it was the most feature-dense. The reconstruction performance exceeds the uniform downsampling case by approximately 3 dB at 10x compression.

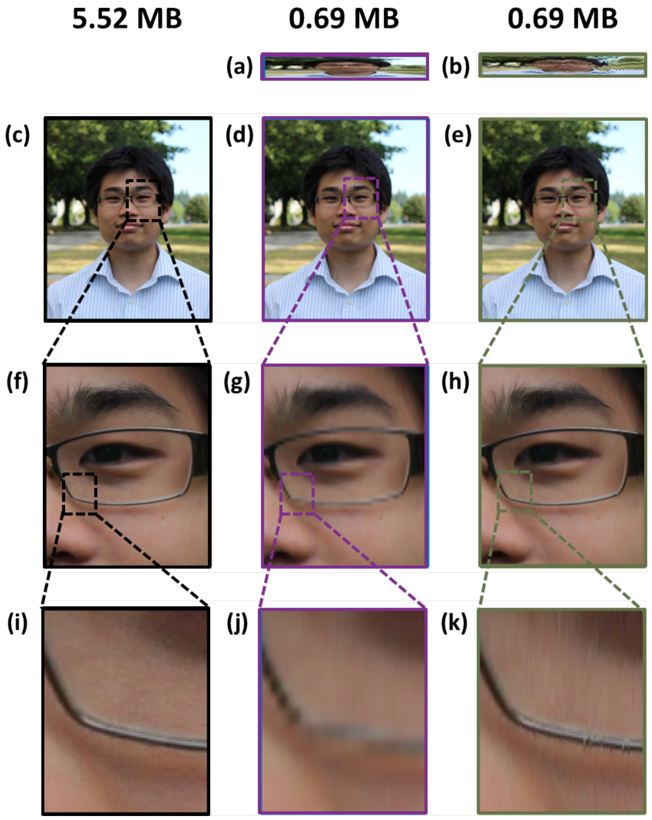

Figure 8.5: Comparison of compression performance with the colour portrait image. (a) The 8x uniformly downsampled image and (b) the 10.2x warp stretch–compressed image are shown with (c) the original image and (d-e) their respective reconstructions, while (f-h) are, in turn, their respective close-up portions. Further zoom-ins on the rims of the glasses are shown in (i-h), highlighting the failure of uniform downsampling to capture this sharp feature. The downsampling rate for the uniform case was adjusted such that the resultant file sizes for both warped and uniform compression become equal; however, since all three colour channels share the same warp kernel, the overhead burden is reduced by a third in this scenario. After reconstruction, the warped case (e,h,k) achieved a PSNR of 39.1 dB, which was 3.11 dB better than the uniform downsampling case (d,g,j).

Figure 8.6 shows the rate distortion plot for warped stretch compression as compared to compression with uniform downsampling for the fractal clock and the

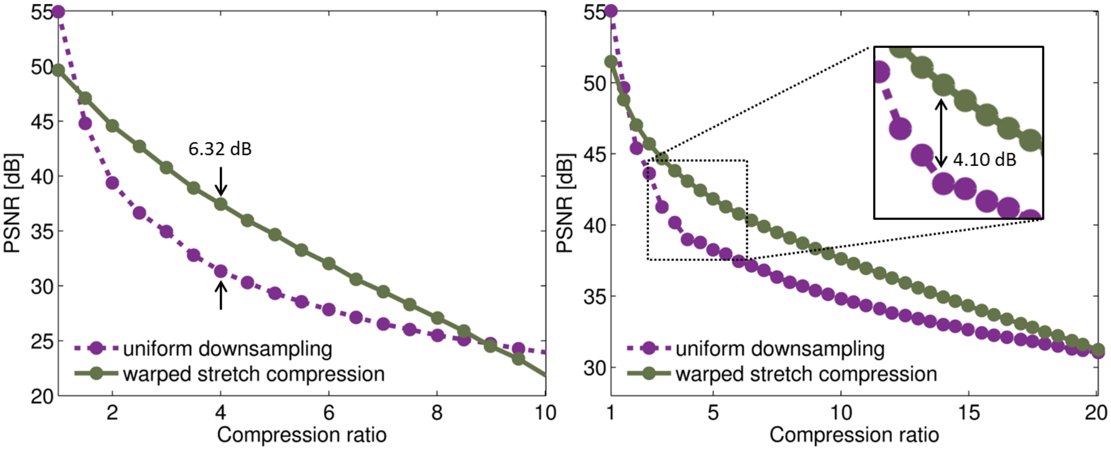

Figure 8.6: Empirical rate distortion plot for fractal clock and portrait images The PSNR of warped stretch compression (solid) is compared with uniform downsampling (dotted) over a range of compression ratios for (a) the grayscale fractal clock image and (b) the colour portrait image. At a compression ratio of 4x, warped stretch outperforms in PSNR by 6.32 dB in the clock, and by 4.10 dB in the portrait. Beyond the compression ratios of 9x and 20x respectively, the overhead from the warp kernel completely compromises the performance.

portrait images. Warped stretch compression was found to be superior to uniform downsampling from a compression ratio of 1.5x, up to 9x for the fractal clock and up to 20x for the portrait image. The range is extended for the colour image due to the lower overhead from the sharing of the warp kernel between colour channels. At a compression ratio of 4x, we find that warped stretch compression is better by more than 6 dB in PSNR for the grayscale clock and more than 4 dB for the color portrait. The lower PSNR difference for the colour image relative to the grayscale image can be attributed to the imperfect entropy redistribution in the red and green channels via using the warp kernel of the blue channel; the blue channel alone achieves a maximum PSNR improvement of 5.85 dB at 4x compression, as compared to 2.55 dB for the red channel, and 3.68 dB for the green channel at the same compression ratio.

To explain the rate-distortion behaviour, we consider how the same warp kernel is used for different compression ratios. As the compression ratio is increased, the post-warp uniform downsampling rate decreases, and the Nyquist condition is no longer satisfied. This is the main source of information loss in any compression scheme which involves downsampling.

8.4 Conclusion

We have formulated a new type of digital image compression inspired by the recently demonstrated analog optical image compression enabled by warped stretch transform [3]. Our optics-inspired method warps the input image based on the distribution of its features, causing context-aware redistribution of the local entropy. Compared to the Fourier domain implementation of warped stretch image compression (DAST) reported earlier, this direct warping eliminates the need for phase retrieval in reconstruction. In this work, we limited the treatment to one-dimensional lines and simplify the analysis. We have shown more than 6 dB improvement in PSNR at a 4x compression ratio compared to the case of uniform downsampling. Future works would extend this to a full two-dimensional warped stretch transformation, and would investigate the combination of it with JPEG compression.

CHAPTER 9

Conclusion and future work

The concept of warped time stretch was explored as a generalization of photonic time stretch to arbitrary dispersion profiles. We first analyzed the warped stretch transformations theoretically, and developed for the first time the additional conditions necessary for a warped mapping of the input optical spectrum into time. We show that each time stretch system can be described by the same stretch factor as long as the effective dispersion is identified, and demonstrate how to identify this effective chromatic dispersion in most major time-stretch systems that disperse in other domains (e.g. angle, space). Mathematical expressions for describing the temporal chirp of an input signal in terms of its group delay profile in the spectral domain were also established. Via a basis decomposition in the spectral domain, the equivalence enables arbitrary control of the temporal profile of a time-stretched broadband optical signal.

Given sufficient a-priori knowledge of the spectrotemporal statistics of the optical input pulses, the appropriate frequency dependence for dispersive elements can be designed; what is appropriate depends on the application. One application of the proper design of warped stretch transformation is in time-bandwidth product engineering. Using time-frequency analysis, we develop and simulate the effect of warped dispersion on the time-bandwidth product of a broadband optical signal, and compared them to theoretical expressions. Given that the smoothness constraints are satisfied, the time-bandwidth product is entirely dependent on the group delay profile and the input time duration and modulation bandwidth.

Using a dispersive time-frequency distribution defined as the “stretched modulation distribution”, we also show the bandwidth is expanded due to group delay imperfections, which break the sideband symmetry and introduce beat artifacts. We also show that while the bandwidth is greatly affected by imperfections in the dispersion profile, tolerances are quantifiable and can be used to determine an effective time-bandwidth product the on the performance of such systems.

Our analysis on noise tolerances was extended to dispersive phase recovery systems in the presence of noise. While the particular amount of noise tolerance depends on the retrieval method and sometimes the signal statistics itself, each phase retrieval method can be assigned an output signal to noise and distortion ratio (SNDR), or equivalently, an output effective number of bits (ENOB) as a threshold, under which the method breaks down and no longer functions properly. This helps provide justifiication in assuming a perfect photodetection system; as long as one can limit the noise and distortion introduced into the system to that below the threshold, the signal can be reconstructed.

Combining our results for time-bandwidth engineering and phase reconstruction, we also show that the signal-to-noise ratio of the optical signal can be engineered. The signal-to-noise ratio. We mathematically show the SNR improvement possible relative to a linearly stretched signal, then show the per-sample averaged effects on the SNR in terms of the instantaneous power and bandwidth reduction. This provides a design pathway for translating the a-priori knowledge of signal spectra into context-optimized data acquisition and processing.

We also show experimentally one possible physical implementaiton of reconfigurable chromatic dispersion profiles. The dynamic tuning of dispersion is enabled by acousto-optic mode excitation of a multimode structure offering tuning of optical dispersion via RF frequency. Also featuring wavelength tuning, our device achieves real-time temporal tuning of narrowband pulses over 1.27 ns and 40 nm of optical bandwidth. It also provides amplitude control of at least 20 dBm, via attenuation of the acousto-optic power.

Finally, we demonstrated the extension of the warped stretch concept to the digital domain as a method for image compression. Our method performs context aware sampling on the input image by redistributing the local entropy prior to uniform downsampling. This is equivalent to performing non-uniform sampling on the image in a reversible manner, which eliminates the need for phase recovery to recover the decompressed image. Relative to blind downsampling, we have shown the effectiveness of our approach over a wide range of compression ratios from 2x up to 20x compression, with ovre 6 dB of improvement in PSNR at 4x compression.

For future work, we recommend the experimental demonstration of a dispersion-based spread spectrum telecommunication system based on the analytical results from SNR engineering with warped stretch. The SNR of an amplitude-shift keying system can potentially be improved once the spectrotemporal statistics are known, then de-warped in the digital domain at the receiver side. Using reconfigurable dispersion sources, the system can also correct for dispersion drifts of the channel. During transmission, the signal can also hidden with extremely high dispersion; if additionally this dispersion profile is uniquely designed, the transmitted optical signal cannot be recovered without the correct inverse dispersion. This has practical appllcations in cybersecure optical transmissions that are immune to interceptions. We also suggest further work on warped stretch image compression, by incorporating the technique with existing compression algorithms, such as JPEG 2000 or RAISR, as pre- or post-compression step.

References

[1] A Mahjoubfar, CL Chen, and B Jalali. Design of warped stretch transform. *Scientific reports*, 5:17148–17148, 2015.

[2] Ata Mahjoubfar, Claire Lifan Chen, and Bahram Jalali. Design of warped stretch transform. In *Artificial Intelligence in Label-free Microscopy*, pages 101–119. Springer, 2017.

[3] Claire Lifan Chen, Ata Mahjoubfar, and Bahram Jalali. Optical data compression in time stretch imaging. *PloS one*, 10(4):e0125106, 2015.

[4] Haiyun Xia, Chao Wang, Sébastien Blais, and Jianping Yao. Ultrafast and precise interrogation of fiber bragg grating sensor based on wavelength-to-time mapping incorporating higher order dispersion. *Journal of lightwave technology*, 28(3):254–261, 2010.

[5] Weiwen Zou, Hao Zhang, Xin Long, Siteng Zhang, Yuanjun Cui, and Jianping Chen. All-optical central-frequency-programmable and bandwidth-tailorable radar. *Scientific reports*, 6:19786, 2016.

[6] Mengxuan Lv, Bo Dai, Songchao Yin, Dawei Zhang, and Xu Wang. Power efficiency of time-stretch imaging system by using parallel interleaving detection. *Chinese Optics Letters*, 14(10):101103, 2016.

[7] Chaitanya K Mididoddi, Fangliang Bai, Guoqing Wang, Jinchao Liu, Stuart Gibson, and Chao Wang. High-throughput photonic time-stretch optical coherence tomography with data compression. *IEEE Photonics Journal*, 9(4):1–15, 2017.

[8] Bo Dai, Songchao Yin, Zhensen Gao, Kaimin Wang, Dawei Zhang, Songlin Zhuang, and Xu Wang. Data compression for time-stretch imaging based on differential detection and run-length encoding. *Journal of Lightwave Technology*, 35(23):5098–5104, 2017.

[9] Ata Mahjoubfar, Dmitry V Churkin, Stéphane Barland, Neil Broderick, Sergei K Turitsyn, and Bahram Jalali. Time stretch and its applications. *Nature Photonics*, 11(6):341, 2017.

[10] AS Bhushan, F Coppinger, and B Jalali. Time-stretched analogue-to-digital conversion. *Electronics Letters*, 34(11):1081–1083, 1998.

[11] F Coppinger, AS Bhushan, and B Jalali. Photonic time stretch and its application to analog-to-digital conversion. *IEEE Transactions on microwave theory and techniques*, 47(7):1309–1314, 1999.

[12] Shalabh Gupta and Bahram Jalali. Time stretch enhanced recording oscilloscope. *Applied Physics Letters*, 94(4):041105, 2009.

[13] Peter T. S. DeVore, Brandon Walter Buckley, Mohammad Hossein Asghari, Daniel Roy Solli, and Bahram Jalali. Coherent time-stretch transform for near-field spectroscopy. *IEEE Photonics*, 6(8), 2014.

[14] Keisuke Goda, Daniel R Solli, and Bahram Jalali. Real-time optical reflectometry enabled by amplified dispersive fourier transformation. *Applied Physics Letters*, 93(3):031106, 2008.

[15] Keisuke Goda, Ali Fard, Omer Malik, Gilbert Fu, Alan Quach, and Bahram Jalali. High-throughput optical coherence tomography at 800 nm. *Optics express*, 20(18):19612–19617, 2012.

[16] K Goda, KK Tsia, and B Jalali. Serial time-encoded amplified imaging for real-time observation of fast dynamic phenomena. *Nature*, 458(7242):1145, 2009.

[17] Claire Lifan Chen, Ata Mahjoubfar, Li-Chia Tai, Ian K Blaby, Allen Huang, Kayvan Reza Niazi, and Bahram Jalali. Deep learning in label-free cell classification. *Scientific reports*, 6:21471, 2016.

[18] Akio Yazaki, Chanju Kim, Jacky Chan, Ata Mahjoubfar, Keisuke Goda, Masahiro Watanabe, and Bahram Jalali. Ultrafast dark-field surface inspection with hybrid-dispersion laser scanning. *Applied Physics Letters*, 104(25):251106, 2014.

[19] RE Saperstein, N Alic, S Zamek, K Ikeda, B Slutsky, and Y Fainman. Processing advantages of linear chirped fiber bragg gratings in the time domain realization of optical frequency-domain reflectometry. *Optics Express*, 15(23):15464–15479, 2007.

[20] Ata Mahjoubfar, Keisuke Goda, Ali Ayazi, Ali Fard, Sang Hyup Kim, and Bahram Jalali. High-speed nanometer-resolved imaging vibrometer and velocimeter. *Applied Physics Letters*, 98(10):101107, 2011.

[21] Mohammad Umar Piracha. *A Laser Radar Employing Linearly Chirped Pulses From A Mode-locked Laser For Long Range, Unambiguous, Submillimeter Resolution Ranging And Velocimetry*. PhD thesis, University of Central Florida, 2012.

[22] BM La Lone, BR Marshall, EK Miller, GD Stevens, WD Turley, and LR Veeser. Simultaneous broadband laser ranging and photonic doppler velocimetry for dynamic compression experiments. *Review of Scientific Instruments*, 86(2):023112, 2015.

[23] George Rodriguez and Steve M Gilbertson. Ultrafast fiber bragg grating interrogation for sensing in detonation and shock wave experiments. *Sensors*, 17(2):248, 2017.

[24] Michelle Rhodes, Corey Bennett, and Daniel Perry. Accuracy and precision in broadband laser ranging. In *Real-time Measurements, Rogue Phenomena, and Single-Shot Applications III*, volume 10517, page 105170B. International Society for Optics and Photonics, 2018.

[25] G Herink, B Jalali, C Ropers, and DR Solli. Resolving the build-up of femtosecond mode-locking with single-shot spectroscopy at 90 mhz frame rate. *Nature Photonics*, 10(5):321, 2016.

[26] Antoine FJ Runge, Neil GR Broderick, and Miro Erkintalo. Observation of soliton explosions in a passively mode-locked fiber laser. *Optica*, 2(1):36–39, 2015.

[27] E Roussel, C Evain, M Le Parquier, C Szwaj, S Bielawski, L Manceron, J-B Brubach, M-A Tordeux, J-P Ricaud, L Cassinari, et al. Observing microscopic structures of a relativistic object using a time-stretch strategy. *Scientific Reports*, 5:10330, 2015.

[28] DR Solli, J Chou, and B Jalali. Amplified wavelength–time transformation for real-time spectroscopy. *Nature Photonics*, 2(1):48, 2008.

[29] Francesco Saltarelli, Vikas Kumar, Daniele Viola, Francesco Crisafi, Fabrizio Preda, Giulio Cerullo, and Dario Polli. Broadband stimulated raman scattering spectroscopy by a photonic time stretcher. *Optics express*, 24(19):21264–21275, 2016.

[30] Ata Mahjoubfar, Claire Lifan Chen, and Bahram Jalali. Deep learning and classification. In *Artificial Intelligence in Label-free Microscopy*, pages 101–119. Springer, 2017.

[31] Jost Adam, Ata Mahjoubfar, Eric D Diebold, Brandon W Buckley, and Bahram Jalali. Spectrally encoded angular light scattering. *Optics express*, 21(23):28960–28967, 2013.

[32] Bahram Jalali and Ata Mahjoubfar. Tailoring wideband signals with a photonic hardware accelerator. *Proceedings of the IEEE*, 103(7):1071–1086, 2015.

[33] Ali M Fard, Shalabh Gupta, and Bahram Jalali. Photonic time-stretch digitizer and its extension to real-time spectroscopy and imaging. *Laser & Photonics Reviews*, 7(2):207–263, 2013.

[34] Keisuke Goda, Daniel R Solli, Kevin K Tsia, and Bahram Jalali. Theory of amplified dispersive fourier transformation. *Physical Review A*, 80(4):043821, 2009.

[35] Bahram Jalali, Ata Mahjoubfar, and Claire L Chen. High-throughput biological cell classification featuring real-time optical data compression. In *Information Sciences and Systems (CISS), 2015 49th Annual Conference on*, pages 1–3. IEEE, 2015.

[36] Bahram Jalali and Frederic Marie Alain Coppinger. Data conversion using time manipulation, September 11 2001. US Patent 6,288,659.

[37] Yan Han and Bahram Jalali. Photonic time-stretched analog-to-digital converter: fundamental concepts and practical considerations. *Journal of Lightwave Technology*, 21(12):3085, 2003.

[38] Ezra Ip, Alan Pak Tao Lau, Daniel JF Barros, and Joseph M Kahn. Coherent detection in optical fiber systems. *Optics express*, 16(2):753–791, 2008.

[39] Daniel Roy Solli, Shalabh Gupta, and Bahram Jalali. Optical phase recovery in the dispersive Fourier transform. *Applied Physics Letters*, 95:231108, 2009.

[40] Mohammad Hossein Asghari and Bahram Jalali. Stereopsis-inspired time-stretched amplified real-time spectrometer (STARS). *IEEE Photonics Journal*, 4:1673–1701, 2012.

[41] Christophe Dorrer and Inuk Kang. Complete temporal characterization of short optical pulses by simplified chronocyclic tomography. *Optics Express*, 28:1481–1483, 2003.

[42] Ian Alexander Walmsley and Christophe Dorrer. Characterization of ultrashort electromagnetic pulses. *Advances in Optics and Photonics*, 1(2):308–437, 2009.

[43] Gonhsin Liu and Peter D Scott. Phase retrieval and twin-image elimination for in-line fresnel holograms. *Journal of the Optical Society of America A*, 4(1):159–165, 1987.

[44] S Grilli, P Ferraro, S De Nicola, A Finizio, G Pierattini, and R Meucci. Whole optical wavefields reconstruction by Digital Holography. *Optics Express*, 9(6):294–302, 2001.

[45] Yan Zhang, Giancarlo Pedrini, Wolfgang Osten, and Hans J Tiziani. Whole optical wave field reconstruction from double or multi in-line holograms by phase retrieval algorithm. *Optics Express*, 11(24):3234–3241, 2003.

[46] Wai Lam Chan, Matthew L Moravec, Richard G Baraniuk, and Daniel M Mittleman. Terahertz imaging with compressed sensing and phase retrieval. *Optics Letters*, 33(9):974–976, 2008.

[47] Kishore Jaganathan, Samet Oymak, and Babak Hassibi. Phase retrieval for sparse signals using rank minimization. *IEEE Transactions on Information Theory*, 52(8):489–509, 2012.

[48] G Herink, F Kurtz, B Jalali, DR Solli, and C Ropers. Real-time spectral interferometry probes the internal dynamics of femtosecond soliton molecules. *Science*, 356(6333):50–54, 2017.

[49] Cejo K Lonappan, Brandon Buckley, Daniel Lam, Asad M Madni, Bahram Jalali, and Jost Adam. Time-stretch accelerated processor for real-time, in-service, signal analysis. In *Signal and Information Processing (GlobalSIP), 2014 IEEE Global Conference on*, pages 707–711. IEEE, 2014.

[50] Christophe Szwaj, Clément Evain, M Le Parquier, Pascale Roy, Laurent Manceron, J-B Brubach, M-A Tordeux, and Serge Bielawski. High sensitivity photonic time-stretch electro-optic sampling of terahertz pulses. *Review of Scientific Instruments*, 87(10):103111, 2016.

[51] AM Fard, B Buckley, S Zlatanovic, C-S Bres, S Radic, and B Jalali. All-optical time-stretch digitizer. *Applied Physics Letters*, 101(5):051113, 2012.

[52] Jia-Ming Liu. *Coupled-wave analysis*, chapter 9.4. Cambridge University Press, 2009.

[53] Bahram Jalali, Jacky Chan, and Mohammad H Asghari. Time–bandwidth engineering. *Optica*, 1(1):23–31, 2014.

[54] Jacky Chan, Ata Mahjoubfar, M Asghari, and Bahram Jalali. Reconstruction in time-bandwidth compression systems. *Applied Physics Letters*, 105(22):221105, 2014.

[55] Herbert Bristol Dwight. Tables of integrals and other mathematical data. *New York: The MacMillan Company,— c1947, Revised Edition*, 1947.

[56] Mohammad Hossein Asghari and José Azaña. Self-referenced temporal phase reconstruction from intensity measurements using causality arguments in linear optical filters. *Optics Letters*, 37:3582–3584, 2012.

[57] Ata Mahjoubfar, Keisuke Goda, Gary Betts, and Bahram Jalali. Optically amplified detection for biomedical sensing and imaging. *Journal of the Optical Society of America A*, 30:2124–2132, 2013.

[58] B Jalali, DR Solli, K Goda, K Tsia, and C Ropers. Real-time measurements, rare events and photon economics. *The European Physical Journal Special Topics*, 185(1):145–157, 2010.

[59] DR Solli, C Ropers, P Koonath, and B Jalali. Optical rogue waves. *Nature*, 450(7172):1054, 2007.

[60] Nail Akhmediev, Adrian Ankiewicz, and Majid Taki. Waves that appear from nowhere and disappear without a trace. *Physics Letters A*, 373(6):675–678, 2009.

[61] Bertrand Kibler, Julien Fatome, Christophe Finot, Guy Millot, Frédéric Dias, Goëry Genty, Nail Akhmediev, and John M Dudley. The peregrine soliton in nonlinear fibre optics. *Nature Physics*, 6(10):790, 2010.

[62] Benjamin Wetzel, Alessio Stefani, Laurent Larger, Pierre-Ambroise Lacourt, Jean-Marc Merolla, Thibaut Sylvestre, A Kudlinski, Arnaud Mussot, Goëry Genty, Frédéric Dias, et al. Real-time full bandwidth measurement of spectral noise in supercontinuum generation. *Scientific reports*, 2:882, 2012.

[63] RM Fortenberry, WV Sorin, H Lin, SA Newton, JK Andersen, and MN Islam. Low-power ultrashort optical pulse characterization using linear dispersion. In *Optical Fiber Communication. OFC 97., Conference on*, pages 290–291. IEEE, 1997.

[64] PV Kelkar, F Coppinger, AS Bhushan, and B Jalali. Time-domain optical sensing. *Electronics Letters*, 35(19):1661–1662, 1999.

[65] Mark A Foster, Reza Salem, David F Geraghty, Amy C Turner-Foster, Michal Lipson, and Alexander L Gaeta. Silicon-chip-based ultrafast optical oscilloscope. *Nature*, 456(7218):81, 2008.

[66] George C Valley. Photonic analog-to-digital converters. *Optics express*, 15(5):1955–1982, 2007.

[67] Johan Stigwall and Sheila Galt. Signal reconstruction by phase retrieval and optical backpropagation in phase-diverse photonic time-stretch systems. *Journal of Lightwave Technology*, 25(10):3017–3027, 2007.

[68] Mohammad Hossein Asghari, Yongwoo Park, and José Azaña. Complex-field measurement of ultrafast dynamic optical waveforms based on real-time spectral interferometry. *Optics Express*, 18:16526–16538, 2010.

[69] Feng Qian, Qi Song, En kuang Tien, Salih Kagan Kalyoncu, and Ozdal Boyraz. Real-time optical imaging and tracking of micron-sized particles. *Optics Communications*, 282(24):4672—4675, 2009.

[70] Chi Zhang, Yi Qiu, Rui Zhu, Kenneth KY Wong, and Kevin K Tsia. Serial time-encoded amplified microscopy (steam) based on a stabilized picosecond supercontinuum source. *Optics express*, 19(17):15810–15816, 2011.

[71] Bahram Jalali and Mohammad H Asghari. The anamorphic stretch transform: Putting the squeeze on "big data". *Optics and Photonics News*, 25(2):24–31, 2014.

[72] B Jalali, P Kelkar, and V Saxena. Photonic arbitrary waveform generator. In *Lasers and Electro-Optics Society, 2001. LEOS 2001. The 14th Annual Meeting of the IEEE*, volume 1, pages 253–254. IEEE, 2001.

[73] JD McKinney, DS Seo, and AM Weiner. Photonically assisted generation of continuous arbitrary millimetre electromagnetic waveforms. *IEEE Electronic Letters*, 39(3):309–310, 2003.

[74] Jianping Yao, Fei Zeng, and Qing Wang. Photonic generation of ultrawideband signals. *Journal of Lightwave Technology*, 25(11):3219–3235, 2007.

[75] Mohammad H Asghari and Bahram Jalali. Anamorphic transformation and its application to time–bandwidth compression. *Applied optics*, 52(27):6735–6743, 2013.

[76] Mohammad H Asghari and Bahram Jalali. Experimental demonstration of optical real-time data compression. *Applied Physics Letters*, 104(11):111101, 2014.

[77] George A Sefler and George C Valley. Mitigation of group-delay-ripple distortions for use of chirped fiber-bragg gratings in photonic time-stretch adcs. *Journal of Lightwave Technology*, 31(7):1093–1100, 2013.

[78] Bernhard E Boser and Bruce A Wooley. The design of sigma-delta modulation analog-to-digital converters. *IEEE Journal of solid-state circuits*, 23(6):1298–1308, 1988.

[79] Robert H Walden. Analog-to-digital converter survey and analysis. *IEEE Journal on selected areas in communications*, 17(4):539–550, 1999.

[80] Sangil Park. Principles of sigma-delta modulation for analog-to-digital converters. *Motorola Digital Signal Processors*, 1999.

[81] CRS Fludger, V Handerek, and RJ Mears. Pump to signal rin transfer in raman fiber amplifiers. *Journal of Lightwave Technology*, 19(8):1140, 2001.

[82] René-Jean Essiambre, Gerhard Kramer, Peter J Winzer, Gerard J Foschini, and Bernhard Goebel. Capacity limits of optical fiber networks. *Journal of Lightwave Technology*, 28(4):662–701, 2010.

[83] Lars Gruner-Nielsen, Marie Wandel, Poul Kristensen, Carsten Jorgensen, L Vilbrad Jorgensen, Bent Edvold, Bera Pálsdóttir, and Dan Jakobsen. Dispersion-compensating fibers. *Journal of Lightwave Technology*, 23(11):3566–3579, 2005.

[84] D Garthe, RE Epworth, WS Lee, A Hadjifotiou, CP Chew, T Bricheno, A Fielding, HN Rourke, SR Baker, KC Byron, et al. Adjustable dispersion equaliser for 10 and 20 gbit/s over distances up to 160 km. *Electronics Letters*, 30(25):2159–2160, 1994.

[85] Jacky CK Chan and Bahram Jalali. Foveated time stretch. *arXiv preprint arXiv:1805.00143*, 2018.

[86] Eric D Diebold, Nick K Hon, Zhongwei Tan, Jason Chou, Todd Sienicki, Chao Wang, and Bahram Jalali. Giant tunable optical dispersion using chromo-modal excitation of a multimode waveguide. *Optics Express*, 19(24):23809–23817, 2011.

[87] Haeri Park, Mohammad Asghari, and Bahram Jalali. Dispersion engineering employing curved space mapping and chromo-modal excitation. In *CLEO: Science and Innovations*, pages JTh2A–34. Optical Society of America, 2015.

[88] Brandon W Buckley, Najva Akbari, Eric D Diebold, Jost Adam, and Bahram Jalali. Radiofrequency encoded angular-resolved light scattering. *Applied Physics Letters*, 106(12):123701, 2015.

[89] A Cozannet and M Treheux. Skew rays in optical fibers. *Applied Optics*, 14(6):1345–1350, 1975.

[90] Allan W Snyder and Mitchell D J. Leaky rays on circular optical fibers. *Journal of the Optical Society of America A*, 64(5):599–607, 1974.

[91] M Shirasaki. Large angular dispersion by a virtually imaged phased array and its application to a wavelength demultiplexer. *Optics letters*, 21(5):366–368, 1996.

[92] Richard L White. High-performance compression of astronomical images. *Sp. Earth Sci. Data Work.*, pages 117–123, 1993.

[93] Richard L White and Jeffrey W Percival. Compression and progressive transmission of astronomical images. In *Advanced Technology Optical Telescopes V*, volume 2199, pages 703–714. International Society for Optics and Photonics, 1994.

[94] M Louys, JL Starck, S Mei, F Bonnarel, and F Murtagh. Astronomical image compression. *Astronomy and Astrophysics Supplement Series*, 136(3):579–590, 1999.

[95] Alaitz Zabala, Xavier Pons, Ricardo Díaz-Delgado, Fernando García, Francesc Aulí-Llinàs, and Joan Serra-Sagristà. Effects of jpeg and jpeg2000 lossy compression on remote sensing image classification for mapping crops and forest areas. In *Geoscience and Remote Sensing Symposium, 2006. IGARSS 2006. IEEE International Conference on*, pages 790–793. IEEE, 2006.

[96] Frank Tintrup, Francesco De Natale, and Daniele Giusto. Compression algorithms for classification of remotely sensed images. In *Acoustics, Speech and Signal Processing, 1998. Proceedings of the 1998 IEEE International Conference on*, volume 5, pages 2565–2568. IEEE, 1998.

[97] Justin D Paola and Robert A Schowengerdt. The effect of lossy image compression on image classification. In *Geoscience and Remote Sensing Symposium, 1995. IGARSS'95.'Quantitative Remote Sensing for Science and Applications', International*, volume 1, pages 118–120. IEEE, 1995.

[98] Milan Sonka, Vaclav Hlavac, and Roger Boyle. *JPEG and MPEG image compression*, pages 734—-738. Cengage Learning, 2014.

[99] Harley R Myler. *Data management*, chapter 7.3. SPIE Optical Engineering Press, 1999.

[100] Marcial García Rojo, Gloria Bueno García, Carlos Peces Mateos, Jesús González García, and Manuel Carbajo Vicente. Critical comparison of 31 commercially available digital slide systems in pathology. *International journal of surgical pathology*, 14(4):285–305, 2006.

[101] Arjun Kalyanpur, Vladimir P Neklesa, Caroline R Taylor, Aditya R Daftary, and James A Brink. Evaluation of jpeg and wavelet compression of body ct images for direct digital teleradiologic transmission. *Radiology*, 217(3):772–779, 2000.

[102] Philippe P Bruyant, Michael A Gennert, Glen C Speckert, Richard D Beach, Joel D Morgenstern, Neeru Kumar, Suman Nadella, and Michael A King. A robust visual tracking system for patient motion detection in spect: Hardware solutions. *IEEE transactions on nuclear science*, 52(5):1288–1294, 2005.

[103] Nils T Siebel and SJ Maybank. Real-time tracking of pedestrians and vehicles. In *IEEE Workshop on PETS*, volume 33, 2001.

[104] King-Yeung Chan, Dominik Stich, and Greg A Voth. Real-time image compression for high-speed particle tracking. *Review of scientific instruments*, 78(2):023704, 2007.

[105] Mohammad H Asghari and Bahram Jalali. Discrete anamorphic transform for image compression. *IEEE Signal Processing Letters*, 21(7):829–833, 2014.

[106] K Goda and B Jalali. Dispersive fourier transformation for fast continuous single-shot measurements. *Nature Photonics*, 7(2):102, 2013.

[107] Bahram Jalali, Jacky CK Chan, Ata Mahjoubfar, Daniel R Solli, and Mohammad H Asghari. The temporal gearbox. *arXiv preprint arXiv:1612.04562*, 2016.

[108] Mohammad H Asghari and Bahram Jalali. Edge detection in digital images using dispersive phase stretch transform. *Journal of Biomedical Imaging*, 2015:6, 2015.

[109] James R Fienup. Phase retrieval algorithms: a comparison. *Applied Optics*, 21(15):2758–2769, 1982.

[110] Ralph W Gerchberg. A practical algorithm for the determination of phase from image and diffraction plane pictures. *Optik*, 35:237–246, 1972.

[111] Yiqing Xu, Zhibo Ren, Kenneth KY Wong, and Kevin Tsia. Overcoming the limitation of phase retrieval using gerchberg–saxton-like algorithm in optical fiber time-stretch systems. *Optics letters*, 40(15):3595–3598, 2015.

[112] Kishore Jaganathan, Samet Oymak, and Babak Hassibi. Sparse phase retrieval: Convex algorithms and limitations. *arXiv preprint arXiv:1303.4128*, 2013.

[113] G Liu and PD Scott. Phase retrieval and twin-image elimination for in-line fresnel holograms. *JOSA A*, 4(1):159–165, 1987.

[114] Stefano Marchesini, H He, Henry N Chapman, Stefan P Hau-Riege, A Noy, Malcolm R Howells, U Weierstall, and John CH Spence. X-ray image reconstruction from a diffraction pattern alone. *Physical Review B*, 68(14):140101, 2003.

[115] PK Atrey, A De, and N Rajpal. Polynomial representation of 2-d image boundary contours. In *TENCON'02. Proceedings. 2002 IEEE Region 10 Conference on Computers, Communications, Control and Power Engineering*, volume 1, pages 257–260. IEEE, 2002.

[116] Vipula Singh and Navin Rajpal. Efficient representation of 2d contour using non-uniform sampling. In *Signal Processing and Communications, 2004. SPCOM'04. 2004 International Conference on*, pages 37–40. IEEE, 2004.

[117] J Mark and T Todd. A nonuniform sampling approach to data compression. *IEEE Transactions on communications*, 29(1):24–32, 1981.

[118] Charles Joseph Rosenberg. *A lossy image compression algorithm based on nonuniform sampling and interpolation of the image intensity surface*. PhD thesis, Massachusetts Institute of Technology, 1990.

[119] Mohammad H Asghari and Bahram Jalali. Self-adaptive stretch in anamorphic image compression. In *Image Processing (ICIP), 2014 IEEE International Conference on*, pages 5571–5575. IEEE, 2014.